Lawrence Berkeley National Laboratory
Recent Work

Title
Characterization and manipulation of ion beam synthesized germanium nanocrystals

Permalink
https://escholarship.org/uc/item/1d12h37w

Author
Sharp, Ian David

Publication Date
2004-05-14

eScholarship.org Powered by the California Digital Library
University of California

Characterization and Manipulation of Ion Beam Synthesized Germanium Nanocrystals

by

Ian David Sharp

B.S. (University of California, Berkeley) 2002

A thesis submitted in partial satisfaction of the

requirements for the degree of

Master of Science

in

Engineering – Materials Science and Engineering

in the

GRADUATE DIVISION

of the

UNIVERSITY OF CALIFORNIA, BERKELEY

Committee in charge:

Prof. Eugene E. Haller, Chair

Prof. A. Paul Alivisatos

Prof. Daryl C. Chrzan

Spring 2004

Acknowledgements

This thesis would not have been possible without the assistance and support of many individuals. I would like to thank my thesis advisor, Professor Eugene E. Haller, who has provided me with a wealth of sound advice and enthusiastic encouragement since my time as an undergraduate student. I would also like to thank Professor Daryl C. Chrzan who has supplied the theoretical basis to make sense out of our experimental observations. Professor Oscar D. Dubón has always been available to provide me with guidance.

Many people contributed directly to the work presented in this thesis. In particular, I would like to thank my fellow graduate students Qing Xu, who has provided, amongst other things, exceptional electron diffraction patterns, Diana Yi, who has developed the theoretical models which describe the experimental data with surprising accuracy, and Chris Liao, who has assisted greatly with nanocrystal synthesis and experimental apparatus construction.

Dr. Joel W. Ager III has provided significant insight into all aspects of this project. In particular, he has taught me a great deal about Raman spectroscopy and the design of optical systems. I would also like to thank Jeff Beeman, who has provided time-consuming implants, advice on all aspects of lab work, and a side of humor. I would also like to thank Dr. Kin Man Yu for providing RBS data. Dr. Zuzanna Liliental-Weber and Dr. Dmitry N. Zakharov provided HRTEM results which really make the nanocrystals come to life. I would also like to thank Professor Hartmut Bracht for teaching me much about the world of diffusion.

I would like to thank all of the other members of the Haller group who are always supportive. David Hom is always willing to provide assistance with administrative matters and a good laugh. I would also like to specifically thank graduate students Hughes Silvestri, Ben Cardozo, Supriya Goyal, Abraham Anapolsky, and Becca Jones. Jeremy Robinson and Mike Scarpulla of the Dubón group also deserve thanks. Sam Nicols, a former Haller group member, provided my introduction to the group and training with much equipment.

I would never have made it this far (or perhaps I would have made it much further…) without the old chums: Bloke, Jimmy, Force, Rookie, Fwu, Cones, Meezil, Danny, and the Lemas. No one has provided me with more constant encouragement and friendship than Leah - thank you.

Most importantly, I would like to thank my parents and sister, all of whom were working diligently to obtain degrees at the same time as me. From an early age I was taught the value of education (from two educators, no less), and I thank them for always encouraging me to do my best.

I would like to acknowledge the support of the Intel Robert N. Noyce Fellowship in Microelectronics. This work is supported in part by the Director, Office of Science, Office of Basic Energy Sciences, Division of Materials Science and Engineering, of the U.S. Department of Energy under contract No. DE-AC03-76F00098 and in part by U.S. NSF Grant Nos. DMR-0109844 and EEC-0085569.

Table of Contents

1. Introduction 1
2. Nanocrystal Synthesis and Processing 8
   2.1. Ion Beam Synthesis 8
   2.2. Sample Preparation 9
   2.3. Closed Ampoule Annealing 11
3. Nanocrystal Characterization 14
   3.1 Introduction 14
   3.2 Rutherford Backscattering Spectrometry 14
   3.3 Raman Spectroscopy 17
      3.3.1 Experimental Technique 18
      3.3.2 Raman Spectroscopy in Bulk Crystals 20
      3.3.3 Phonon Confinement Effects 23
   3.4 Transmission Electron Microscopy 27
4. Liberation and Manipulation of Nanocrystals 32
   4.1 Introduction 32
   4.2 Experimental Procedure for Nanocrystal Liberation 33
   4.3 Vapor Etching Results 35
   4.4 Liquid Etching Results 38
   4.5 Van der Waals Interaction Forces 46
   4.6 Removal, Transfer, and Manipulation of Liberated Nanocrystals 51
5. In situ Characterization of Nanocrystals at Elevated Temperature 57
   5.1 Introduction 57
   5.2 In situ Raman Spectroscopy 58
      5.2.1 Experimental 58
      5.2.2 Anharmonic Effects on First Order Raman Spectra 58
      5.2.3 In situ Raman Spectroscopy Results 65
   5.3 In situ Transmission Electron Microscopy 68
      5.3.1 Experimental 68
      5.3.2 In situ Electron Diffraction Results 69
   5.4 Growth Experiments 71
   5.5 Theory of the Melting Behaviors of Nanocrystals 73
   5.6 Summary of Melting Point Observations 76
6. Characterization and Control of Nanocrystal Stresses 78
   6.1 Introduction 78
   6.2 Experimental Techniques 80
   6.3 Pressure Dependent Raman Spectroscopy 81
   6.4 Nanocrystal Coarsening Rate 83
   6.5 Surface Free Energy 84
   6.6 Aggregation Pressure 86
   6.7 Stress Relief Mechanism 88
7. Conclusions and Future Work 93

Appendix A: Van der Waals Interactions 95
Appendix B: Temperature Dependence of Raman Line Shapes 100
Appendix C: Pressure Dependence of Raman Line Positions 106
Appendix D: The Gibbs-Thomson Effect 110
Appendix E: Diffusive Stress Relaxation Model 112
References 122

1. Introduction

Aggressive device miniaturization by the semiconductor industry provides a strong driving force for the development of functional nanomaterials. As dimensions of materials decrease many physical properties diverge radically from those expected for bulk materials. Some of these properties are well understood and may be described by invoking standard quantum mechanical, thermodynamic, and mechanical arguments. Many other properties, however, remain mysterious. Thus, studies of fundamental physical, mechanical, electrical, and optical properties and mechanisms at the nanoscale are required to realize the full potential of these materials. Moreover, such studies provide a means to discover entirely new physical and chemical phenomena that can not be observed, or necessarily even predicted, otherwise.

As the dimensions of a semiconductor device approach the excitonic Bohr radius, quantum confinement effects begin to dominate optical and electronic processes.[1] One dimensional quantum confinement effects have been exploited to form thin film structures such as quantum wells and superlattices.[2] Structures exhibiting quantum confinement in two dimensions, such as nanowires and nanotubes, are currently being vigorously investigated.[3-12] Indeed, some of the first nanotube-based devices have begun to find commercial application as gas sensors. Structures which are governed by quantum confinement in all three dimensions, often called quantum dots, hold great promise for light emission[13-19] and spin[20-22] and charge[23-25] storage and manipulation. Crystalline quantum dots may be fabricated by a variety of methods, the most common including heteroepitaxial growth on a substrate,[26-30] chemical synthesis,[31-35] evaporation,[36,37] and solid state nucleation and growth.[38-45]

For the present study, isotopically pure ^{70}Ge and ^{74}Ge nanocrystals are synthesized by Ge ion implantation into silicon dioxide followed by high temperature thermal annealing. Chapter 2 details this synthesis procedure and Chapter 3 presents the results of experiments to characterize the as-grown crystals. This process, also called ion beam synthesis (IBS), has a number of unique advantages over other nanocrystal production procedures. Ion implantation is widely used in the semiconductor device manufacturing industry for the introduction of dopants. Therefore, an industrial infrastructure exists for integrating nanocrystals into semiconductor devices using current production lines. IBS is a mass selective process, so nanocrystals of a specific isotope may be formed. This may be used to produce nanocrystals composed of atoms with nuclear spins, such as ^{73}Ge or ^{29}Si, for spintronics investigations. Implantation is an inherently non-equilibrium process. Therefore, atoms may be introduced into any substrate, though growth of nanocrystals is dependent on solubilities and diffusivities of these atoms within the matrix.

Conversely, there are two significant drawbacks to IBS, both of which are general to nanocrystal synthesis within a solid matrix. These must be overcome to optimize the efficiencies of nanocrystal-based devices. First, IBS relies on a nucleation and growth process that yields wide nanocrystal size distributions. For narrow band optical emission and predictable charge storage, the size distribution must be significantly narrowed. To date, this has been accomplished with minimal success through implant profile selection[46,47] and system specific post-growth oxidation procedures.[48] Second, nanocrystals randomly nucleate in space. Therefore, self-organization of two- and three-dimensional arrays has not been achieved for Ge nanocrystals grown in the solid phase.

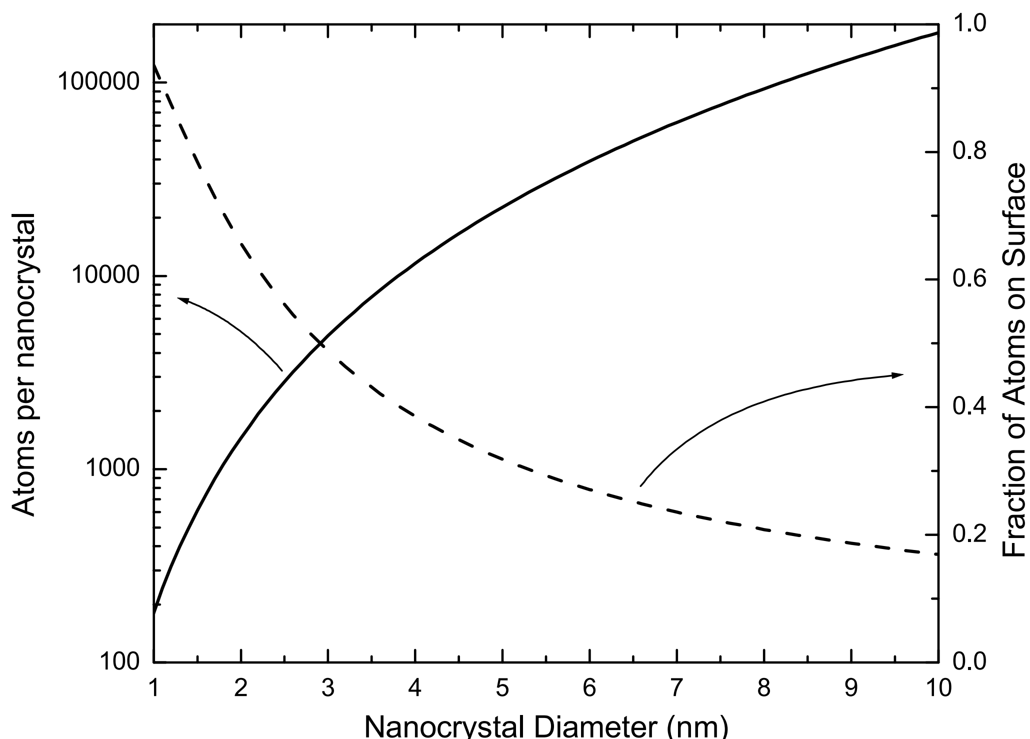

Figure 1.1: Plot of the total number of atoms (solid line) and the fraction of atoms forming the surface (dashed line) of a Ge nanocrystal as a function of size.

A number of the unique properties of nanocrystals are predicated by an extremely high surface to volume ratio. Figure 1.1 shows a plot of the total number of atoms in a Ge nanocrystal as a function of its diameter. In the present case, the average nanocrystal size is approximately 5 nm. Also shown in Figure 1.1 is the ratio of surface atoms to the total number of atoms in a nanocrystal as a function of the diameter, where surface atoms are defined as Ge-Ge bonded Ge atoms forming the interface between the nanocrystal and the surrounding environment. At the smallest sizes, which are readily attained using chemical and solid state synthesis methods, up to half of the total atoms sit on the surface. These atoms often dictate the properties of nanocrystals and entirely different physical behaviors may be observed for nanocrystals with different surface terminations.[49] Here, nanocrystals are embedded in a silica matrix which, it will be shown, suppresses surface atom vibrations and significantly alters the nanocrystal melting points and Raman

spectra. Understanding surface states, which may govern optical and electronic properties,[50-52] is essential for utilizing nanocrystals as device components.

Quantum confinement in nanocrystals leads to discrete atomic-like electronic energy levels and optical transitions.[16] Group IV bulk semiconductors have indirect band gaps which preclude their use as efficient optical devices. However, in the quantum confinement regime, a transition from indirect band gap to atomic-like discrete electronic states is predicted which would allow for highly efficient light emission from elemental semiconductors.[53] Germanium has a number of significant advantages over silicon, owing to its excitonic Bohr radius and specific band structure. The excitonic Bohr radius in Ge is approximately 24.3 nm, whereas that in Si is 4.9 nm.[54] As a result, quantum confinement is more pronounced and gets initiated at Ge nanocrystal sizes significantly larger than for Si nanocrystals. Furthermore, the direct band transition of Ge is 0.898 eV, which is only 138 meV above the indirect band gap.[55] For Si, the direct transition is 3.03 eV above the indirect gap.[55] Therefore, the transition from indirect to direct-like character should be far more easily attained in Ge nanocrystals. Figure 1.2 shows the exciton binding energy in Si and Ge as a function of nanocrystal diameter. Interestingly, the effective Ge bandgap rises above that of Si at a diameter of 5.5 nm. If narrow and controllable Ge nanocrystal size distributions can be obtained, Ge nanocrystal-based devices could be manufactured with size-dependent emission and absorption properties extending over wide energy ranges. Importantly for commercial application, these optical transitions occur in the visible and ultraviolet.

Though theory predicts strong light emission and absorption from Ge nanocrystals, this has still not been conclusively shown experimentally for the case of

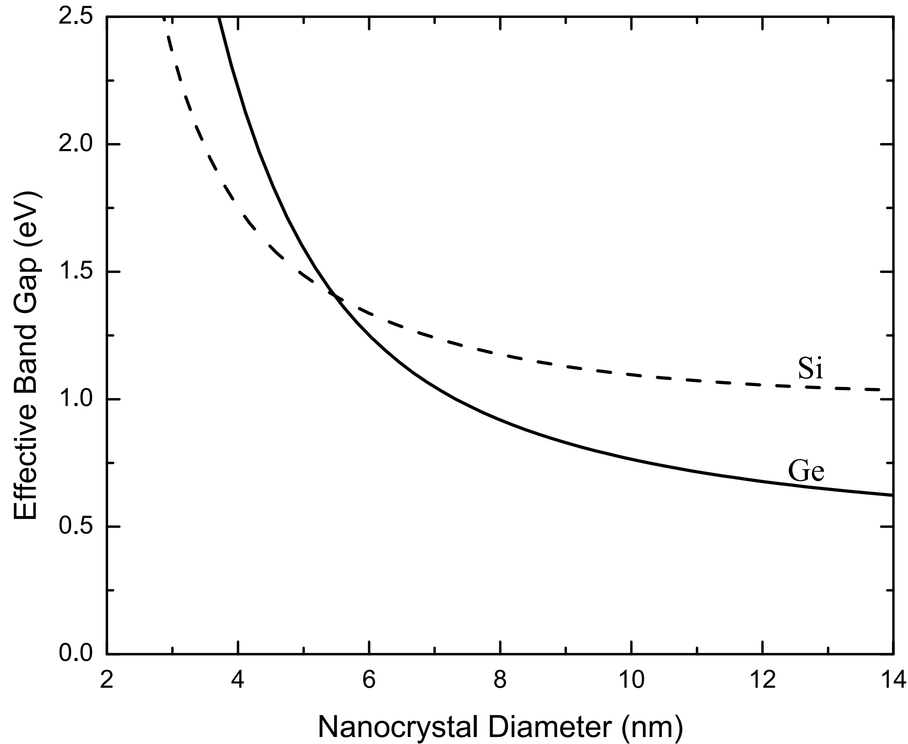

Figure 1.2: Plot of the free exciton binding energy as a function of diameter for Ge (solid line) and Si (dashed line) nanocrystals.[53]

embedded crystals. Nanocrystals formed in the solid state are typically embedded in silica, and many authors have reported strong photoluminescence.[39,56-67] However, it is often shown that the observed light emission arises from oxygen deficient defect centers near the silica/nanocrystal interface itself.[60-67] In Chapter 4, it will be shown that the silica matrix can be selectively removed to obtain free standing, or “liberated”, nanocrystals. Future experiments will focus on comparing emission spectra from liberated crystals to those from embedded crystals in order to isolate any emission arising from quantum confinement.

An additional promising application for Ge nanocrystals is solid state nonvolatile memory.[23] Nanocrystals may be embedded in the gate oxide of a standard transistor, as shown schematically in Figure 1.3. By appropriately biasing the device, nanocrystals can

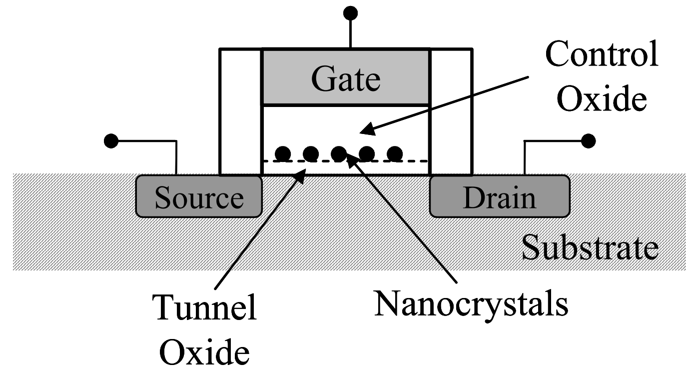

Figure 1.3: Schematic illustration of a nanocrystal-based transistor for solid state nonvolatile memory. Nanocrystals are located in the gate oxide region and may be charged, read, and discharged with the appropriate bias conditions.[23]

be charged. Charge saturation occurs after a single electron is added to each nanocrystal because of the so-called Coulomb blockade effect.[68] The energy required to add a second electron is significantly greater than to add the first electron because of Coulombic forces. Charged nanocrystals effectively shield the electric field of the charge on the gate, thereby increasing the threshold voltage for conduction through the channel. However, when nanocrystals are not charged, the transistor assumes normal operation. Hence, this device is capable of storing information, in the form of charge on the nanocrystals, which can then be read and written extremely rapidly. Since the nanocrystals are embedded in oxide, there are large electron retention times, in excess of those in present floating gate memory devices.

In Chapter 2, it is shown that ion beam synthesized nanocrystals are under significant compressive stresses (> 1 GPa). These stresses likely arise as a result of the growth process itself. *In-situ* Raman spectroscopy and electron diffraction were performed at elevated temperatures to determine nanocrystal melting points and more completely understand the growth of stressed nanocrystals (Chapter 5). In heteroepitaxial thin film and quantum dot growth, stress has been successfully exploited to achieve long

range island ordering[69-71] and narrow size distributions.[26,72-74] Therefore, stress generation and relief mechanisms are studied and provide significant insight into the dynamics of the growth process itself. Unlocking such information about solid state nanocrystal growth and stresses may provide a means of more controllably producing nanocrystals with specifically engineered properties. In Chapter 6, it is demonstrated that the controllable relief of stress can be achieved through post growth thermal treatments and a quantitative and mechanistic theoretical model is proposed to describe the relaxation process. Therefore, it is likely that stress, in addition to size, may be used to tune the optical and electronic bandgaps of nanocrystals.

2. Nanocrystal Synthesis and Processing

2.1. Ion Beam Synthesis

A remarkable array of both semiconductor and metal nanocrystals has been fabricated using a broad range of growth techniques. For the case of II-VI compound semiconductor nanocrystals, liquid phase chemical synthesis routes have achieved considerable success.[14,31,32,75,76] With a few notable exceptions,[34,77] however, successful synthesis of elemental semiconductor nanocrystals by chemical means has been limited. Nucleation and growth in the solid phase, typically a silicon dioxide matrix, has received considerable attention due to compatibility with present microelectronics processing techniques and the relative ease of nanocrystal formation. Ion beam synthesis (IBS),[39,40,46-48,78] chemical vapor deposition (CVD),[24,79,80] rf magnetron co-sputtering,[41,43,81,82] and molecular beam epitaxy (MBE)[38] are all commonly implemented for group IV semiconductor nanocrystal formation. In the present case, IBS has been selected for the formation of Ge nanocrystals in SiO_2 matrices.

IBS offers a promising approach to synthesizing metal[83-86], compound semiconductor (both III-V[44] and II-VI[87]), and group IV[39,40,46-48,78] semiconductor nanocrystals. In fact, a wide variety of semiconductor nanostructures including quantum dots,[88,89] core shell nanocrystals,[85,90] and even quantum wires,[91,92] have all been produced using this technique. IBS grown nanostructures offer the potential to be fabricated within existing semiconductor processing lines, thus maximizing their potential to be utilized in practical devices. This synthesis route is thus extremely straightforward, and broadly applicable.

IBS is achieved through implantation of the desired elemental species into a

Table 2.1: Atomic composition of naturally occurring Ge isotopes.[93]

Isotope	Atomic %
^{70}Ge	20.84
^{72}Ge	27.54
^{73}Ge	7.73
^{74}Ge	36.28
^{76}Ge	7.61

substrate. Control of the kinetic energy of incident ions and their dose allows for precise depth control over the concentration of the implanted species. Sequential implantation with ions of different energies and doses provides additional means of stipulating the concentration distribution. Furthermore, careful selection of implantation conditions, together with use of lithographically patterned masks, allows for three-dimensional control over concentration distributions.

The operation of ion implantation equipment is analogous to that of a high energy mass spectrometer. Therefore, IBS allows for the formation of nanocrystals with isotopically engineered compositions. Natural Ge, for example, is composed of five stable isotopes with the compositions given in Table 2.1.[93] Multiple implantations may be performed to create mixed isotope or, possibly, core-shell nanocrystals. In the present case, ^{70}Ge and ^{74}Ge nanocrystals are synthesized via implantation into silicon dioxide followed by thermal annealing.

2.2. Sample Preparation

Silicon dioxide was chosen as the host matrix material for nanocrystal growth due to its ease of production and compatibility with current microelectronics processes. Furthermore, Ge has a very small solubility in silica, so there is a strong driving force for the precipitation of the Ge to form nanocrystals. Silicon dioxide films, 500 nm in

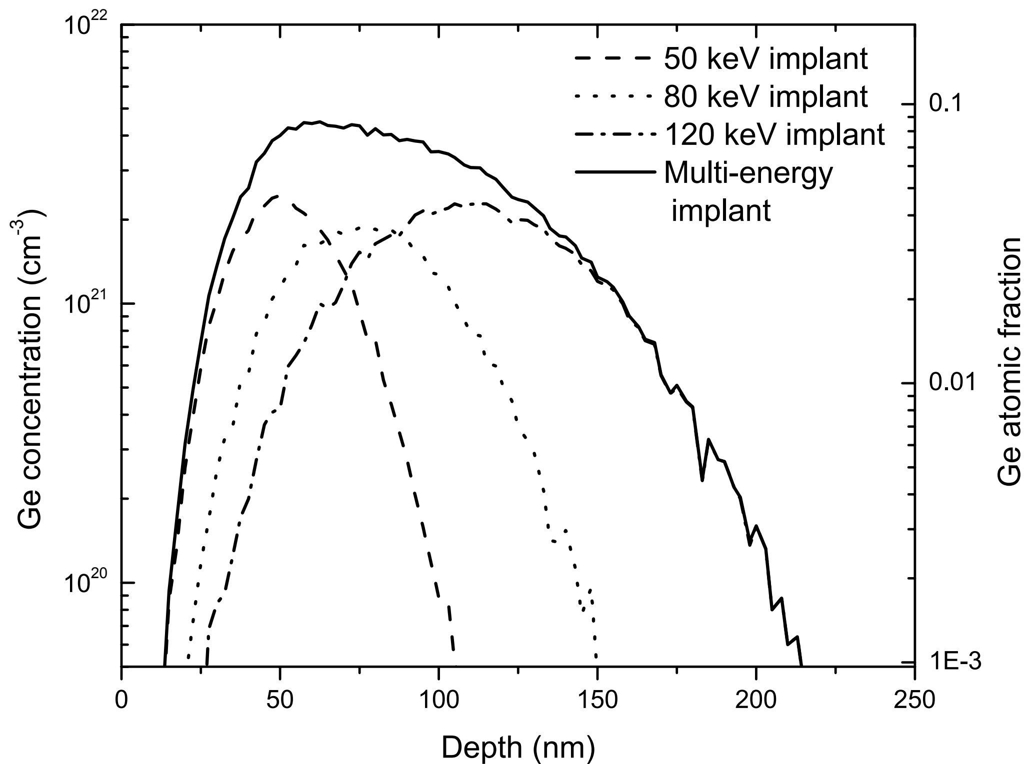

Figure 2.1: Ge concentration distributions for Ge implantation into SiO_2 obtained from TRIM simulation. A more constant concentration distribution near the peak may be achieved through multiple implants than from single implants.

thickness, were grown via wet oxidation of (100) oriented silicon substrates in a chemical vapor deposition (CVD) reactor. This layer thickness was chosen to suppress interactions between Ge atoms and the Si/SiO_2 interface during nanocrystal growth and subsequent processing.

Isotopically pure Ge nanocrystals were formed via implantation of either ^{70}Ge or ^{74}Ge into the 500 nm thick SiO_2 film. The Trapping Range of Ions in Matter (TRIM) Monte Carlo software package was used to predict Ge concentration distributions and select the desired implantation conditions.[94] Figure 2.1 shows the results of the TRIM simulation for room temperature multi-energy ion implantation of Ge with ion energies and doses of 50 keV at 1×10^{16} cm^{-2}, 80 keV at 1.2×10^{16} cm^{-2}, and 120 keV at 2×10^{16} cm^{-2}

into 500 nm thick silicon dioxide layers. These implantation conditions are similar to those used in the work of Yamamoto *et al*.[47] Multiple implantations were performed at various energies and doses in order to make the as-implanted Ge concentration nearly constant in the nanocrystal growth region. Implantation was performed using a Varian CF 3000 implanter and a germanium tetrafluoride (GeF_4) plasma source for Ge ions.

Prior to annealing, all samples were thoroughly cleaned to reduce the chance of surface contamination. Samples were immersed in boiling xylenes for approximately five minutes to remove organic contamination. Following cleaning in xylenes, samples were soaked in heated acetone for approximately two minutes and room temperature methanol for one minute. Samples were then dried under flowing nitrogen.

2.3. Closed Ampoule Annealing

To form nanocrystals, samples were annealed in a controlled argon atmosphere using the closed ampoule technique. This technique has been widely used for diffusion studies that require well controlled atmospheres at high temperatures. It is essential to eliminate oxygen and moisture from the annealing atmosphere when forming nanocrystals. In-diffusion of excess oxygen into the film results in oxidation of Ge to form GeO_x, which is fully soluble in silica and eliminates the driving force for precipitation of nanocrystals.

Ampoules were constructed by sealing one end of 1 cm outer diameter (0.8 cm inner diameter) semiconductor grade quartz tube obtained from GM Associates, Inc. Semiconductor grade quartz plugs were formed in the same way to enable sealing, as shown in Figure 2.2. Both quartz parts were rinsed in acetone then etched in 49% HF for 1 minute. Ampoule/plug assemblies containing samples for annealing were attached to

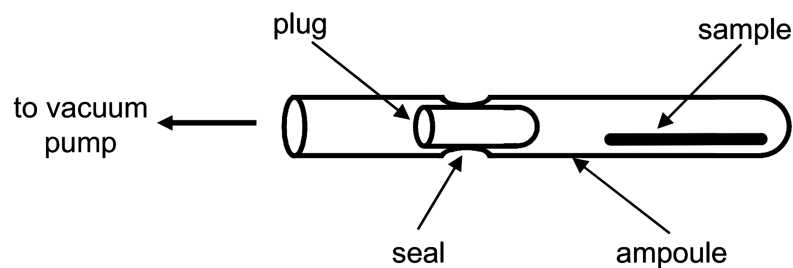

Figure 2.2: Diagram of an ampoule used for high temperature thermal annealing in a controlled argon atmosphere. The ampoule is evacuated to 1×10^{-5} torr, backfilled with 120 mTorr Ar, and sealed using a hydrogen/oxygen torch.

the sealing apparatus shown in Figure 2.3 and evacuated to less that 1×10^{-5} torr. Once the base pressure was reached, a hydrogen torch was used to heat the ampoule and the sealing apparatus in order to outgas the inner walls and remove any remnant organic solvents. The sealing assembly was then isolated from the pump system with a gate valve and the system was backfilled with argon to 120 mTorr to ensure adequate thermal

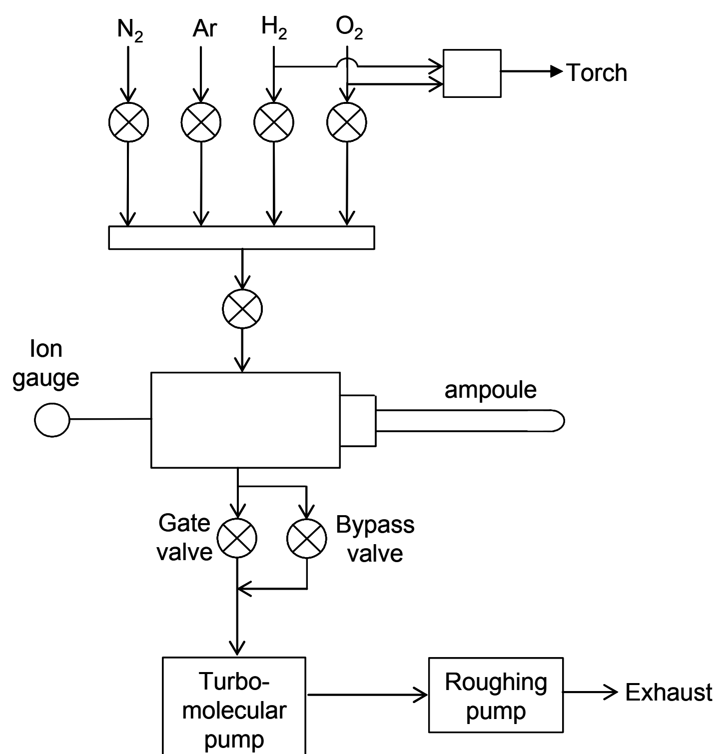

Figure 2.3: Diagram of the ampoule sealing apparatus. The ampoule is attached to a high vacuum system. A gas manifold allows for backfilling with a variety of gases.

coupling to the surrounding environment. A hydrogen/oxygen torch was used to seal the plug to the surrounding ampoule walls and isolate the sample from the outer atmosphere. Additional forming gases such as hydrogen, oxygen, and nitrogen in various proportions are also available if desired.

Nanocrystal growth was achieved by high temperature thermal annealing at temperatures between 800 °C and 900 °C for times ranging from 30 minutes to 60 minutes in a ±2 °C Lindbergh Blue resistively heated tube furnace. An S-type thermocouple encased in a quartz tube was placed in direct contact with the ampoule to precisely measure the annealing temperature. Annealing was terminated by rapidly quenching samples from the growth temperature under running cold water. Quenching to room temperature was achieved in less than 30 seconds. After removal from the ampoule, the xylenes/acetone/methanol cleaning procedure described above was repeated.

3. Nanocrystal Characterization

3.1 Introduction

A variety of characterization techniques were implemented to verify successful fabrication of nanocrystals, determine their size distributions, and explore their physical properties. This chapter will address characterization of the crystals immediately after growth and prior to subsequent processing. Rutherford backscattering spectrometry (RBS) was used to determine Ge concentration distributions, Raman spectroscopy was used to confirm the existence of nanocrystalline Ge, and transmission electron microscopy (TEM) was used to obtain nanocrystal size distributions and directly view their internal structures and interfaces with the surrounding matrix.

3.2 Rutherford Backscattering Spectrometry

RBS was performed both before and after thermal annealing to verify successful Ge implantation and observe the change in the Ge concentration profile during nanocrystal growth. This technique offers a number of advantages over competing depth profiling methods,[95] such as Secondary Ion Mass Spectrometry (SIMS). No standard reference sample is required for calibration since RBS gives an absolute measurement based on fundamental interactions. Unlike other profiling techniques, RBS is nondestructive since the sample is bombarded with He nuclei, which are extremely light and cause relatively little damage. RBS may be performed rapidly (the typical collection time is approximately 10 min per spectrum), thus making it a comparatively inexpensive method and allowing for characterization of a large number of samples.

In this technique, a sample is bombarded by high energy He^+ ions. The vast majority of the incident ions remain within the sample, but some are scattered back

towards a detector. The energy of the scattered ions depends on the substrate element that initiated scattering, the scattering angle, and the depth of interaction below the surface of the sample. Therefore, measurement of the number of scattered ions and their energies may be used to generate a concentration profile.[95]

To determine the Ge concentration profiles, RBS spectra were obtained using a 1.92 MeV He^+ beam, generated from a 2.5 MeV High Voltage Engineering AK-2500 van de Graaff accelerator, with a sample tilt of 50° to improve depth resolution. Backscattered ions were collected at an angle of 165° with a Si surface barrier detector.

Figure 3.1 shows the Ge concentration profile after multi-energy ion implantation and after subsequent thermal annealing. Implantation yields a Ge distribution with a

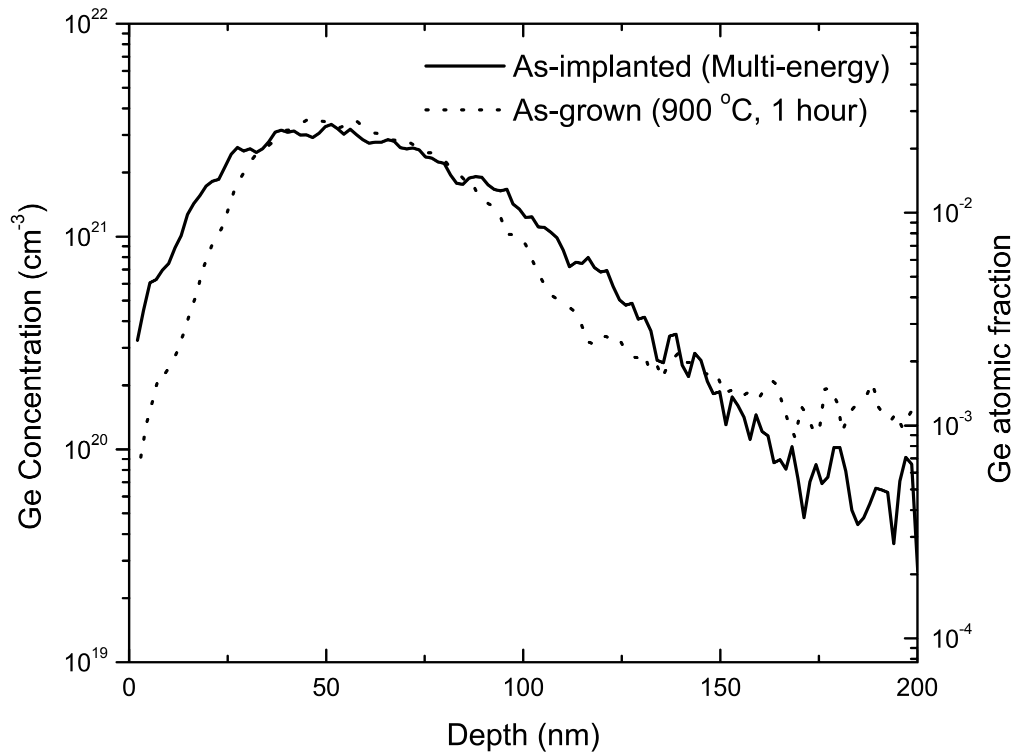

Figure 3.1: Concentration profiles obtained using Rutherford backscattering spectrometry. The profile width decreases upon thermal annealing at 900 °C for 1 hour in an argon atmosphere as a result of Ge nanocrystal nucleation and growth.

maximum of 6 atomic percent Ge located 50 nm below the surface, in reasonable agreement with the results from the TRIM simulation. However, the simulation predicts the concentration tail to extend to much greater depths. The reason for the discrepancy between simulation and experiment is not known. Nevertheless, the Ge concentration obtained is sufficient for the formation of nanocrystals. Upon annealing, the concentration distribution sharpens, which is consistent with nanocrystal precipitation. Usually, diffusion occurs down a concentration gradient. However, the true driving force for diffusion is the chemical potential. In this case, the chemical potential of Ge atoms in clusters is less than for isolated Ge atoms in silica and there exists a driving force for growth. As a result, the Ge concentration distribution narrows, as shown in Figure 3.1.

Figure 3.2 shows a RBS concentration profile for a sample implanted with 4×10^{16} cm^{-2} ^{74}Ge ions at 150keV before and after annealing in air at 900 ^{o}C for 16 hours. It is interesting to compare the approximate diffusivity of Ge under an inert atmosphere to that of Ge under air by equating the change in the logarithmic FWHM to the diffusion length, $\sqrt{D_{Ge}t}$. These calculations give diffusion coefficients of 1.1×10^{-15} cm^2 s^{-1} and 2.9×10^{-17} cm^2 s^{-1} for the diffusion of Ge in SiO_2 under Ar and under air at 900 ^{o}C, respectively, which are reasonable values for solid state diffusivities. Diffusion under air is observed to occur down the Ge concentration gradient due to oxidation. After oxidation, GeO_x forms and is soluble in SiO_2. As a result, the driving force for precipitation of nanocrystals is lost. Also, once Ge becomes oxidized, diffusion either requires the dissociation of a GeO_2 molecule or direct transport of this molecule, which is

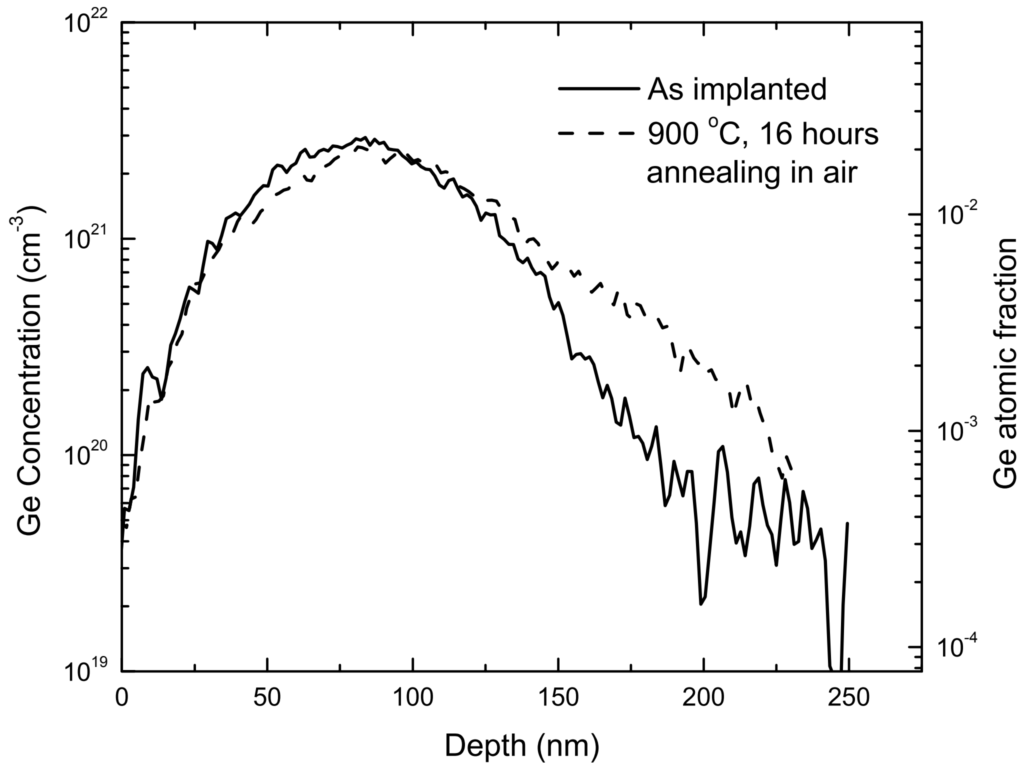

Figure 3.2: Concentration profiles obtained using Rutherford backscattering spectrometry. The profile width increases upon thermal annealing at 900 °C for 16 hours in air as a result of Ge oxidation.

much larger than elemental Ge, through the silica. As a result Ge diffusion is much slower in the presence of oxygen.

3.3 Raman Spectroscopy

Raman spectroscopy is one of the most powerful techniques for characterization of nanocrystals because it is very sensitive, may immediately ascertain crystallinity, is isotope specific, and may be used to calculate nanocrystal sizes and stress states. Phonon confinement in nanocrystalline materials results in asymmetric peak broadening of Raman spectra, and application of a phonon confinement model allows for determination of crystal sizes. Stress states of nanocrystals may be determined based on peak splitting (tensile or compressive stress) and shifts (hydrostatic pressure).

3.3.1 Experimental Technique

Raman spectra were obtained using the 488 nm line of Lexel Model 95 continuous wave Ar ion laser operating at 150 mW in a macroscopic optical setup with 5 cm^{-1} resolution. Figure 3.3 shows a schematic diagram of the Raman system. A narrow bandpass filter was used to eliminate laser lines. To maximize the interaction length, and thus the signal intensity, the laser beam was incident at a glancing angle to the surface of the sample. To eliminate the main laser line, while preserving the low intensity Raman signal, a holographic supernotch filter with an angular dependent bandpass spectrum was used. An Instruments SA, Inc. HR-640 single-pass grating spectrometer with a liquid nitrogen cooled CCD camera was used to collect the Raman signal.

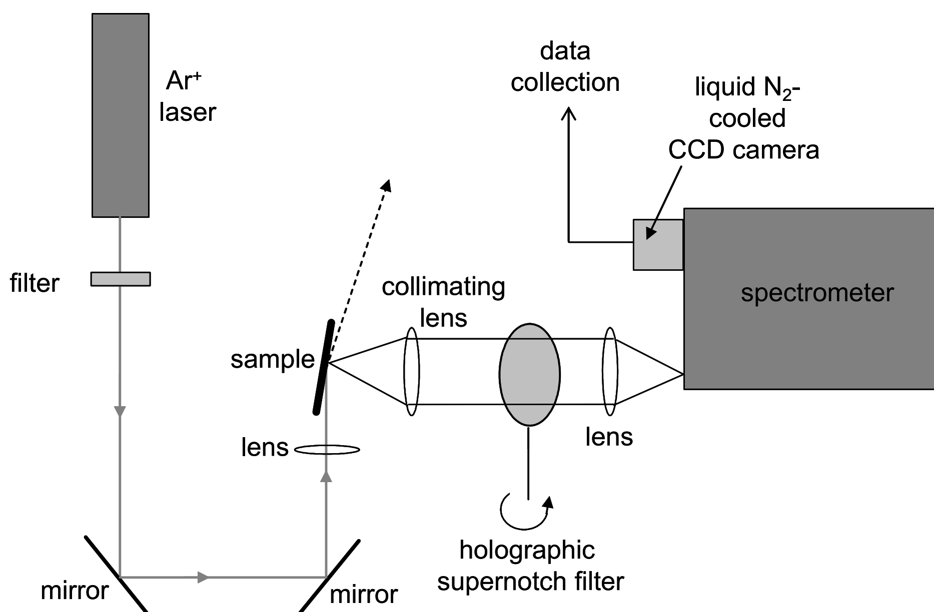

Figure 3.3: Schematic diagram of the Raman spectroscopy setup.

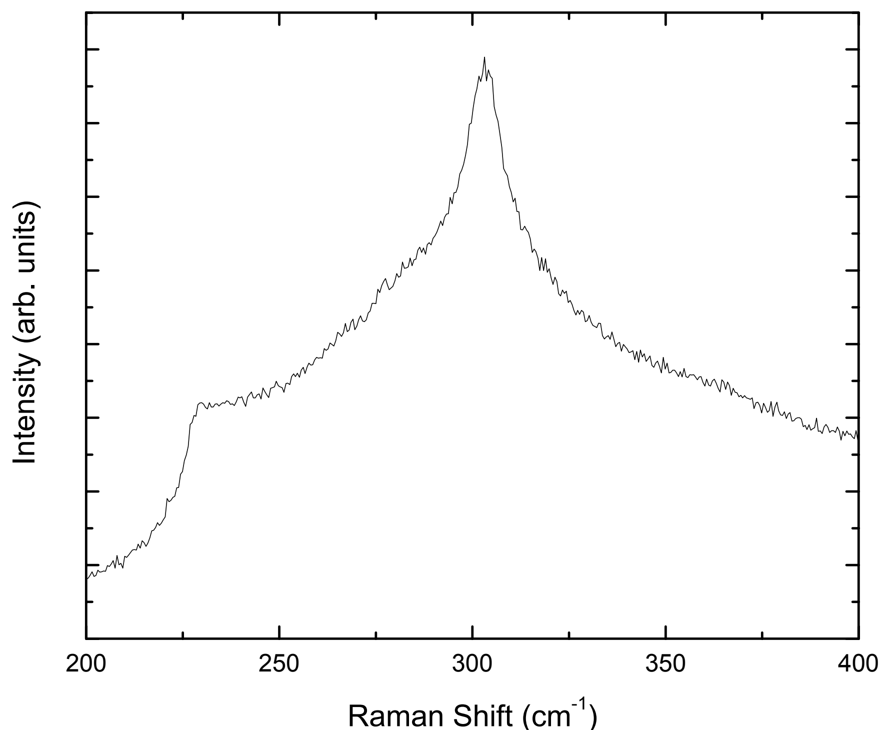

Figure 3.4: Raman spectrum of the second order Si phonon mode. This signal must be carefully subtracted to obtain the Ge nanocrystal Raman signal.

To isolate the Ge nanocrystal signal, it is necessary to perform a careful subtraction of the background signal. Figure 3.4 shows the second order Si Raman spectrum. This Si peak is located at approximately the same position as the Ge nanocrystal signal. Accurate subtraction is obtained by ensuring the background signal is level. It has been suggested by Kolobov *et al*.[41] that many reports of Raman spectra of Ge nanocrystals are false and correspond instead to the Si second order peak. To ensure that this is not the case in the present study, Raman spectra of both isotopically pure ^{70}Ge and ^{74}Ge nanocrystals were obtained. Figure 3.5 shows that the Raman line positions shift with isotope mass, as expected, confirming that measured spectra originate from the Ge nanocrystals.

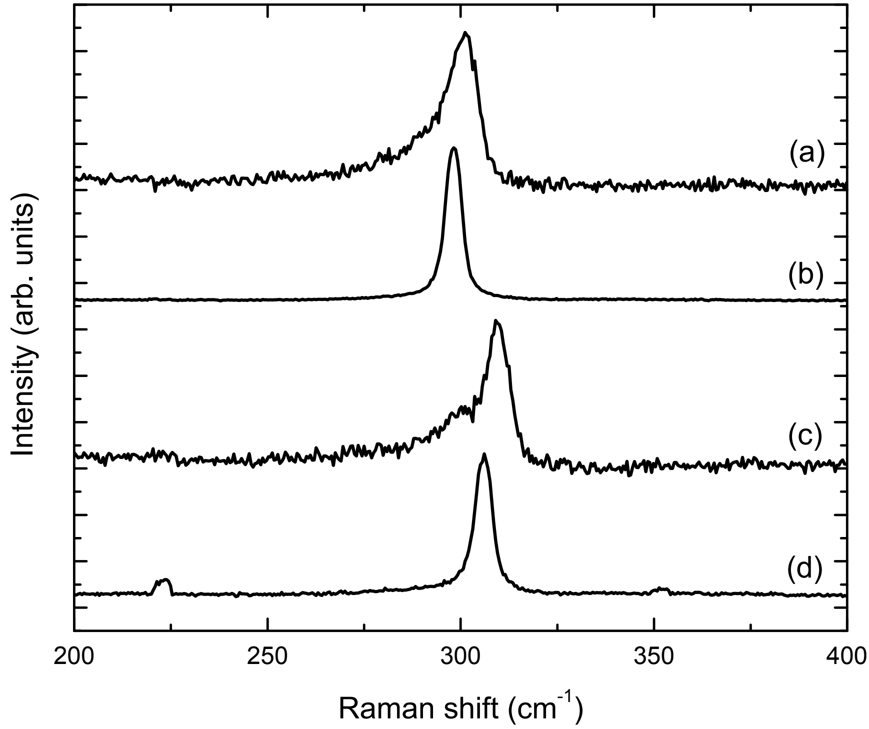

Figure 3.5: Raman spectra of ^{74}Ge nanocrystals (a), ^{74}Ge bulk (b), ^{70}Ge nanocrystals (c) and ^{70}Ge bulk (d). Asymmetric line broadening due to phonon confinement is observed in the nanocrystal samples. Nanocrystal peaks are blue shifted from the corresponding bulk peaks, indicating the presence of significant compressive stress.

3.3.2 Raman Spectroscopy in Bulk Crystals

In crystalline solids, Raman spectroscopy measures inelastically scattered light originating from optically driven vibrational transitions. Figure 3.6 shows a phonon dispersion curve for Ge in the [111] direction.[96] Since photons carry very little momentum, only zone center optical phonons ($\vec{k} = 0$) may be excited. In first order Raman scattering, an incident photon of frequency ω either creates (Stokes) or annihilates (anti-Stokes) a phonon of frequency Ω. Thus, scattered light is emitted with a frequency given by:

$$\omega' = \omega \pm \Omega \tag{3.1}$$

where the positive term corresponds to anti-Stokes scattering and the negative term corresponds to Stokes scattering. Since creation of a phonon is more probable than simultaneous interaction of the incident photon and an existing phonon, the Stokes line is more intense than the anti-Stokes line.[97] Therefore, the Stokes line is used for the detection of nanocrystals in this study.

The mass dependence of the zone center optical phonon frequency is[98]

$$\Omega \propto \frac{1}{M^{1/2}} \tag{3.2}$$

assuming an elemental material of mass *M*. As a result, Raman measurements are dependent upon the isotopic composition of the material under investigation. This unique

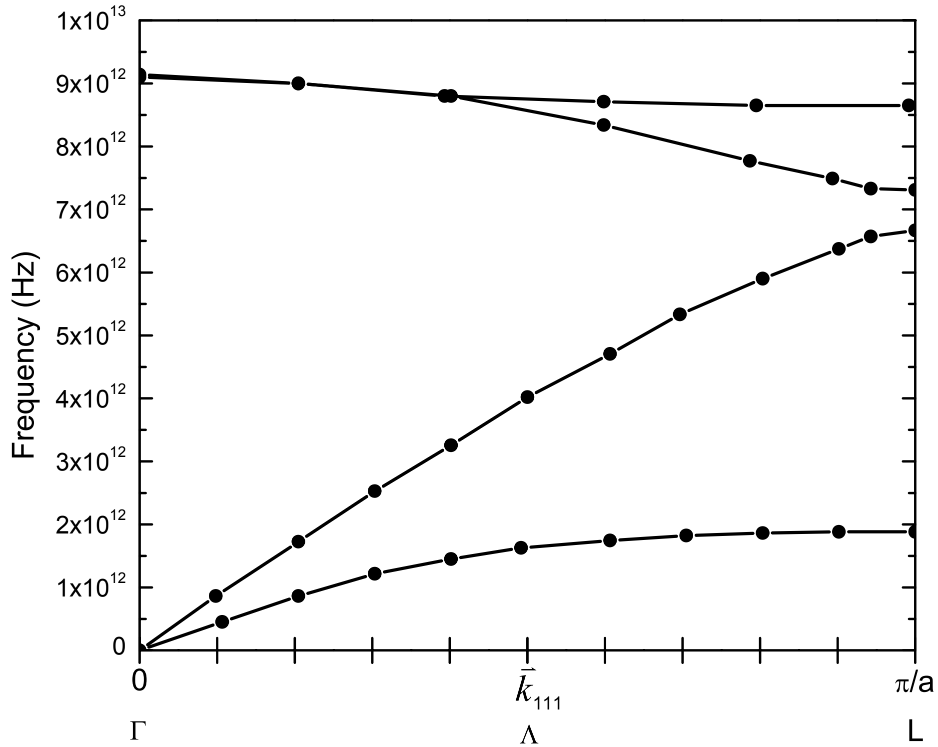

Figure 3.6: Ge phonon dispersion curve in the [111] direction. Data were obtained by Nilsson & Nelin using inelastic neutron scattering.[96]

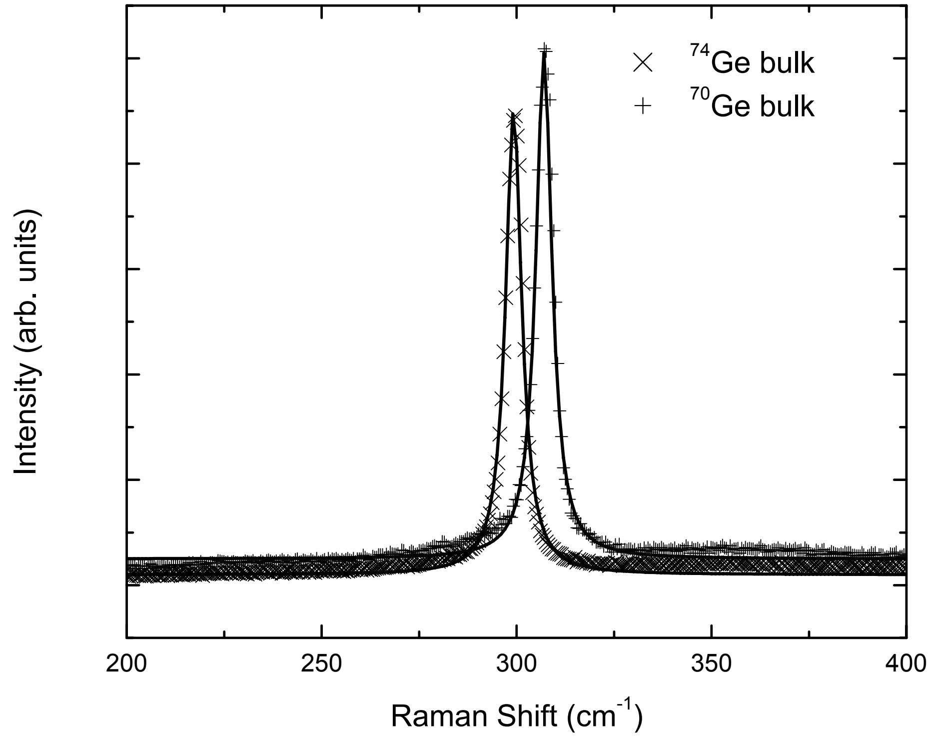

Figure 3.7: Raman spectra of isotopically enriched ^{70}Ge and ^{74}Ge bulk crystals. The solid lines give theoretical fits to the data using Equation 3.3. Results are consistent with Equation 3.2.

feature of Raman spectroscopy is particularly advantageous for the present study of isotopically pure Ge nanocrystals.

Raman spectra of bulk crystals are homogeneously lifetime broadened, resulting in the standard Lorentzian lineshape of the form:[99]

$$I(\omega) = \frac{1}{(\omega - \omega_0)^2 + \left(\frac{\Gamma_0}{2}\right)^2} \tag{3.3}$$

where $I(\omega)$ is the intensity (arbitrary units) as a function of the frequency ω, ω_o is the frequency corresponding to the $\vec{k} = 0$ transition, and Γ_o is the natural linewidth of the peak at the full width at half maximum (FWHM). Figure 3.7 shows Raman spectra obtained from isotopically enriched bulk Ge crystals. Also shown are Lorentzian fits to

the experimental data, using a natural linewidth of 5 cm^{-1}, which illustrate the validity of Equation 3.3. Line shifts are consistent with the predictions of Equation 3.2.

3.3.3 Phonon Confinement Effects

In an infinite crystal, phonons are described by Bloch waves of the form:[97]

$$\Phi(\vec{k}_0,\vec{r}) = u(\vec{k}_0,\vec{r})e^{-i\vec{k}_0\bullet\vec{r}} \tag{3.4}$$

where $u(\vec{k}_0,\vec{r})$ represents the displacement of an atom at the origin of a unit cell and has the periodicity of the lattice, $\vec{k}_0$ is the wavevector of the phonon in an infinite lattice, and $\vec{r}$ is the lattice vector. In nanocrystals, however, such a description no longer holds true, and phonons must be described as localized wavepackets within the nanocrystal.[100] The Heisenberg Uncertainty relation predicts that $\Delta k \Delta x \geq \hbar$. Therefore, as crystal dimensions are reduced, the selection rules governing optical transitions are relaxed and non-zone center optical transitions become allowed. As shown in Figure 3.6, the transitions away from $\vec{k} = 0$ are lower in energy than at the zone center. Therefore, an apparent red shift of the Raman spectrum occurs with decreasing nanocrystal sizes.

In order to describe confined phonons in nanocrystalline materials, it is necessary to add a phonon weighting function, $W(r,L)$, where L is the diameter of the nanocrystal. Consequently, the phonon wavefunction becomes:

$$\Psi(\vec{k}_0,\vec{r}) = W(r,L)\Phi(\vec{k}_0,\vec{r}) = \Psi'(\vec{k}_0,\vec{r})u(\vec{k}_0,\vec{r}) \tag{3.5}$$

Richter *et al.*[99] assumed a spherical crystal, which is proved in Chapter 3.4 to be a good approximation for the present case. In addition, they chose a Gaussian phonon weighting function of the form:

$$W(r,L) = Ae^{\frac{-2r^2}{L^2}} \tag{3.6}$$

This weighting function assumes that the surface boundary condition, which defines the surface phonon amplitude, is 1/e. Campbell *et al.*,[101] however, explored various forms of the phonon weighting function and argued that there is no physically justifiable reason to set the surface phonon amplitude to 1/e. Comparison with experimental data revealed that $\exp(-\alpha r^2 / L^2)$, does provide the best fit to experimental data but that a value of $\alpha =$ $8\pi^2$, which drives the surface phonon amplitude close to zero, is more appropriate. It will be shown in Chapter 4 that surface phonon modes of embedded nanocrystals are suppressed relative to those of free-standing nanocrystals. Uncertainty in choice of the surface boundary condition limits the applicability of this model for nanocrystal size determination.

Fourier series expansion of $\Psi'(\vec{k}_0, \vec{r})$ is required to obtain an expression for the intensity of Raman spectra as a function of frequency. This Fourier series expansion gives:

$$\Psi'(\vec{k}_0, \vec{r}) = \int C(\vec{k}_0, \vec{k}) e^{i\vec{k} \bullet \vec{r}} d^3 k \tag{3.7}$$

The functional form for the Raman line shape in terms of frequency for a system exhibiting phonon confinement is:[99]

$$I(\omega) = \int \frac{\left|C(0, \vec{k})\right|^2}{\left[\omega - \omega(\vec{k})\right]^2 + \left(\frac{\Gamma_0}{2}\right)^2} d^3 k \tag{3.8}$$

where $\omega(\vec{k})$ is the equation for the optical branch of the phonon dispersion curve. The Fourier coefficients, $C(\vec{k}_o, \vec{k})$, are given by the expression:

$$C(\vec{k}_0, \vec{k}) = \frac{1}{(2\pi)^2} \int \Psi(\vec{k}_0, \vec{r}) e^{-i\vec{k} \bullet \vec{r}} d^3 r \tag{3.9}$$

For the case of the weighting function proposed by Campbell *et al.*,[101] $W(r,L)=\exp(-8\pi^2r^2/L^2)$, and the Fourier coefficients are:

$$|C(0,k)|^2 \cong e^{-k^2L^2/16\pi^2} \tag{3.10}$$

Integration over the entire Brillouin zone would be rather complex because the phonon dispersion relations are anisotropic. For the present case, the Brillouin zone is assumed to be spherical and the phonon dispersion relations are assumed to be isotropic. This approximation is appropriate when the near-zone center optical phonons dominate the Raman signal.[100] As shown in the phonon dispersion curve in Figure 3.6, the difference between the phonon frequency at the zone center and at the zone edge is approximately 1.5×10^{12} s^{-1}, which would correspond approximately to a 48 cm^{-1} change in the Raman line position. Since the experimentally observed line broadening is only approximately 5 cm^{-1} – 10 cm^{-1}, this approximation is appropriate.

Raman spectra from ^{70}Ge and ^{74}Ge, shown in Figure 3.5, exhibit the asymmetric line broadening predicted by the phonon confinement model. Peaks are significantly blue shifted in relation to bulk spectra. The phonon confinement model, however, predicts red shifted peaks. This discrepancy is consistent with significant hydrostatic pressure on the as-grown nanocrystals.[102] As will be discussed in Chapters 4 & 5, this stress may be relieved through either selective removal of the oxide matrix or post growth thermal treatments.

Figure 3.8 shows the calculated FWHM and red shift of the Raman line as a function of nanocrystal diameter using Equations 3.8 & 3.10. This calculation is highly sensitive to the choice of the surface phonon amplitude boundary condition and the functional form for the phonon dispersion curve. Furthermore, experimental Raman

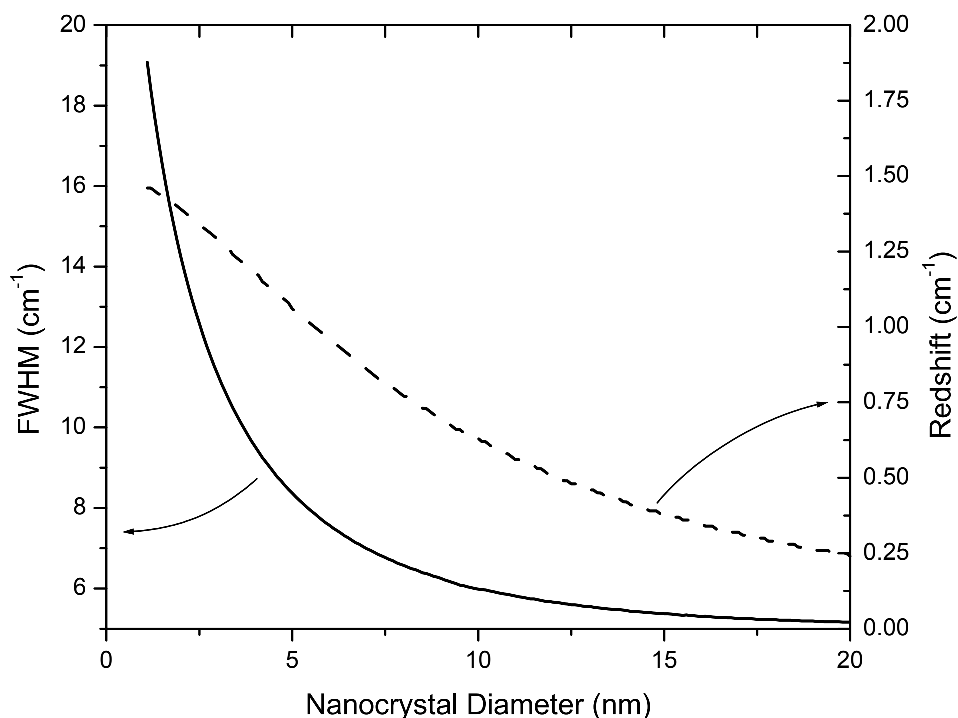

Figure 3.8: Calculated full width at half maximum (FWHM) and red shift of the Ge Raman line as a function of nanocrystal diameter using a natural linewidth of 5 cm^{-1}.

spectra are typically broadened further as a result of the nanocrystal size distribution and different sized nanocrystals are not equally sampled during measurement. Consequently, these calculations only provide a rough guide for the average nanocrystal diameter. More direct methods for measurement of the nanocrystal size distribution should be utilized when available. In the present study, Raman spectra of as-grown nanocrystal samples give a FWHM of approximately 9 cm^{-1}, which corresponds to a nanocrystal diameter of 4.5 nm. TEM measurements, which will be presented in Chapter 3.4, reveal that the true average nanocrystal diameter is 5.1 nm. Thus, these calculations provide a good rough approximation of the nanocrystal size, as expected. As will be discussed in Chapter 6, these calculations are inadequate to predict the nanocrystal red shift for the purpose of precisely determining the magnitude of stress exerted on nanocrystals.

3.4 Transmission Electron Microscopy

Transmission electron microscopy (TEM) provides a means to directly observe nanocrystals down to the atomic level. At low magnifications, it is possible to obtain nanocrystal size distributions and observe the entire growth region. High resolution TEM (HR-TEM) may be used to observe individual lattice planes. This makes it possible to determine the internal structures of the crystals, observe their shapes, and obtain information about their surfaces. TEM, therefore, is a powerful technique for materials characterization at the nanoscale. Unfortunately, sample preparation, which includes thinning to electron transparency, remains difficult and time consuming for the case of embedded nanocrystals. As a result, only a limited number of samples may be realistically imaged using this technique. For the case of free-standing nanocrystals, sample preparation can be significantly less difficult through use of electron transparent TEM grids. As will be shown in Chapter 4, it is possible to "liberate" nanocrystals from the SiO_2 matrix and transfer them to TEM grids for further characterization. Nevertheless, observation of nanocrystals within the matrix is essential to understanding the growth process and the properties of nanocrystals.

Cross sectional TEM of nanocrystals embedded in amorphous SiO_2 was performed in a Topcon 002B microscope with 200 keV electrons. Figure 3.9(a) shows a bright field image of the 500 nm silicon dioxide thin film on a silicon substrate after growth at 850 ^{o}C for 30 min. This image reveals an approximately 70 nm wide layer of nanocrystals in the near-surface region of the oxide film. No nanocrystals are observed in the top 50 nm of the sample. However, the Ge concentration in this region should be sufficient to produce nanocrystals. A similar observation was previously reported by

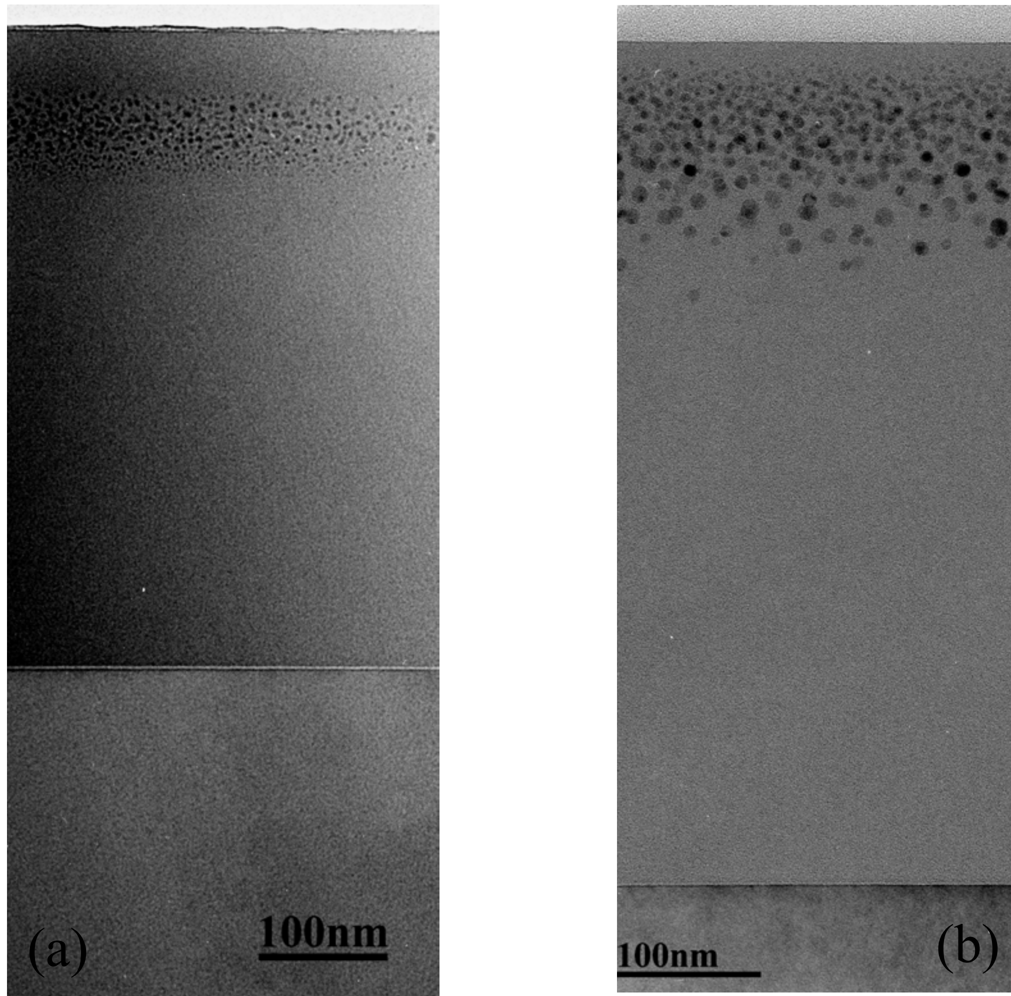

Figure 3.9: Transmission electron micrographs of as grown nanocrystals after annealing at 850 °C for 30 minutes (a) and 900 °C for 1 hour (b). Nanocrystals form bands near SiO_2 surfaces.

Heinig *et al.*,[103] who convincingly concluded that oxidation of Ge via in-diffusion of oxygen suppresses nanocrystal formation near the surface. The source of oxygen is likely residual moisture in the ampoule. Figure 3.9(b) shows a similar image for the case of a sample grown at 900 °C for 1 hr. Significant differences are observed for the two growth conditions. Larger nanocrystals and a wider growth band are observed for higher temperature annealing. For the 900 °C growth, particular care was taken to outgas the system through heating and extended pumping prior to sealing the ampoule. It appears these efforts were successful at decreasing the amount of oxygen in-diffusion as

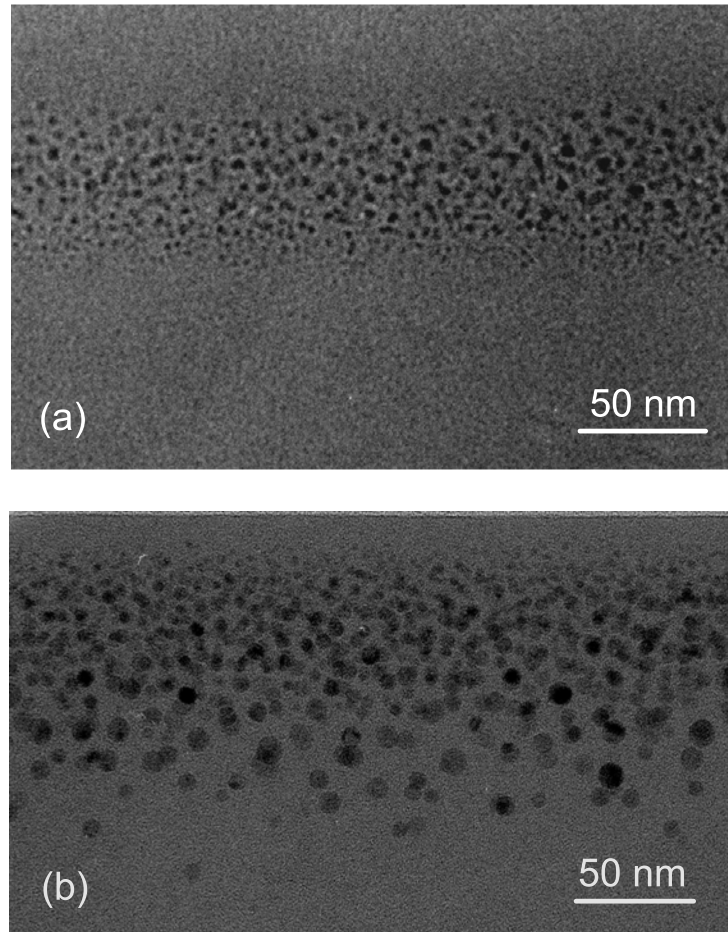

Figure 3.10: Transmission electron micrographs of the nanocrystal growth region for annealing at 850 °C for 30 minutes (a) and 900 °C for 1 hour (b). The surfaces of both samples are located at the top of the images.

evidenced by the growth of nanocrystals much closer to the surface than in the 850 °C sample.

Figure 3.10 shows the nanocrystal bands for the two growth conditions. Larger nanocrystals are observed for higher temperature annealing conditions. From such images, nanocrystal size distributions were determined. A histogram of nanocrystal sizes for the standard growth process (900 °C, 1hr) is shown in Figure 3.11. Nanocrystals have a mean diameter of 5.1 nm with a size distribution FWHM of 3.4 nm. This FWHM demonstrates that size distribution control of nanocrystals produced by ion implantation

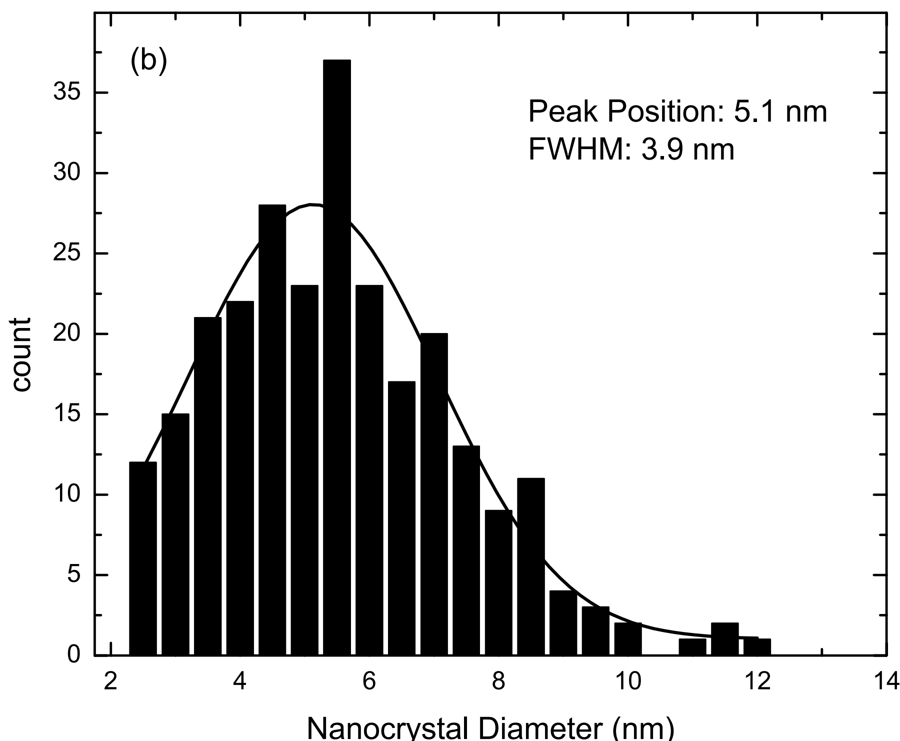

Figure 3.11: Nanocrystal size distribution obtained using transmission electron microscopy. Growth was performed at 900 °C for 1 hour.

is currently limited. Narrowing this distribution, perhaps by controlling stresses on nanocrystals (Chapter 6), will be a topic of future research.

HR-TEM images of individual nanocrystals are presented in Figure 3.12. Nanocrystals are spherical with sharp interfaces with the surrounding matrix. It has been suggested that nanocrystals are spherical as a result of liquid phase growth of Ge droplets. Upon cooling from the growth temperature, nanocrystals rapidly solidify and retain their spherical shape. However, in Chapter 5, significant evidence indicating the nanocrystals are solid at the growth temperature will be presented. Furthermore, Bording & Taftø[104] have performed molecular dynamics simulations of the growth of nanocrystals within an amorphous matrix, assuming solid phase growth. Their results predict the formation of spherical precipitates when the matrix is isotropic. It will be necessary to perform additional experiments to conclusively determine the growth phase. Both perfect

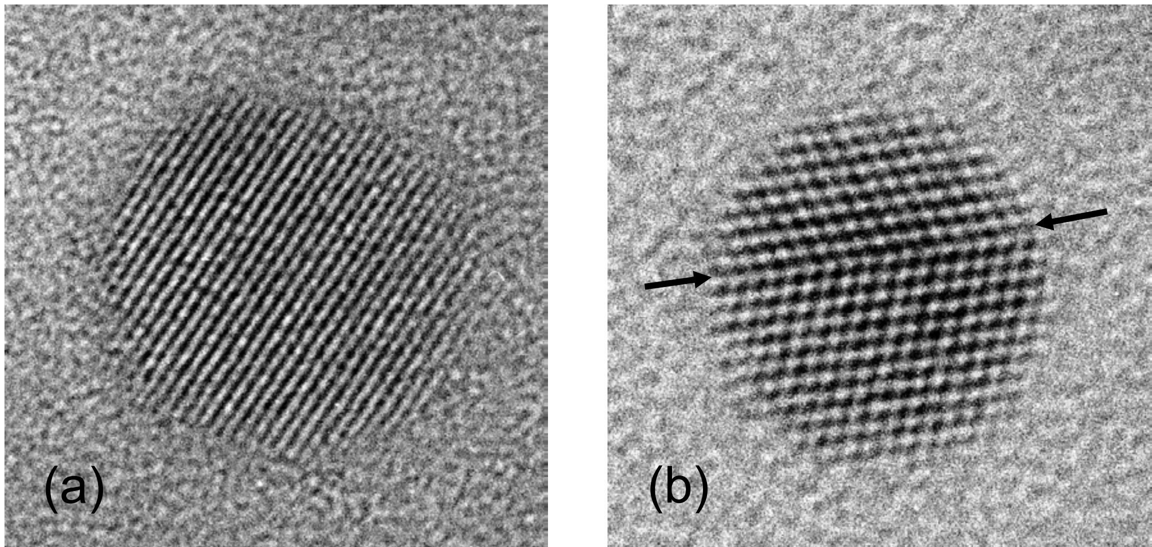

Figure 3.12: High resolution transmission electron micrographs of individual nanocrystals 9.8 nm in diameter (a) and 5.3 nm in diameter (b). The arrows in (b) indicate the location of a single twinning plane.

and twinned nanocrystals are observed. It is possible that twinning planes are formed to decrease the total energy of the system in the presence of the observed compressive stress, as suggested by Kolobov *et al*.[41]

4. Liberation and Manipulation of Nanocrystals

4.1 Introduction

With the exception of those synthesized by chemical means, semiconductor nanocrystals are typically embedded in a host matrix, usually SiO_2. While this may be desirable for the fabrication of conventional solid-state devices, it is not conducive to comprehensive surface and electronic characterization or direct manipulation. At present, only a limited number of optical and x-ray techniques are available for non-destructive characterization of nanocrystals embedded in oxide films. Therefore, it is desirable to develop a method to selectively remove the matrix and "liberate" the nanocrystals. Such a process will provide a means to directly and individually contact nanocrystals for electrical characterization, which will allow for study of quantum confinement effects and manipulation, which will allow for the formation of ordered two-dimensional structures. Successful liberation will also make it possible to manipulate large numbers of nanocrystals. For example, it is often desirable to transfer nanocrystals to other substrates for further characterization; Lacy carbon grids allow for rapid characterization using TEM, extremely flat and conducting substrates are required for Scanning Tunneling Microscopy (STM), and optically transparent substrates are required for absorption measurements. Once liberated, it will be possible to transfer nanocrystals to these, or other, substrates.

Two methods are currently available for determining the size distributions of nanocrystals: TEM and Raman spectroscopy. TEM requires painstaking sample preparation and has a very limited sampling of nanocrystal sizes. Fitting Raman spectra using the phonon confinement model is relatively inaccurate owing to the dependence of

the weighting function on the specific form of the confining function, as discussed in Chapter 3.2. Therefore, this method is typically only used to obtain a rough estimate of the average nanocrystal size. Using the liberation process, it will be possible to rapidly determine nanocrystal size distributions using an atomic force microscope (AFM). This technique has a number of advantages. AFMs are typically more accessible than TEMs, no arduous sample preparation is required, and there is virtually no limit to the sampling size. This final point is particularly advantageous, as it provides enhanced statistical reliability over any other existing technique.

As discussed in the previous chapter, Raman spectra indicate the presence of significant compressive stress on the as-grown nanocrystals. Removal of the oxide matrix will necessarily remove one source of compressive stress, thereby allowing for comprehensive characterization of the external pressure and determination of its magnitude. Comparing the stresses on relaxed nanocrystals within the matrix to liberated crystals also provides information about the Ge/SiO_2 interfacial energy relative to the Ge/air interfacial energy. At the nanoscale, the effects of surfaces often dictate the properties of the entire system. Thus, it will be particularly interesting to compare the properties of embedded nanocrystals to those of free-standing nanocrystals.

4.2 Experimental Procedure for Nanocrystal Liberation

Hydrofluoric acid (HF) is very effective at removing SiO_2, yet it leaves Ge essentially untouched. Therefore, HF was chosen as a suitable etchant for the selective removal of the matrix. HF etches SiO_2 through the following chemical reaction:

$$HF_{(v,l)} + SiO_{2(s)} \longleftrightarrow H_2O_{(l)} + SiF_{4(v)} \tag{4.1}$$

Liberation experiments were performed using two procedures. In the first set of

experiments vapor from 2:1 49% HF:H_2O solutions was used for etching and in the second set of experiments samples were immersed in a 1:1 49% HF:H_2O liquid solution. As will be shown, there are both benefits and drawbacks to each of these etching procedures. For most practical purposes, however, immersion in diluted liquid HF provides the best results.

For HF vapor etching experiments, samples were held approximately 2 cm above the surface of the HF solution. To remove the H_2O reaction product and ensure effective HF mass transport, the sample surface was purged with dry nitrogen at ten-second intervals throughout the etching process. For HF liquid etching experiments, samples were immersed in the HF solution and etching was terminated by placing the samples in methanol, followed by drying under flowing nitrogen.

Nanocrystals were removed from etched surfaces by 40 kHz sonication in methanol for times between 15 min and 60 min. Shorter sonication times were used to decrease the density of nanocrystals on the surface, whereas long times were used to completely remove nanocrystal films. Nanocrystals were transferred between surfaces by immersing a second substrate, initially free of nanocrystals, into the nanocrystal-containing solutions and evaporating away the methanol under flowing nitrogen.

Liberated nanocrystal films were primarily characterized by Raman spectroscopy and AFM. Raman was performed using the system and techniques described previously. AFM was performed on a Digital Instruments Dimension 3100 scanning probe microscope. All images shown here were obtained in tapping mode with Ultrasharp etched Si tips manufactured by MikroMasch. The tip radius was less than 10 nm and the

cantilevers had a resonant frequency at approximately 325 kHz and a force constant of 40 N/m.

Since the radius of the AFM tip, under perfect conditions, is approximately four times the radius of a nanocrystal of average size, it is not possible to obtain accurate in-plane (x-y plane) dimensional data. Under such conditions, images show the tip rather than nanocrystals. However, height data (z-direction) may provide extremely accurate information about nanocrystal sizes. When the radius of the tip is significantly smaller than the size of the object under investigation, which is not the case here, accurate in-plane data may be obtained. The height data, however, are unaffected by the tip radius and are therefore used for determination of nanocrystal size distributions. In-plane data, while not quantitatively accurate, do provide a good indication of the surface morphology and the inter-nanocrystal spacing.

4.3 Vapor Etching Results

There are two major benefits to using HF vapor for selectively etching the SiO_2 matrix. First, this process is significantly less aggressive than liquid etching so the thickness of SiO_2 removed may be easily controlled. If the surface atoms of the nanocrystals are not fully resistant to HF, the effect will be less pronounced during the less insidious vapor etching process. Second, immersion in solution followed by drying could introduce contaminants and lead to a loss of nanocrystals.

Contrary to the expected result, AFM data obtained after etching through the SiO_2 film to the underlying Si substrate indicate that the surface is extremely rough.[105] It is believed that implantation-induced damage to the SiO_2 and restructuring during thermal annealing results in the formation of an etch-resistant oxide phase that accumulates on the

surface as after etching. Formation of this phase is undesirable for most applications, most notably for manipulation of nanocrystals on the surface. However, since the vapor etching rate is well controlled, this process can be utilized to characterize the evolution of the Ge concentration profile after partial removal of the oxide film, thereby providing a means of determining Ge loss mechanisms that occur throughout the etching process.

Raman spectra show asymmetrically broadened peaks consistent with the phonon confinement model that confirm that nanocrystalline Ge is present on the surface during and after etching. These peaks also indicate that upon removal of the oxide matrix some of the compressive stress initially present in as-grown crystals is relieved. Raman spectra from liberated nanocrystals will be discussed at length in the following section on HF liquid etching.

RBS profiles of samples before and after etching of the SiO_2 matrix indicate that after complete removal of the oxide film, 76% of the total implanted Ge remains on the surface. Figure 4.1(a) shows RBS spectra from an as-grown sample and after etching of 53 nm, 59 nm, and 63 nm. Figure 4.1(b) shows RBS spectra from an as-grown sample and after etching of 140 nm and 410 nm. Prior to etching, the standard Ge concentration distribution, characteristic of as-grown samples, is observed in both figures. As etching proceeds, Ge accumulates on the surface. The tail observed in RBS spectra of etched samples [Figure 4.1(b)] is a consequence of the loose packing of Ge on the surface. Table 4.1 shows that all Ge loss occurs during etching of the first 140 nm. No Ge is lost upon further etching of the SiO_2. This suggests the Ge nanocrystals are impervious to the HF etchant and are not swept away during periodic purging with the nitrogen gun. Any Ge not found in nanocrystalline form, such as GeO_x in the near surface region

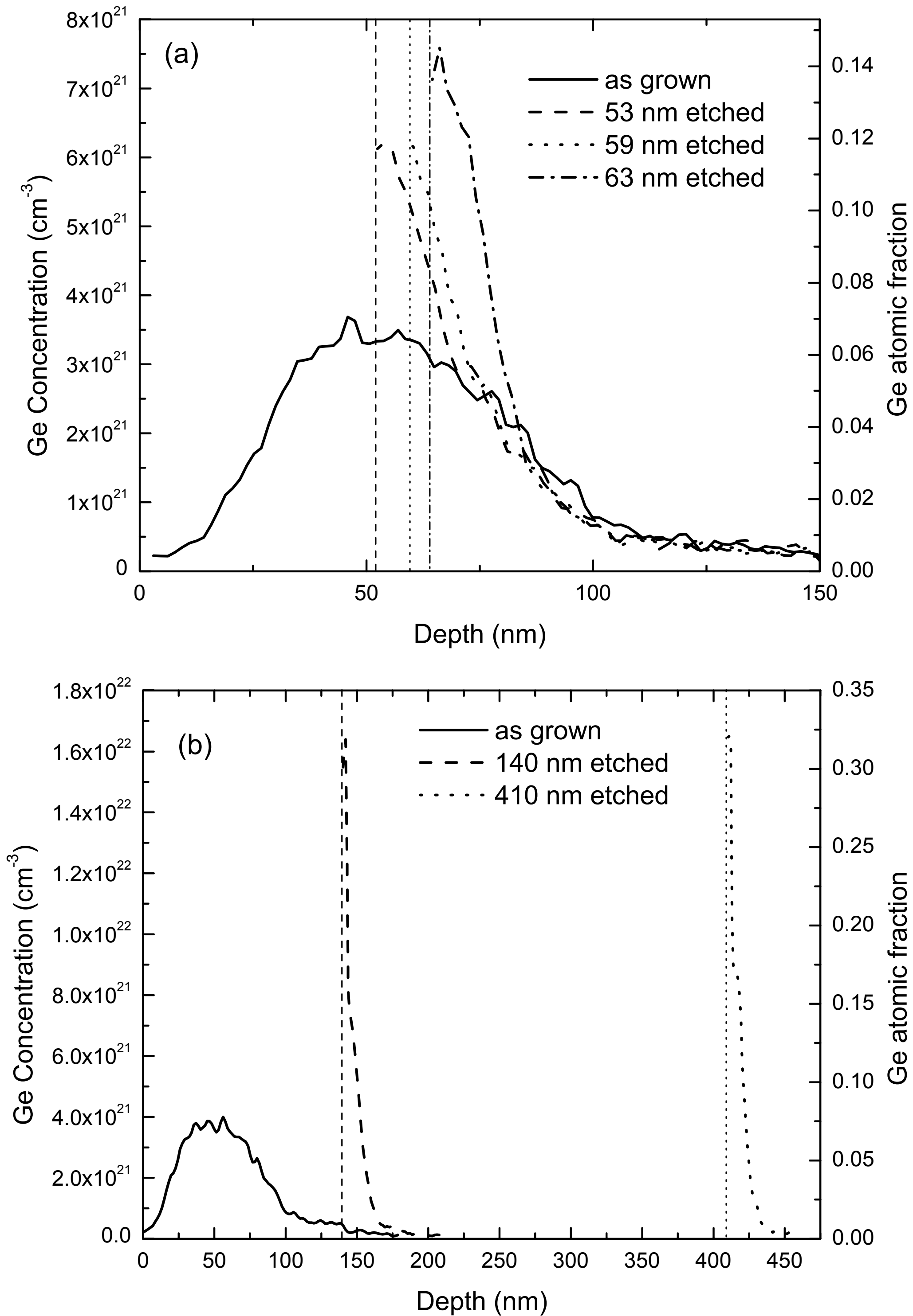

Figure 4.1: Ge concentration distributions obtained with Rutherford backscattering spectrometry. Vertical lines indicate the location of the surface after etching. Etching was halted after etching of 53 nm, 59 nm, and 63 nm (a) to determine Ge loss during etching through the growth region. Etching was halted after etching of 140 nm and 410 nm (b) to determine total Ge losses.

Table 4.1: Surface accumulated Ge after HF vapor etching.

Oxide Thickness (nm)	Thickness of Oxide Removed (nm)	Ge Content (cm^{-2})	Percent of Retained Ge
420	0	3.3×10^{16}	100%
367	53	2.9×10^{16}	88%
361	59	2.9×10^{16}	88%
357	63	2.8×10^{16}	85%
280	140	2.5×10^{16}	76%
10	410	2.5×10^{16}	76%

and isolated Ge atoms not bound to nanocrystals, is expected to be etched away along with the matrix. Table 4.1 shows that approximately 12% of the implanted Ge is lost after etching of 53 nm of oxide which is likely the result of GeO_x being removed from the near surface region. After etching of 140 nm of oxide, an additional 12% of the implanted Ge is lost, most likely due to isolated Ge atoms in the tail of the implant profile where nanocrystals do not nucleate.

4.4 Liquid Etching Results

Surface analysis via AFM of HF liquid etched samples reveals that, unlike the HF vapor etching case, no large SiO_2 particles accumulate on the surface. Furthermore, Raman spectroscopy confirms that nanocrystalline Ge is present on the surface after etching. Therefore, liquid etching is an effective means of liberating nanocrystals and provides surfaces suitable for surface characterization and manipulation. Therefore, the term “liberated” will, henceforth, be used to refer to nanocrystals that have been exposed via HF liquid etching.

AFM images indicate the presence of a nanocrystalline film on the surface of the etched sample, as shown in Figure 4.2. From this image, it is apparent that significant quantities of nanocrystals have collected on the surface. The crystals appear to be loosely

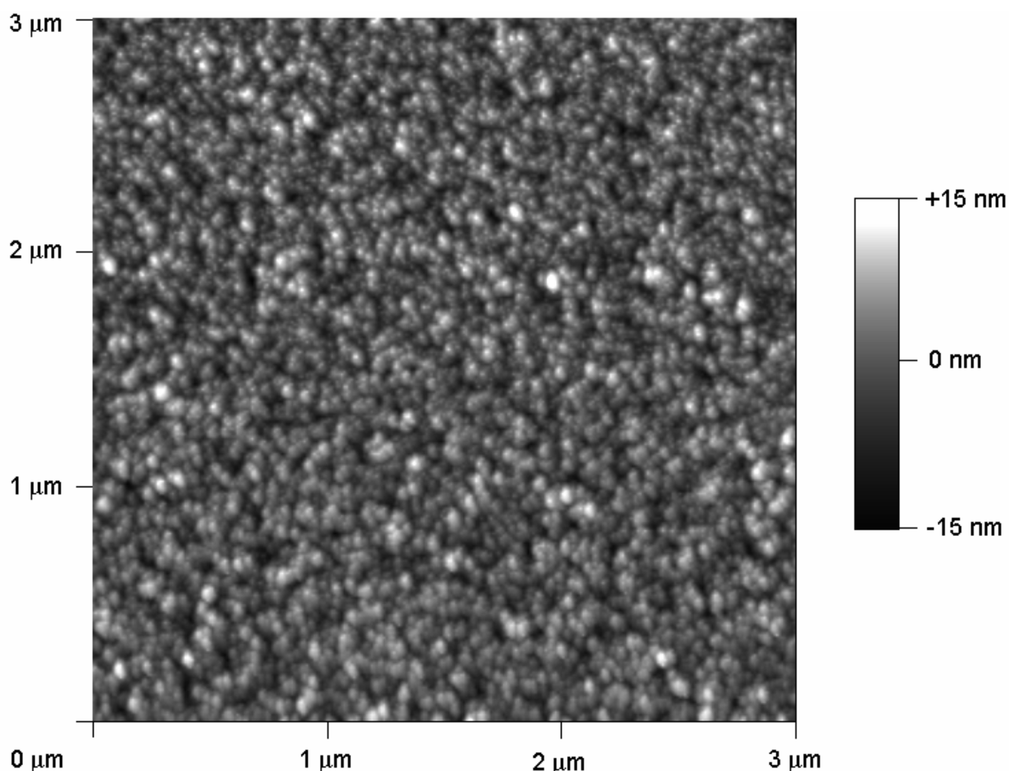

Figure 4.2: Atomic force microscope image of liberated Ge nanocrystals after removal of the oxide matrix via HF liquid etching. Ge nanocrystals accumulate in a loosely packed film on the surface of the sample. The high nanocrystal density precludes determination of nanocrystal size distributions.

packed and there is no indication of agglomeration into larger particles. Because of the high nanocrystal density immediately after etching, it is not possible to ascertain size distributions from images such as this. As discussed in Section 4.2, planar x-y data can not give an accurate measurement of the sizes of nanocrystals. Height data are not reliable with such high nanocrystal densities because there is no clear baseline. Nevertheless, the image does show nanocrystals with heights consistent with the expected size distribution.

As in the case of vapor etching, quantitative RBS data show that a significant fraction of the original Ge is retained on the surface after etching. Prior to etching, the total Ge content in the sample is 3.2×10^{16} cm^{-2} and after etching the total remaining Ge content is 2.2×10^{16} cm^{-2}. Therefore, after complete removal of the SiO_2 film, 69% of the

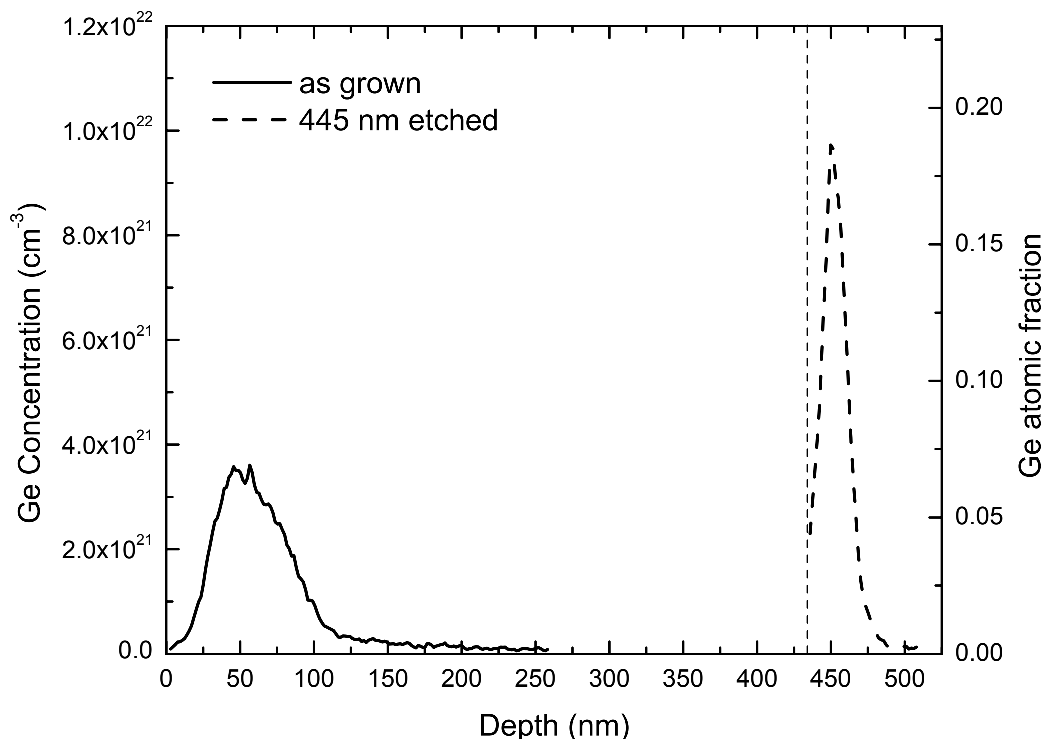

Figure 4.3: Ge concentration distributions obtained with Rutherford backscattering spectrometry after complete removal of the oxide matrix. The vertical line indicates the location of the surface after etching. The Ge distribution arises from the accumulation of a loosely packed Ge nanocrystal film on the surface.

initially implanted Ge is retained on the surface, as shown in Figure 4.3. For the case of HF vapor etching, 76% of the Ge remained after etching. Because the liquid etching process is much more rapid and less controlled than the vapor etching process, RBS data were not obtained for partial liquid etching through the oxide film. It is likely that the additional 7% loss during liquid etching is within the error between subsequent etching experiments and that Ge loss occurs according to the description given in the preceding section.

Comparison of RBS spectra obtained after complete removal of the oxide matrix via HF liquid etching (Figure 4.3) and HF vapor etching [Figure 4.1(b)] reveals that the surface Ge layer is much thicker and the peak Ge concentration is much lower after wet etching. This suggests the crystals are more loosely packed on the surface after liquid

etching, though it is not clear why this is the case.

While RBS is useful for measuring the total quantity of Ge retained on the surface and the corresponding concentration distribution, it does not provide any information regarding Ge crystallinity. Raman spectra, however, show conclusively that Ge retains its nanocrystalline structure subsequent to etching. Figure 4.4 shows Raman spectra obtained before [Figure 4.4(a)] and after [Figure 4.4(b)] etching along with an isotopically enriched ^{74}Ge bulk reference [Figure 4.4(c)]. As discussed previously, the as-grown nanocrystal line position is blue shifted in relation to both the bulk reference and the position predicted by the phonon confinement model due to compressive stress on the nanocrystals. As expected, selective removal of the oxide matrix relieves this

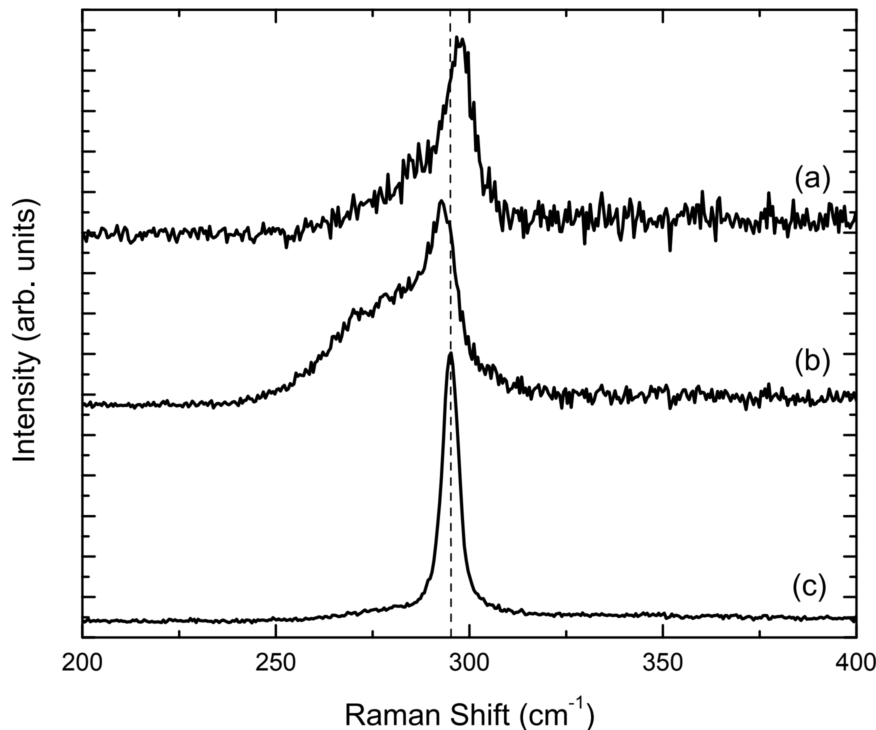

Figure 4.4: Raman spectra of embedded ^{74}Ge nanocrystals under compressive stress (a), liberated ^{74}Ge nanocrystals (b), and a ^{74}Ge bulk sample (c). The dashed vertical line indicates the position of the bulk Raman line. Liberation relieves the compressive stress present in as grown nanocrystals. Liberated spectra exhibit extended tails to lower frequencies that are likely due to surface phonon modes.

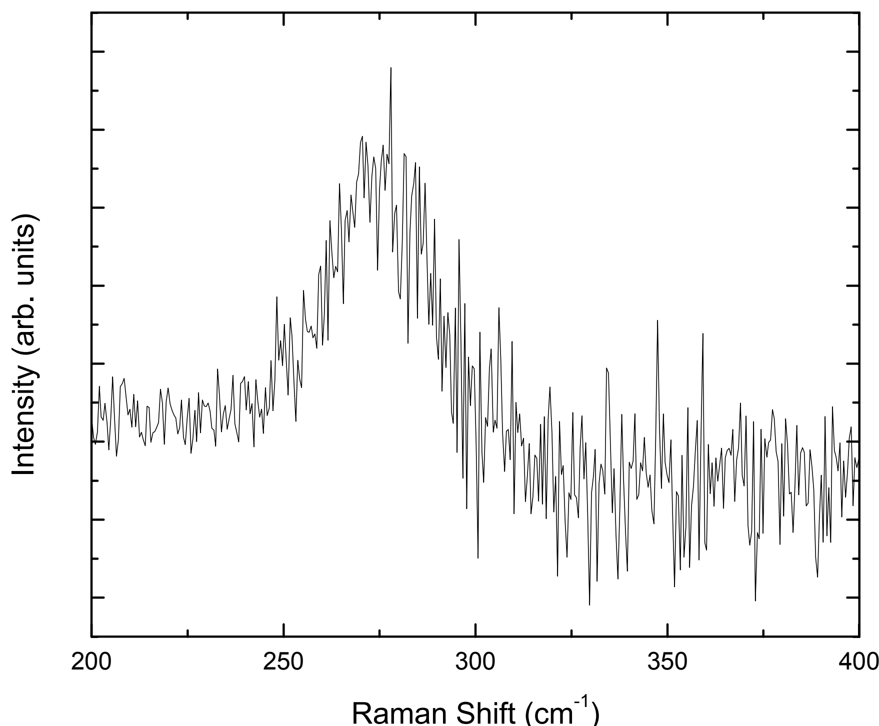

Figure 4.5: Raman spectrum obtained by subtracting the spectrum shown in Figure 4.4(a) from the spectrum shown in Figure 4.4(b) after shifting peak (a) to the same position as peak (b). Therefore, the signal from the low energy tail is isolated. The peak occurs at 276 cm^{-1}, which is close to the position of the amorphous Ge Raman line. This peak is attributed to low energy surface phonon modes which are suppressed for embedded nanocrystals due to interactions with the matrix.

stress. The Raman line position from the etched sample is red shifted with respect to the bulk reference sample as predicted by theory. Therefore, it is clear that the stress is not a fundamental property of the nanocrystals, but rather, it originates from the oxide matrix. The generation and relief of compressive stress will be discussed in detail in Chapter 6.

Raman spectra from etched samples exhibit extended tails to lower frequencies. Similar spectra were observed previously in Ge nanocrystals synthesized by co-sputtering.[100,106] Figure 4.5 shows a spectrum obtained by subtracting the Raman spectrum of the liberated crystals from that of the as-grown crystals. The as-grown spectrum was shifted such that the high energy shoulders of the two spectra coincide and subtraction could be performed appropriately. A broad, but distinct, peak is observed

with a maximum at approximately 276 cm^{-1}, which is consistent with the amorphous TO Ge mode reported by Lannin *et al.*[107] occurring at 275 cm^{-1}. However, since no amorphous Ge was detected in Raman spectra from as-grown samples and the etching process is not expected to amorphize the nanocrystals, the presence of a pure amorphous phase is not likely. Therefore, two possible sources of this spectral feature are considered: first, the peak may possibly arise from an altered nanocrystal size distribution, and second, it may be attributed to amorphous-like surface phonon modes predicted by a recent complete dynamical matrix calculation.[108]

If etching alters the size distribution by decreasing nanocrystal sizes, more pronounced phonon confinement would lead to additional line broadening. Therefore, two additional experiments were performed to determine whether nanocrystal sizes are reduced during the HF etching process, both of which indicate that the HF has a negligible impact on the size distribution. Samples were immersed in 60 mL of the 1:1 49% HF:H_2O etch solution for times ranging from 30 seconds to 1 hour. Raman line shapes did not vary with etching time. Also, AFM data taken from well-separated nanocrystals on flat substrates will be presented in Section 4.6 which show conclusively that the size distribution is left unaltered by the etching process.

The second possible cause of the observed Raman line shape is a change in the surface vibrational modes. Just after growth, the nanocrystals are embedded in a rigid silicon dioxide matrix that may dampen the vibrational modes of surface atoms through interface interactions. Furthermore, significant evidence shows that the embedded nanocrystals are under large compressive stresses which may further suppress lower energy surface vibrational modes. However, once the matrix is removed, surface atoms

are less tightly bound than the interior atoms and high amplitude and low energy phonons, similar to those in amorphous Ge, may be observed.[100] Conclusive evidence to support this theory is not yet available, and further experiments will be required to develop a complete understanding of the observed Raman line shapes. However, experiments to determine nanocrystal melting points, which will be discussed in Chapter 5, support the claim that low energy surface phonon modes are responsible for the observed spectral features.

Following the etching process, nanocrystals are expected to be hydrogen passivated and significant oxidation should not occur at short times. After extended exposure to oxygen, however, hydrogen passivation should break down and the nanocrystals oxidize. On bulk Ge, approximately 2-3 nm of native oxide forms upon exposure to air.[109] If Ge nanocrystals behave similarly to their bulk counterpart, all but the largest crystals should be fully consumed by oxidation. However, it has been shown that formation of a self-limiting native oxide that is significantly thinner than the bulk native oxide is possible in nanocrystalline systems.[110] Since oxides of Si and Ge have greater volumes than the elemental materials, oxidation of a particle or wire with a high radius of curvature necessarily introduces strain into the oxide shell.[110] This strain, in turn, may reduce the diffusivity of oxygen through the shell and limit the native oxide thickness at room temperature.

To determine the stability of free-standing nanocrystals, Raman spectroscopy was performed before and after liberated samples were exposed to ambient atmospheric conditions for extended times. The maximum exposure time investigated was 5 weeks. No significant changes in Raman line shapes or positions are observed after any exposure

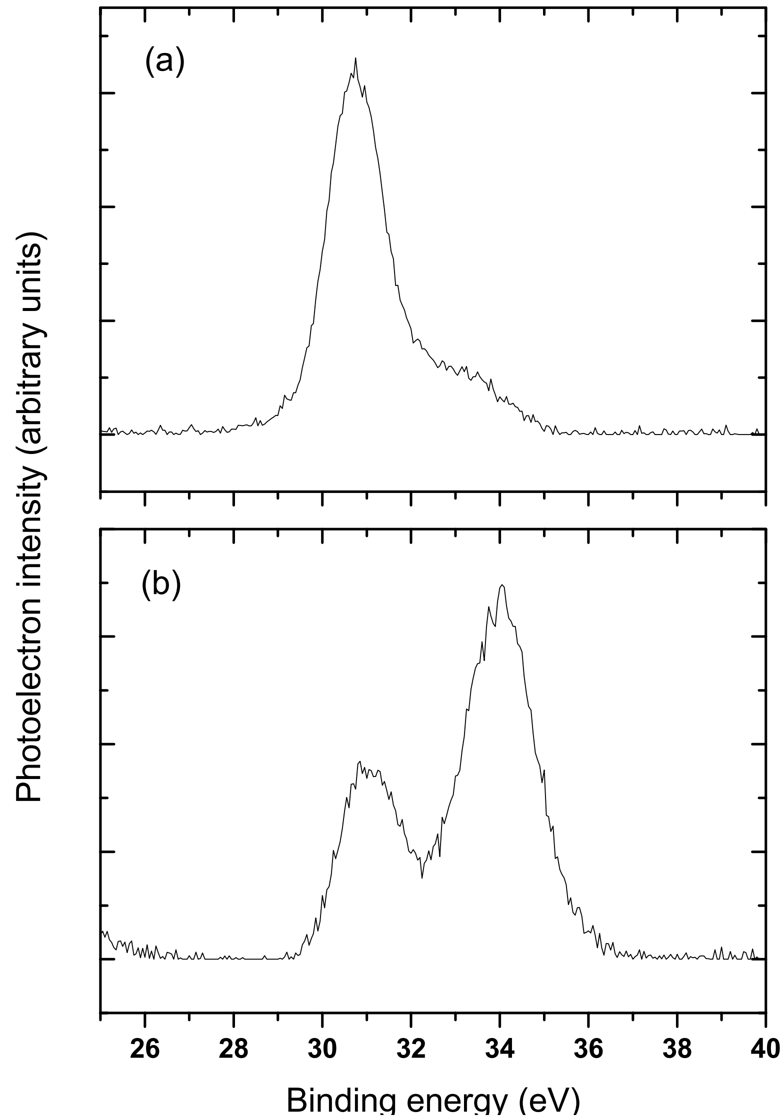

Figure 4.6: Ge 3d XPS spectra of exposed nanocrystals immediately after (a) and 47 days after (b) selective removal of the SiO_2 matrix. The lower energy peak corresponds to Ge-Ge bonding in the nanocrystals. The higher energy peak in (b) is consistent with the presence of Ge oxide.

time. Therefore, the nanocrystals appear to be stable in air and oxidation does not seem to be sufficient to alter significantly nanocrystal sizes.

As shown in Figure 4.6(a), XPS indicates very little oxidation of nanocrystals after a few hours of exposure to ambient conditions. A strong signal is observed at approximately 30.7 eV resulting from Ge-Ge bonding in the nanocrystals. This peak is shifted from the reference value at 29.5 eV. A similar shift was seen in the XPS study of

Ge nanocrystals conducted by Borodin et al.,[111] though its origin is not yet known. A slight shoulder is observed at higher energy which is consistent with the presence of a small quantity of Ge oxide. However, the intensity of the oxide peak is extremely low and hydrogen passivation is considered to be effective. Additional oxidation is observed after 47 days of exposure to ambient conditions, as shown by the XPS spectrum in Figure 4.6(b). However, since no additional broadening is observed in the Raman signal, the native oxide thickness must be considerably thinner than that observed on planar bulk Ge samples. Despite the significant rise of the Ge-O peak, it is likely this XPS spectrum is dominated by the chemical states of the outermost atoms of the nanocrystals since a significant fraction lie on the surface (Figure 1.1). Due to the size distribution of nanocrystals, it is difficult to determine quantitatively the oxide thickness from these XPS data alone and further work will be required to determine the dynamics of native oxide formation.

4.5 Van der Waals Interaction Forces

Nanocrystals accumulate on the surface during the etching process, and are preserved afterwards, most likely because of van der Waals attractions to the substrate and to each other. Van der Waals dispersion forces, also called London forces, arise from instantaneous dipole-dipole interactions. At any instant, there exists a dipole within all atoms and molecules, regardless of whether they are polar or non-polar. This instantaneous dipole influences the electron clouds of surrounding atoms, and may lead to either attractive or repulsive forces that have a finite value when averaged over time. Such forces are responsible for condensation of non-polar atomic and molecular gases, though they are typically quite weak; helium condensation, for instance, occurs at 4.2 K.

Nevertheless, these attractive forces become quite important at the nanometer scale.

The theory of van der Waals dispersion forces between atoms and molecules may be readily extended to the case of larger bodies, such as the interaction of two nanocrystals or the interaction of a nanocrystal and a substrate. The pair potential arising from van der Waals interactions between two atoms or molecules is given by:[112]

$$U(d) = -\frac{C}{d^6} \tag{4.2}$$

where C is a constant and d is the interaction length. In the simplest case, we assume the van der Waals forces between larger bodies are assumed to be equal to the sum of contributions from each individual atom in the system. This approximation assumes that each atom interacts with each of the others independently, and the effect of the medium is not considered. Nevertheless, this approximation yields useful results and the resulting errors may be straightforwardly accounted for later. A full derivation of the expression for interaction forces between two particles and between a particle and a substrate may be found in Appendix A. For the case of two interacting particles, integration of the forces between atoms over all atoms in the system yields an expression for the total pair potential which may be expressed as:[113]

$$U(D) = -\frac{A}{12}\left\{\frac{y}{x^2+xy+x} + \frac{y}{x^2+xy+x+y} + 2\ln\left(\frac{x^2+xy+x}{x^2+xy+x+y}\right)\right\} \tag{4.3}$$

The bracketed term is simply a geometrical factor, general to all particle/particle interactions, with x and y defined as follows:

$$x = \frac{D}{2R_1} \quad \text{and} \quad y = \frac{R_2}{R_1}$$

where D is the interparticle separation and R_1 and R_2 are the particle radii. The prefactor,

A, is known as the Hamaker constant. This term contains information specific to the materials in the system under consideration and its formulation will be discussed shortly.

For the case of a particle interacting with a flat surface, Equation 4.3 may be simplified by allowing $y \to \infty$. The resulting equation gives the pair potential between a small spherical particle and a flat surface:[113]

$$U(D) = -\frac{A}{12}\left\{\frac{1}{x} + \frac{1}{x+1} + 2\ln\left(\frac{x}{x+1}\right)\right\} \qquad (4.4)$$

Simple forms of the Hamaker constant exist, but they are not capable of accounting for van der Waals interactions in the presence of a third medium. Using a formulation derived through the so-called Lifshitz theory, it is possible to obtain a Hamaker constant that both accounts for the presence of a third medium and corrects for errors introduced in the initial approximation of independent interaction between individual atoms.[112] Assuming two bodies (either particle-particle or particle-surface) with dielectric constants $\varepsilon_1(i\nu_n)$ and $\varepsilon_2(i\nu_n)$ are interacting through a medium with a dielectric constant $\varepsilon_3(i\nu_n)$, the Hamaker constant is given by:[112]

$$A = \frac{3}{4}k_B T\left[\frac{\varepsilon_1 - \varepsilon_3}{\varepsilon_1 + \varepsilon_3}\right]\left[\frac{\varepsilon_2 - \varepsilon_3}{\varepsilon_2 + \varepsilon_3}\right] + \frac{3h}{4\pi}\int_{\nu_1}^{\infty}\left[\frac{\varepsilon_1(i\nu) - \varepsilon_3(i\nu)}{\varepsilon_1(i\nu) + \varepsilon_3(i\nu)}\right]\left[\frac{\varepsilon_2(i\nu) - \varepsilon_3(i\nu)}{\varepsilon_2(i\nu) + \varepsilon_3(i\nu)}\right]d\nu \qquad (4.5)$$

where ε_j is the static dielectric constant of medium *j*, $\varepsilon_j(i\nu)$ is the dielectric constant evaluated at the imaginary frequency $i\nu$, and ν_i is 4×10^{13} s^{-1} at 300 K.[112] The integral may be evaluated by expressing $\varepsilon_j(i\nu)$ as:[112]

$$\varepsilon_j(i\nu) = 1 + \frac{\left(n_j^2 - 1\right)}{\left(1 + \frac{\nu^2}{\nu_{e,j}^2}\right)} \qquad (4.6)$$

Table 4.2: Static dielectric constants and indices of refraction for the calculation of van der Waals forces.[93]

Material	ε	n
Ge	16.0	4.01
Si	12.1	3.4
SiO_2	3.81	1.45
HF	83.6	9.14
MeOH	33	5.74
air	1	1

where n_j and $v_{e,j}$ are the refractive index and the main UV absorption frequency of medium j, respectively. The quantity $v_{e,j}$ is typically assumed to be approximately 3×10^{15} s^{-1}.[112] Table 4.2 gives the values for the static dielectric constant and the index of refraction required to calculate the Hamaker constant for systems involving interactions between Ge, Si, SiO_2, HF, MeOH, and air.[93] The van der Waals pair potential between two interacting bodies may be calculated using either Equation 4.3 or 4.4, depending on the geometry. The force between the bodies is calculated in the normal fashion:

$$F = -\frac{dU(D)}{dD} \tag{4.7}$$

Table 4.3 displays the Hamaker constants, van der Waals pair potentials, and van der Waals forces for all interactions that occur during the processing and characterization of liberated nanocrystals, assuming an interaction length of 0.3 nm. All interaction energies are attractive and significantly larger than k_BT at room temperature. Hence, nanocrystals are retained on surfaces during processing.

During the etching process, nanocrystals accumulate on the surface as a result of their strong attraction to the underlying SiO_2 substrate and to one another. Indeed, the high dielectric constant of HF leads to extremely large pair potentials. Therefore, initial concerns that the nanocrystals would be "swept" away during immersion in the liquid

Table 4.3: Hamaker constants, pair potentials, and van der Waals forces for nanocrystal interactions in various media.

Medium 1	Medium 2	Medium 3	A ($/k_BT$)	U ($/k_BT$)	F (dyn)
Ge nanocrystal	Si substrate	HF	321	-325.5	5.7×10^{-4}
Ge nanocrystal	Si substrate	MeOH	71	-72.0	1.3×10^{-4}
Ge nanocrystal	Si substrate	air	180	-182.5	3.2×10^{-4}
Ge nanocrystal	SiO_2 substrate	HF	393	-398.5	6.9×10^{-4}
Ge nanocrystal	SiO_2 substrate	MeOH	123	-124.7	2.2×10^{-4}
Ge nanocrystal	SiO_2 substrate	air	49	-49.7	8.7×10^{-5}
Ge nanocrystal	Ge nanocrystal	HF	291	-114.1	8.9×10^{-5}
Ge nanocrystal	Ge nanocrystal	MeOH	53	-20.8	1.6×10^{-5}
Ge nanocrystal	Ge nanocrystal	air	204	-80.0	6.2×10^{-5}
Ge nanocrystal	Si AFM tip	air	180	-134.8	1.8×10^{-4}

prove to be unfounded. After etching, multiple layers of nanocrystals accumulate on the surface. Therefore, nanocrystals which are imaged with the AFM are attracted not to the underlying substrate, but rather to underlying nanocrystals. Comparison of the van der Waals AFM tip/nanocrystal and nanocrystal/nanocrystal forces reveals that there is a net attraction to the scanning tip. This would suggest that nanocrystals would leave the surface during imaging. In truth, each nanocrystal interacts with a number of other crystals on the surface and it is possible to image the nanocrystals without accumulation on the AFM tip. However, it is observed experimentally that nanocrystals occasionally stick to the surface of the scanning tip, as evidenced by double imaging of individual crystals. This observation is consistent with the data presented in Table 4.3.

The van der Waals attraction between an isolated nanocrystal and a Si substrate is larger than the attraction between a nanocrystal and the AFM tip. Thus, development of a process to obtain isolated nanocrystals should allow imaging of single nanocrystals. This prediction is confirmed by the results presented in the next section, Chapter 4.6.

Equation 4.5 predicts that the Hamaker constant will be negative for cases in

which the dielectric constant of the medium through which interaction occurs, ε_3, is intermediate between the dielectric constants of the two interacting bodies.[112] Van der Waals forces are repulsive for such a case. This effect provides a possible method for large scale patterning of nanocrystals. For instance, a silicon wafer could be patterned with a material having a very high dielectric constant that is resistant to HF etching and thermal treatments. Such materials, which include novel oxides and perovskites, are currently being explored in the microelectronics industry. Silicon dioxide could then be deposited above this layer and nanocrystals could be formed in the usual fashion. Upon etching, nanocrystals would be attracted to regions of exposed silicon, but repulsed from the patterned regions. An alternate procedure would be to immerse the etched and patterned sample in a medium with an appropriately chosen dielectric constant. This would provide more versatility for selection of the patterning material. Future experiments will explore this proposed method of nanocrystal patterning.

4.6 Removal, Transfer, and Manipulation of Liberated Nanocrystals

To determine nanocrystal size distributions using AFM, it is necessary to reduce the density of nanocrystals on the surface such that isolated nanocrystals can be imaged on a smooth substrate. Furthermore, it is desirable to transfer nanocrystals to other surfaces, such as TEM grids and conducting substrates, for further characterization. To overcome the van der Waals binding forces calculated in the previous section, 40 kHz ultrasonic cleaning in a methanol bath was chosen since interactions in methanol are relatively weak. Aggregation of nanocrystals is not expected during this process since energy is continually deposited into the methanol solution.

After sonication of etched samples for 15 min, some nanocrystals are retained on

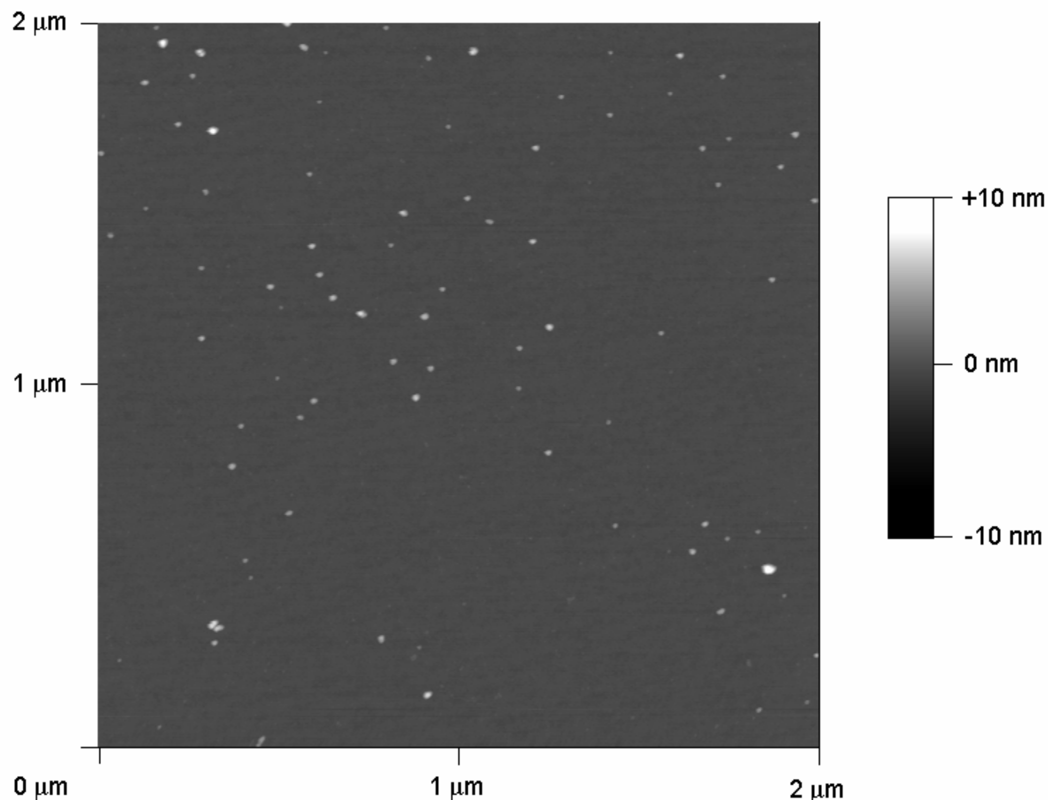

Figure 4.7: Atomic force microscope image of isolated Ge nanocrystals on a Si substrate obtained after HF liquid etching of the oxide matrix followed by sonication in methanol. Compiled height data are used to accurately determine size distributions.

the surface, but most crystals are removed to the solution. Figure 4.7 shows that such a treatment allows for the imaging of isolated nanocrystals. The Si substrate has sub-nanometer roughness, so it is possible to obtain the diameters of individual nanocrystals by analyzing the height as measured by the AFM. Multiple images such as that shown in Figure 4.7 were obtained at random locations on the surface of the sample. Figure 4.8(a) shows a histogram of compiled AFM height data and Figure 4.8(b) shows a histogram of nanocrystal diameters obtained from TEM. Both histograms have been fit with Gaussian curves. Both the mean nanocrystal diameter and the FWHM of the size distributions are in excellent agreement. These results show conclusively that nanocrystal size distributions are not significantly affected by the HF etching process. As a consequence,

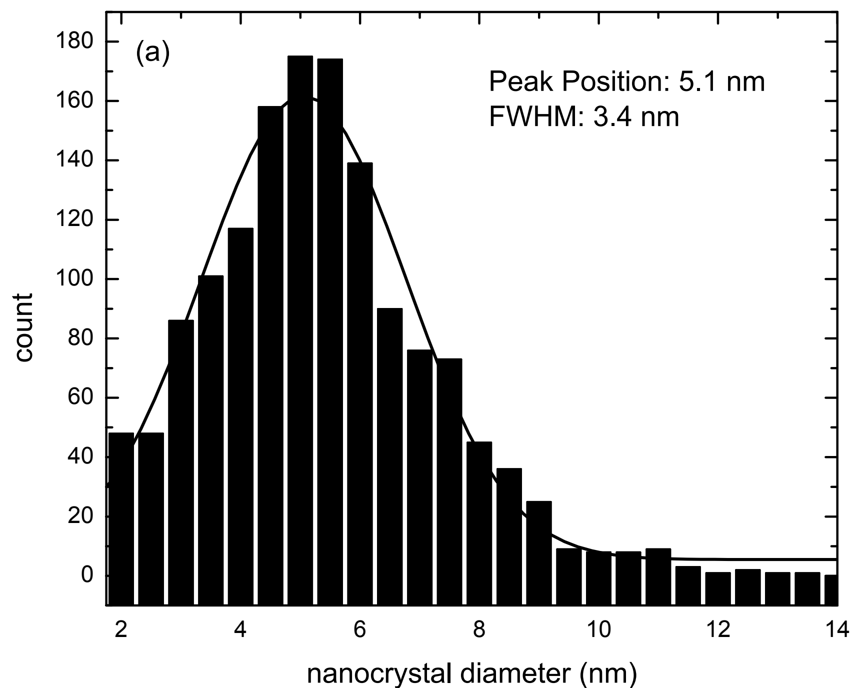

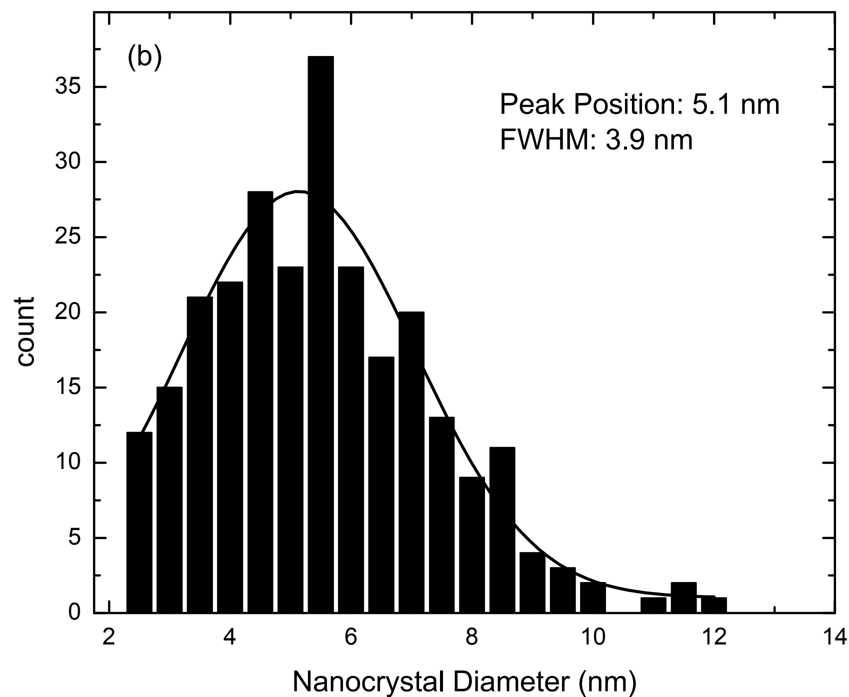

Figure 4.8: Nanocrystal size distributions obtained using atomic force microscopy (a) and transmission electron microscopy (b). The liberation and sonication procedure preserves the nanocrystal sizes, thus allowing AFM to be used for rapid determination of nanocrystal size distributions.

it will be possible to compare directly liberated and embedded nanocrystals to ascertain the effects of pressure and surface termination on their properties.

Using the technique of liberating nanocrystals, decreasing their surface density through ultrasonic treatment, and imaging them using an AFM, nanocrystal size distributions may be determined directly without the aid of a TEM. This finding will allow for the rapid determination of nanocrystal size distributions. It will, therefore, be possible to conduct an array of studies exploring the effects of various processing procedures and oxidation on nanocrystal size distributions. Such studies will be pursued in the future.

Nanocrystals may be transferred between surfaces by immersion of a second substrate in the nanocrystal-containing methanol solution directly after sonication. Figure 4.9 shows an electron diffraction pattern of Ge nanocrystals that have been

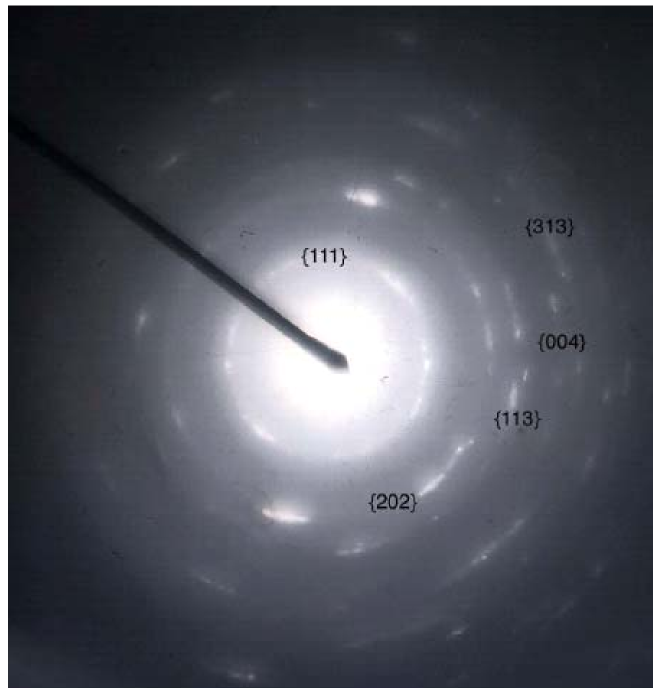

Figure 4.9: Electron diffraction pattern obtained in a transmission electron microscope after transfer of nanocrystals to a Lacy carbon grid using the HF etching and methanol ultrasonic cleaning process.

transferred to a Lacy carbon grid using this process. Because there is no preferential crystallographic alignment of nanocrystals, a powder-like electron diffraction pattern is observed. This transfer process may be useful for more rapid TEM characterization of nanocrystals. Furthermore, this may allow for the transfer of nanocrystals to atomically smooth and conducting substrates for scanning tunneling microscopy (STM) of individual nanocrystals. This could provide significant information about the electronic structure and surface properties of nanocrystals as a function of their size.

Using AFM, it should be possible to directly manipulate nanocrystals on a substrate. So-called nanomanipulation has been achieved for the case of exposed Si nanocrystals formed via gas evaporation.[114] Use of this procedure in the present case would provide a means to “push” single nanocrystals between patterned contacts for electrical measurements and form ordered 1-D and 2-D nanocrystal arrays to study the interactions between nanocrystals. Though this has not been done with liberated nanocrystals to date, initial results from standard AFM scans suggests that it will be possible. Figure 4.10 shows two AFM scans. In the first scan, which was obtained in tapping mode, some nanocrystals are observed to move across the surface in response to the AFM tip. In the second scan, the nanocrystals have assumed new positions as a result of this movement. Control of nanocrystal motion on the substrate has not been achieved through the course of the present study, but in the future, contact mode AFM will be used to manipulate the positions of nanocrystals.

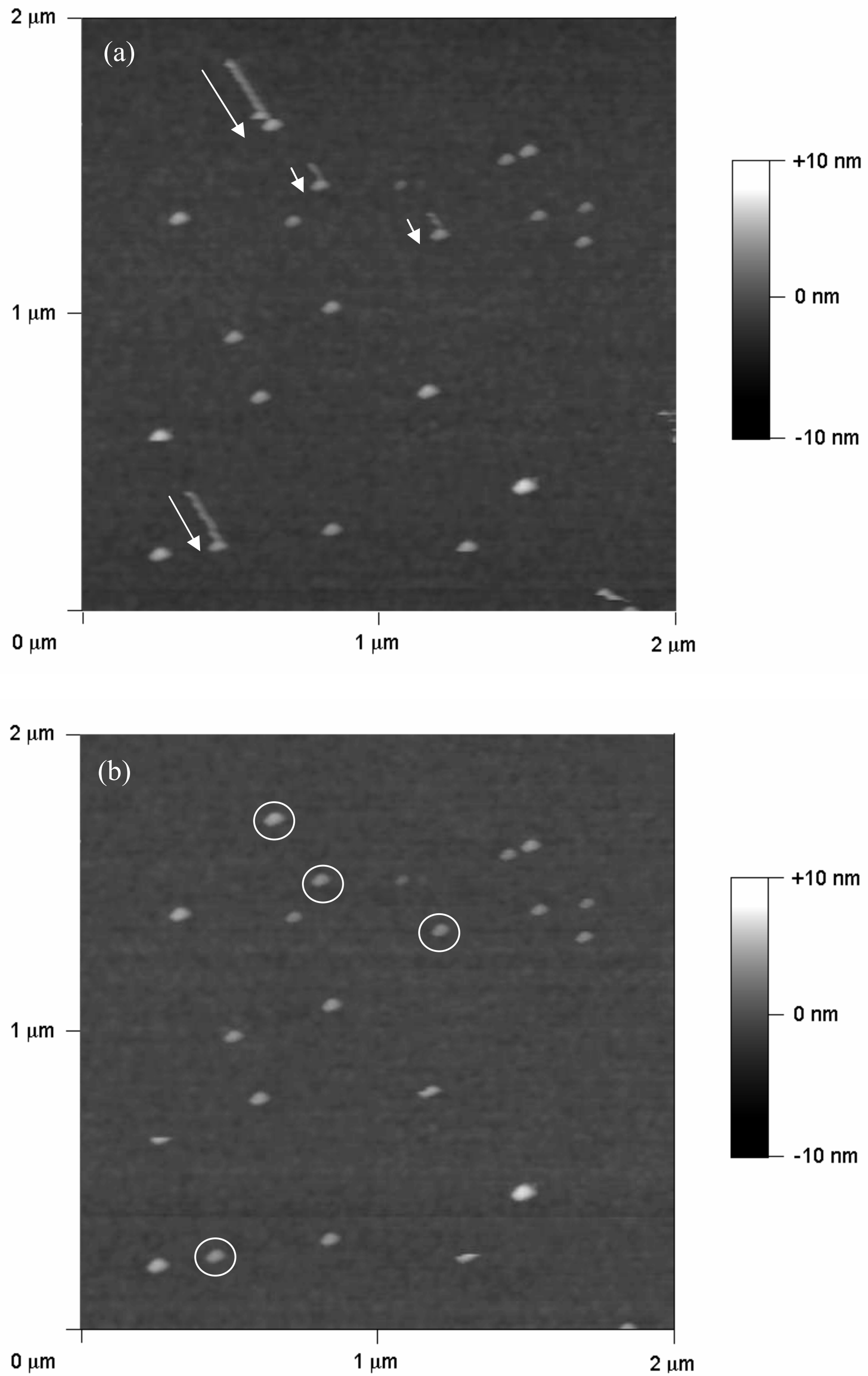

Figure 4.10: Nanocrystals may be pushed along a Si surface (a). After manipulation, nanocrystals assume their new positions (b). Arrows indicate the directions of the moving nanocrystals and circles show the new positions. These results suggest controllable nanomanipulation will be possible using AFM.

5. In-situ Characterization of Nanocrystals at Elevated Temperature

5.1 Introduction

Of particular importance to understanding nucleation and growth phenomena in nanocrystal systems is knowledge of whether nanocrystals are solid or liquid during growth. A variety of studies have been performed to determine the melting points of nanocrystals as a function of their size and surface termination. For the case of free standing nanocrystals and nanowires, melting point depression has been commonly observed.[115-119] However, when nanocrystals are embedded in a matrix, both melting point depression and elevation have been reported.[120-122] In the present case, nanocrystals nucleate and grow in an oxide matrix just below the bulk Ge melting point of 938 °C, and thus their phase during the growth process is not immediately evident. To further understand the melting behavior of embedded Ge nanocrystals, *in-situ* electron diffraction (performed by Qing Xu) and Raman spectroscopy (performed by the author) were implemented. In addition, growth experiments were carried out at a variety of times and temperatures and *ex-situ* Raman spectroscopy was performed to correlate the observed compressive stresses to the nanocrystal phase during growth. Future experiments will compare the melting behaviors of liberated nanocrystals to those of embedded nanocrystals. In addition to phase determination, the temperature dependence of first order Raman active phonon modes provides practical information regarding anharmonic crystalline properties and the influence of surface scattering on phonon relaxation times.

5.2 In-situ Raman Spectroscopy

5.2.1 Experimental

In-situ Raman spectra were obtained between room temperature and 850 °C using the Raman configuration described in Chapter 3 with a few slight modifications. Samples were heated on an alumel filament under flowing dry nitrogen. Due to significant blackbody radiation at higher temperatures, it was not possible to use the 488 nm line of the Ar ion laser. To avoid this background, the 457.9 nm emission line was instead used for excitation. To maximize the incident laser power, and hence the Raman signal, no narrow bandpass filter was used. As a result, it was necessary to manually remove laser lines from some spectra. Above 850 °C, thermal stability was lost and it was not possible to obtain reproducible results. In the future, additional experiments with a more stable heater will be performed under vacuum to obtain higher temperature data.

The measurement temperature was determined by tracking the position of the first order Si Raman line. The temperature dependence of this phonon has been well characterized[123,124] and thus provides an internal temperature calibration for these experiments. Therefore, the spectrometer was adjusted to simultaneously capture the Raman lines from both the Si substrate and the Ge nanocrystals. The temperature dependence of Raman spectra, along with the specific Si temperature calibration that was used, will be discussed in detail in the following section.

5.2.2 Anharmonic Effects on First Order Raman Spectra

The temperature dependence of Raman spectra arises from anharmonic contributions to the bonding potential. The standard harmonic oscillator model provides a good approximation for calculating many properties of crystalline materials. However,

at finite temperature this model is insufficient to predict many real phenomena such as phonon-phonon coupling, thermal expansion, and relaxation to equilibrium phonon occupations. Therefore, it is necessary to apply perturbation theory to the harmonic oscillator approximation in order to accurately describe the effects of temperature on Raman spectra.

With increasing temperature, Raman spectra are altered in three ways:[123]

i) The intensity of the Stokes line decreases whereas the intensity of the anti-Stokes line increases

ii) The Raman line position red shifts

iii) The natural linewidth of the Raman peak increases.

The first observation may be easily described by analyzing the temperature dependent phonon occupation number. However, the second two effects can only be described using perturbation theory. Each of these effects is described in detail below, and Appendix B provides a more in-depth mathematical description of the theoretical models. Figure 5.1 shows the experimentally obtained first order Si Raman signal at various temperatures. The three temperature effects described above are all observed.

The intensity of Stokes scattering decreases with increasing temperature. In the present experiments the anti-Stokes line is not monitored because of its relatively weak intensity. However, to qualitatively show the origin of this intensity reduction, the effect of temperature on the ratio of the anti-Stokes to Stokes intensity is presented. Upon heating, the intensity of the anti-Stokes line increases because thermally induced lattice vibrations enhance the probability of phonon absorption. Consequently, the intensity of the Stokes line decreases with increasing temperature. The intensity of anti-Stokes

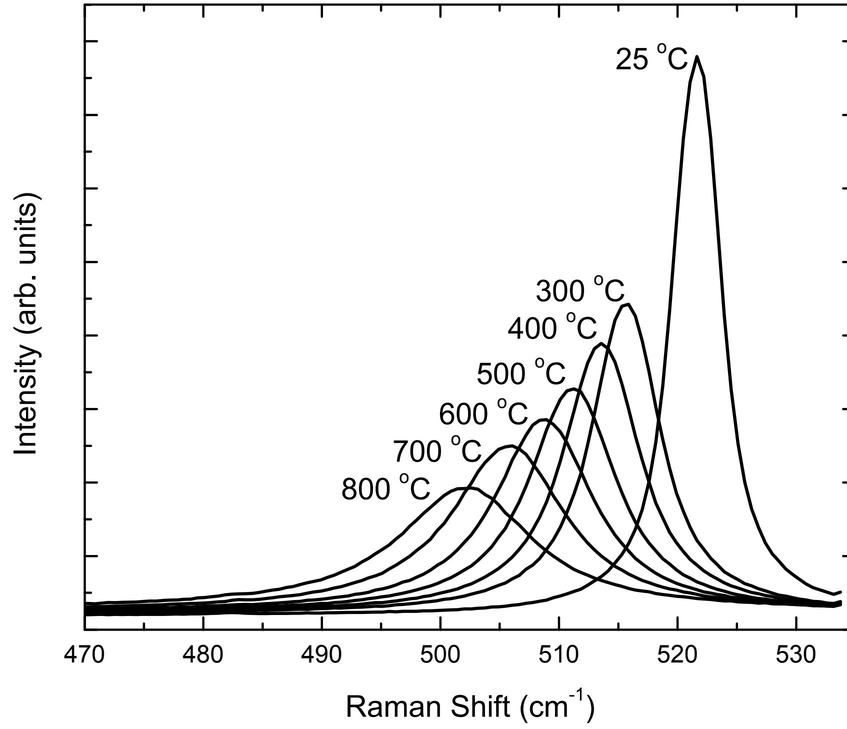

Figure 5.1: Experimentally obtained first order Si Raman peaks at 25 °C, 300 °C, 400 °C, 500 °C, 600 °C, 700 °C, and 800 °C (right to left). With increasing temperature, the Raman line red shifts, broadens, and loses intensity.

scattering is proportional to the zone center phonon occupation number, N_o and the intensity of Stokes scattering is proportional to $N_o + 1$, where the 1 is the result of zero-point motion at absolute zero. The ratio of the anti-Stokes line, $I_{a\text{-}S}$ to the intensity of the Stokes line, I_S, is:[125]

$$\frac{I_{a-S}}{I_S} = \frac{N_o}{(N_o + 1)} \tag{5.1}$$

The thermal occupation of the zone center optical phonon mode is simply given by a Bose-Einstein distribution function:[97]

$$N_o = \frac{1}{e^{\hbar\omega_o / k_B T} - 1} \tag{5.2}$$

Therefore, the intensity ratio as a function of temperature becomes:

$$\frac{I_{a-S}}{I_S} = \exp\left(-\frac{\hbar\omega_o}{kT}\right) \tag{5.3}$$

It should be noted that this model assumes the absorption coefficients and Raman efficiencies are equivalent at the Stokes and anti-Stokes wavelengths.[124] Since Equation 5.3 was not directly used to determine the sample temperature, a correction for this approximation is not required. Equation 5.3, however, serves to qualitatively describe the behavior of the Raman intensities with temperature and illustrates the increasing difficulty of obtaining Raman spectra from the Stokes line at elevated temperatures. It should also be noted that at elevated temperature mechanical stability of the sample due to thermal expansion of the heating element, and thus focusing within the Raman system, become more difficult. Thus, the absolute intensities of Raman spectra are not necessarily quantitatively accurate.

The red shifting and line broadening of Raman spectra with increasing temperature may be attributed to thermal expansion and multi-phonon coupling, both of which are anharmonic effects. Near the equilibrium bond length the potential is close to parabolic, which leads to the standard harmonic oscillator approximation. However, as temperature increases from the ideal case at absolute zero, anharmonic effects begin to play an increasingly important role. At room temperature, anharmonic contributions to the Raman line position and width, and to less extent the bond length, are already impacted by anharmonic effects.

Lattice expansion and phonon-phonon coupling result in broadened and shifted first order optical phonon modes and the temperature dependence of the optical phonon mode gives a significant amount of information about phonon dynamics. The temperature dependent Raman frequency, $\omega(T)$ may be written as:

$$\omega(T) = \omega_o + \Delta_1(T) + \Delta_2(T) \tag{5.4}$$

where ω_o is the Raman frequency in the limit of zero absolute temperature, $\Delta_1(T)$ is the contribution to the frequency shift due to thermal expansion, and $\Delta_2(T)$ is the contribution to the frequency shift due to phonon-phonon coupling. The thermal expansion component may be expressed as:[123]

$$\Delta_1(T) = \omega_o \left[\exp\left\{ -3\gamma \int_0^T \alpha_L(T)dT \right\} - 1 \right] \tag{5.5}$$

where $\alpha_L(T)$ is the linear coefficient of thermal expansion and γ is the mode-Grüneisen parameter.

At moderate temperatures, $\Delta_2(T)$ may accurately describe experimental data when only three phonon coupling is considered. However, at higher temperatures, such as those considered here, it is necessary to consider four phonon coupling, corresponding to the quartic anharmonic terms in the bonding potential. The frequency shift, considering both three and four phonon process is given by:[124]

$$\Delta_2(T) = A\left(1 + \frac{2}{e^{\hbar\omega_0/2k_BT}}\right) + B\left[1 + \frac{3}{e^{\hbar\omega_0/3k_BT} - 1} + \frac{3}{\left(e^{\hbar\omega_0/3k_BT} - 1\right)^2}\right] \tag{5.6}$$

where A and B are constants. The first (second) term in Equation 5.6 gives the coupling of the excited optical phonon to two (three) additional phonons.

Likewise, line broadening may be expressed as a function of temperature in the following manner:[124]

$$\Gamma(T) = C\left(1 + \frac{2}{e^{\hbar\omega_0/2k_BT}}\right) + D\left[1 + \frac{3}{e^{\hbar\omega_0/3k_BT} - 1} + \frac{3}{\left(e^{\hbar\omega_0/3k_BT} - 1\right)^2}\right] \tag{5.8}$$

where C and D are constants and the first and second terms have the same meaning as

those in Equation 5.6. It is no coincidence that the expressions for line shift and broadening are very similar. The contribution of phonon-phonon coupling to the line shift is the real part of the phonon self-energy, whereas the corresponding contribution to line broadening is the imaginary part of the phonon self-energy. The two are directly related through a Kramers-Kronig relation.[126]

When considering phonon-phonon coupling, it is useful to recognize that coupling is a means of describing phonon decay processes. That is, three phonon coupling involves the decay of the optically excited phonon to two phonons and four phonon coupling is decay to three phonons. Therefore, the linewidth is proportional to the decay rate of the occupation number of the Raman active phonon. This, in turn, is inversely proportional to the phonon relaxation time, τ, so[127]

$$\Gamma(T) \propto \frac{1}{\tau} \tag{5.9}$$

Therefore, comparison of the nanocrystalline Ge Raman line broadening to the bulk Ge line broadening with temperature provides direct information about the confined phonon lifetime. This may provide useful information regarding phonon scattering from the surface of nanocrystals and will be examined further in Chapter 5.2.2.

The peak position and width for the Si Raman line as a function of temperature have been determined over a wide temperature range. Figure 5.2(a) shows the line position as a function of temperature as determined by Balkanski *et al.*[124] using the parameters 528 cm^{-1}, -2.96 cm^{-1}, and 0.174 cm^{-1} for ω_o, A, and B, respectively. The dashed line in Figure 5.2(a) shows the result when four phonon coupling is not considered and the fitting parameters are optimized using 529 cm^{-1} and -4.24 cm^{-1} for ω_o and A, respectively. The four phonon model accurately fits the experimental observations

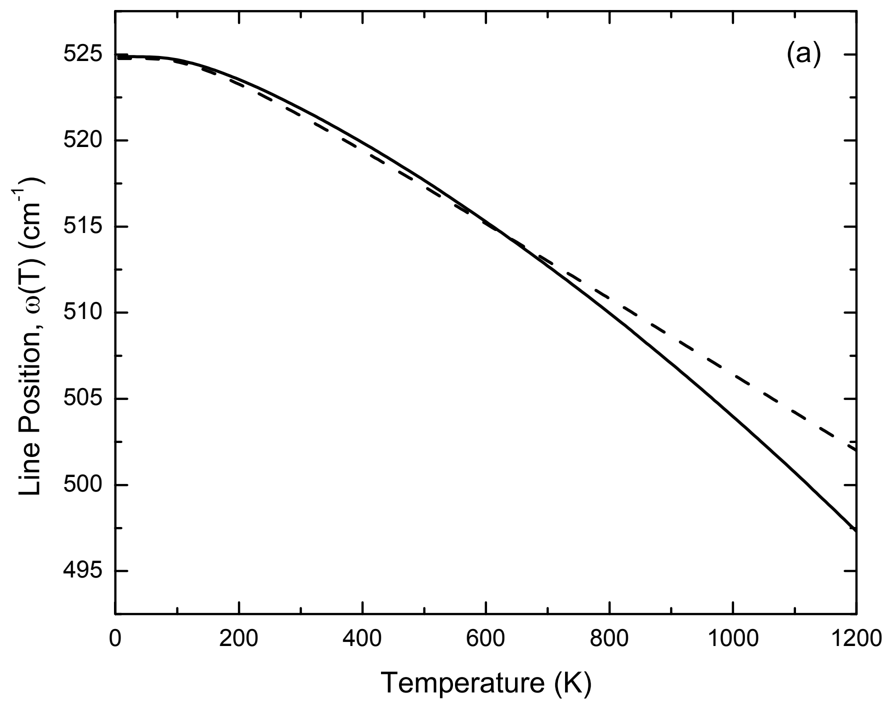

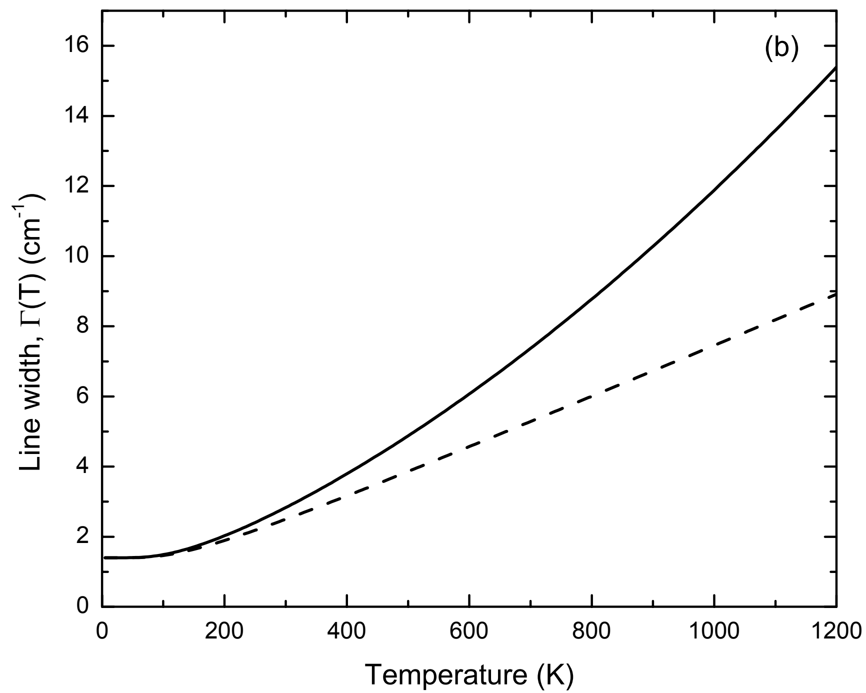

Figure 5.2: Calculated position (a) and width (b) of the first order Si Raman line. Solid lines give results of calculations using three and four phonon coupling and dashed lines give results using only three phonon coupling. Solid lines provide a good fit to the data reported by Balkanski *et al.* (not shown).[124]

of Balkanski and co-workers, but the dashed line deviates significantly from their experimental data (not shown) at higher temperatures.

In this model, the contribution due to thermal expansion is not considered by the authors because the experimental data could be fit by appropriately adjusting the parameters *A* and *B*.[128] Adding the contribution due to thermal expansion does not significantly improve the fit but does alter the fitting parameters and adds complexity to the model.

Figure 5.2(b) shows the temperature dependence of the line width. Here, the dashed line, which shows the result when four phonon coupling is neglected, deviates significantly from the fit using Equation 5.8. The fitting parameters for the line broadening are 1.295 cm^{-1}, and 0.105 cm^{-1} for *C* and *D*, respectively. When four phonon coupling is not considered, the fitting parameter is 1.40 cm^{-1} for *C*. Temperature measurements in the current study were made according to Equations 5.4 and 5.6 using the fitting parameters of Balkanski *et al*. considering four phonon coupling, as shown by the solid line in Figure 5.2(a).

5.2.3 In-situ Raman Spectroscopy Results

Figure 5.3 shows Ge Raman spectra obtained at temperatures ranging from 700 °C to 850 °C. As expected, the Raman signal decreases in intensity, shifts to lower energy, and broadens with increasing temperature. Though the intensity of the signal decreases, this is a natural consequence of the predictions of Equation 5.3. The intensity decrease does not imply melting of nanocrystals. From this figure, it is clear that Ge remains in nanocrystalline form at all measurement temperatures. *In-situ* observation of melting was not possible due to high temperature limitations of the heating system.

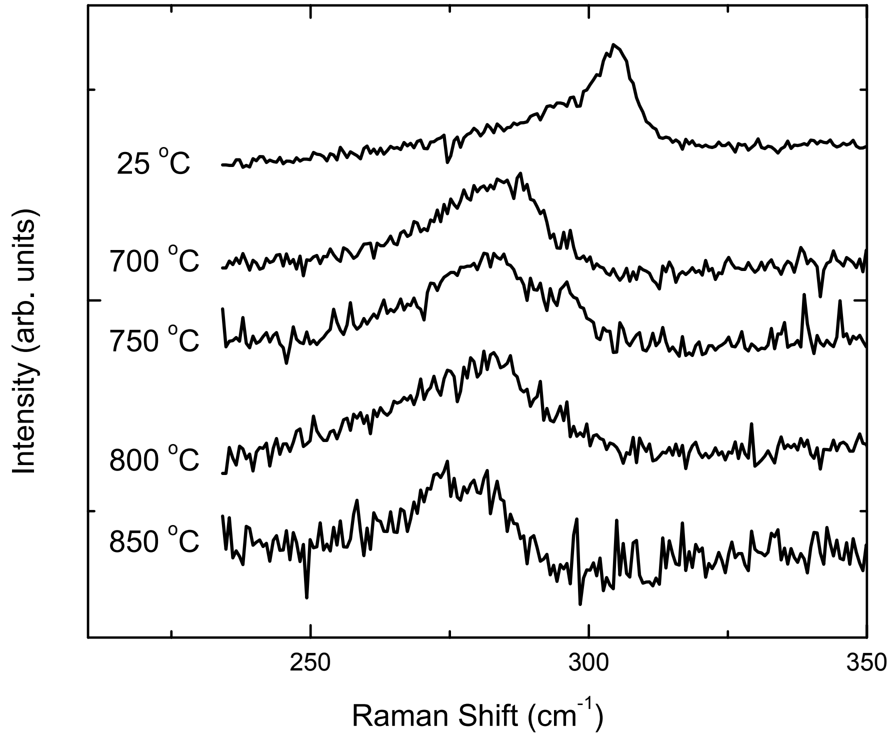

Figure 5.3: Raman spectra of nanocrystalline Ge at room temperature and between 700 °C and 850 °C.

Nevertheless, these results indicate that significant melting point depression, which has been observed in free standing nanocrystals, does not occur for the case of embedded Ge nanocrystals in amorphous silica.

The FWHM of the Raman peaks of bulk ^{nat}Ge[129] and ^{74}Ge nanocrystals are shown in Figure 5.4 as a function of temperature (no data are currently available for bulk ^{74}Ge). The FWHM is significantly larger for Ge nanocrystals as a result of phonon confinement effects described in Chapter 3. This size effect is not expected to be temperature dependent.[130] Therefore, it is possible to define an additional broadening term, $\Gamma_{confine}$, summed in Equation 5.8 to be the temperature independent, but size dependent, broadening arising from phonon confinement.[130] Experimental data from bulk and nanocrystalline Ge are fit using the factors C and D from Equation 5.8, along with $\Gamma_{confine}$

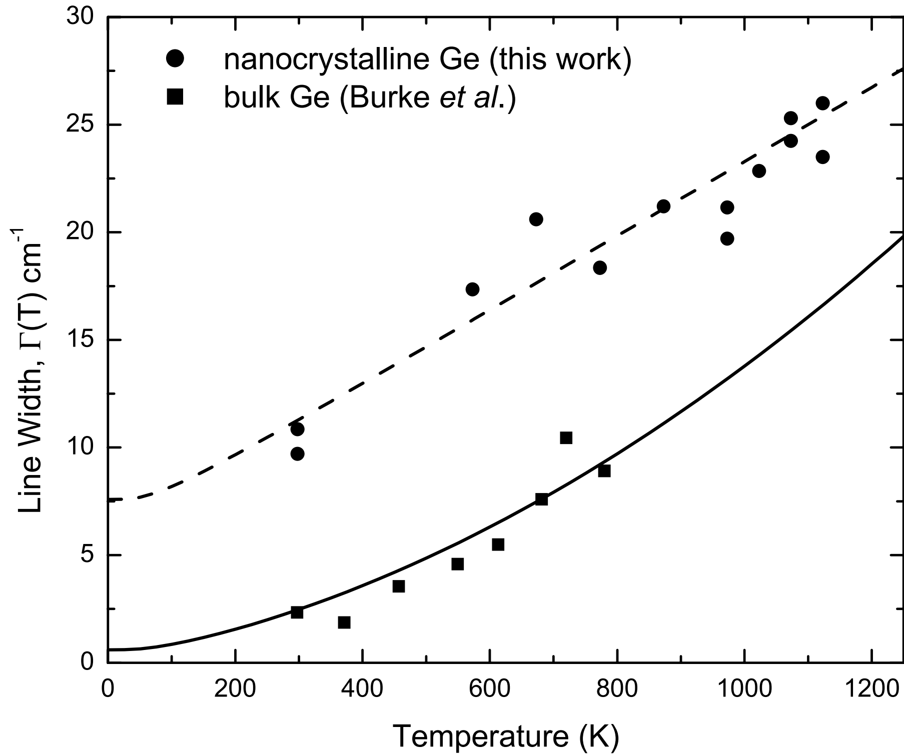

Figure 5.4: The Raman line width as a function of temperature for nanocrystalline ^{74}Ge (●) and bulk ^{nat}Ge (■). Experimental data are fit with Equation 5.8 for nanocrystalline ^{74}Ge (dashed line) and bulk ^{nat}Ge (solid line). Fitting parameters are given in Table 5.1.[129]

for the case of nanocrystals. Table 5.1 gives the relevant constants and fitting parameters used for these calculations.

For the case of bulk Ge, a good fit to the experimental data may only be obtained by accounting for both three and four phonon coupling through the constants C and D.[129] As evidenced by the relative values of these constants, the three phonon process is

Table 5.1: Constants and fitting parameters used for calculation of the FWHM of ^{74}Ge nanocrystals and bulk ^{nat}Ge as a function of temperature.

	^{nat}Ge bulk (cm^{-1})	^{74}Ge nanocrystals (cm^{-1})
C	0.54	1.69
D	0.06	0
Γ(T=0K)	0.6	7.59
$\Gamma_{confine}$	N/A	5.9
ω_o	306	298

dominant, as expected. For the case of nanocrystalline Ge, the contribution from four phonon processes seems to be negligible (D = 0). The value $\Gamma_{confine}$, which gives the confinement-induced broadening, is reasonable and describes well the size-dependent line broadening observed at room temperature. Mishra & Jain[130] have analyzed the size dependence and temperature dependence of the FWHM of the Raman line for nanocrystalline Si. They found that anharmonic effects are larger in nanocrystalline Si than in bulk Si and become more pronounced with decreasing crystal size. The results presented here support that finding, as evidenced by the enhancement of three phonon coupling in nanocrystals. These preliminary results suggest that phonon lifetimes in nanocrystals are suppressed according to Equation 5.9, likely due to phonon scattering at the nanocrystal/matrix interface. Additional experiments will be required to conclusively determine the effect of nanocrystal size on phonon lifetimes. In particular, experiments should be performed with isotopically enriched bulk samples, the temperature range should be extended below room temperature, and a much higher data point density is required. Furthermore, these experiments should be performed on samples with various nanocrystal size distributions. Nevertheless, these initial results demonstrate that significant information, beyond the phase of Ge, may be gleaned from variable temperature Raman spectroscopy experiments.

5.3 In-situ Transmission Electron Microscopy

5.3.1 Experimental

Elevated temperature electron diffraction patterns were obtained by Qing Xu, a graduate student in the group of Professor E.E. Haller, at elevated temperatures using a JEOL 200CX analytical electron microscope at the National Center for Electron

Microscopy (NCEM), with 200 keV accelerating voltage for all experiments. Heating was performed using a Gatan single tilt 628Ta heating stage. This stage is rated to go up to 1300 °C with ± 60 °C accuracy, and the temperature may be continuously monitored using a thermocouple. Nanocrystal samples were thinned by dimpling and ion milling to obtain electron transparency. Embedded nanocrystal samples were heated between room temperature and 1100 °C until the electron diffraction pattern was no longer observed. Slow cooling was subsequently performed to observe the reemergence of electron diffraction patterns upon solidification of nanocrystals.

As materials are heated, thermal atom vibrations around their equilibrium positions leads to a decrease in the diffraction intensity. However, the peak width is preserved at all temperatures below the melting point. This change of the diffraction intensity with temperature, known as the Debye-Waller effect, may be described by the following equation:[98]

$$I = I_o \exp\left(-\frac{k_B T G^2}{M\omega^2}\right) \tag{5.10}$$

The Debye-Waller factor, given by the exponential, contains the oscillator frequency, ω, its mass, M, and the reciprocal lattice vector, G, for the diffraction peak under consideration. Therefore, the intensities of higher order diffraction peaks should decrease more rapidly than lower order peaks.

5.3.2 In-situ Electron Diffraction Results

Figure 5.5 shows a plot of the normalized (111) diffraction peak intensity as a function of temperature during heating and cooling. The intensity has been normalized to the intensity of the (111) peak at 731 °C for clarity, and solid lines are shown to guide the eye. During heating to a temperature of approximately 1050 °C, the diffraction intensity

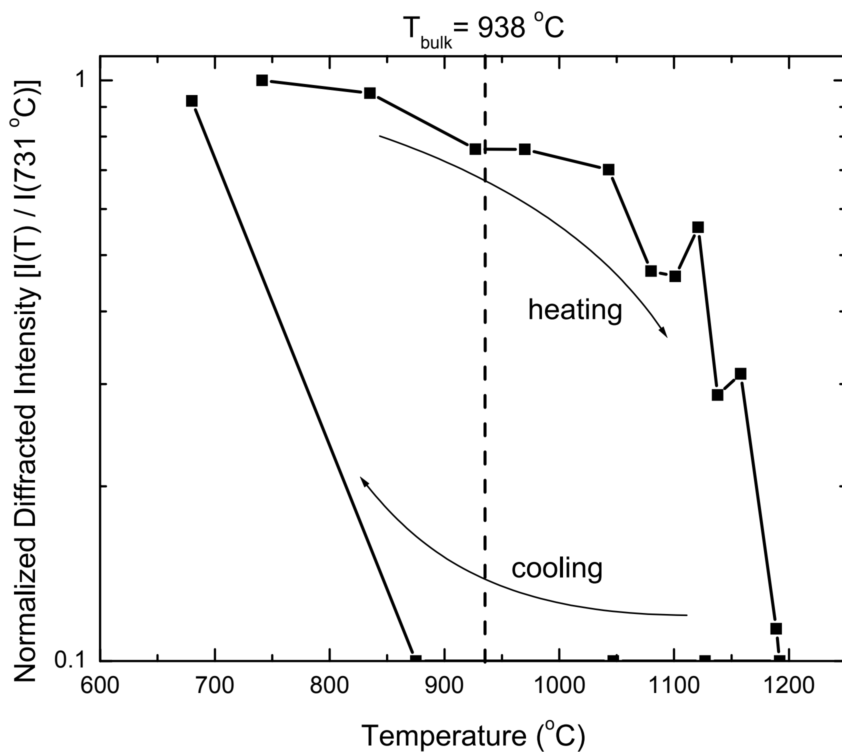

Figure 5.5: Normalized (111) Ge diffraction intensity as a function of temperature. All intensities have been normalized to the intensity of the original peak at 731 °C. The vertical dashed line indicates the bulk Ge melting point. Significant melting point hysteresis is observed around this temperature. Solid lines are shown as guides only.

gradually decreases. This is a consequence of thermally enhanced atomic vibrations, as discussed in the previous section. However, above approximately 1100 °C, the intensity decreases due to the onset of melting. At 1189 °C, the intensity of the diffracted peak is on the order of background noise and nanocrystals are fully melted. This transition from nanocrystalline Ge to liquid Ge is not entirely sharp. This is likely a result of the wide nanocrystal size distribution and is an indication that the Ge melting point is size dependent.

During cooling, the diffraction peak remains absent to 875 °C. Between 875 °C and 680 °C the peak reappears, indicating that Ge solidifies. However, the data point density is not high enough to observe the transition from liquid Ge droplets to nanocrystalline Ge. Further *in-situ* electron diffraction experiments will be performed to

more precisely observe the solidification process.

The bulk melting point of Ge is 938 °C. The results presented here indicate that embedded Ge nanocrystals can be superheated and embedded liquid Ge droplets can be undercooled. Thus, a wide melting point hysteresis exists around this bulk melting point which is beyond the maximum temperature measurement error (±60 °C for each point). A similar phenomenon has been observed in other nanocrystal systems and will be discussed in Chapter 5.5.[131] Since these experiments were performed subsequent to growth, it remains unclear whether nanocrystals are solid or liquid during the initial growth process. It is expected the magnitude of superheating is size dependent. If this is the case, melting point enhancements should be the largest for the smallest particles.

5.4 Growth Experiments

Two systematic growth experiments were performed to determine the phase of nanocrystals during the initial growth process. In the first experiment, implanted samples were annealed for one hour each at temperatures between 800 °C and 900 °C. In the second experiment, implanted samples were annealed at 900 °C for times ranging from 15 minutes to 24 hours. Raman spectroscopy was used to determine the compressive stress present in all samples after quenching from the annealing temperature. Additional stress measurements will be discussed in detail in Chapter 6 and the method for determining stress from the Raman line position is given in Appendix C.

It has been hypothesized that Ge is liquid during growth and compressive stresses originate from the 6% volume expansion[93] of Ge upon solidification when samples are cooled to room temperature.[132] If this is the origin of stress, the measured pressure should be independent of nanocrystal size since the 6% lattice expansion would result in

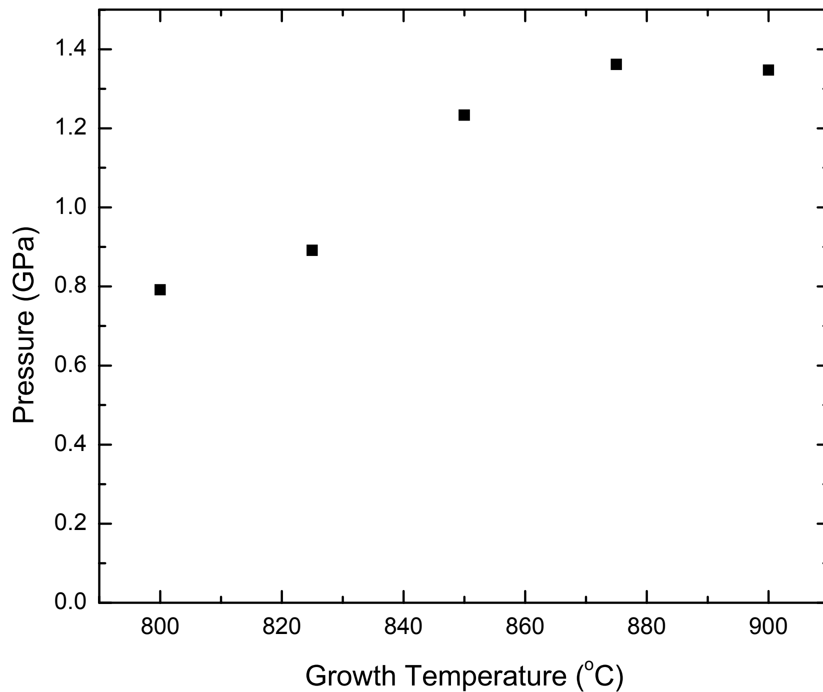

Figure 5.6: Pressure exerted on nanocrystals as a function of the growth temperature. All samples were annealed for 1 hour.

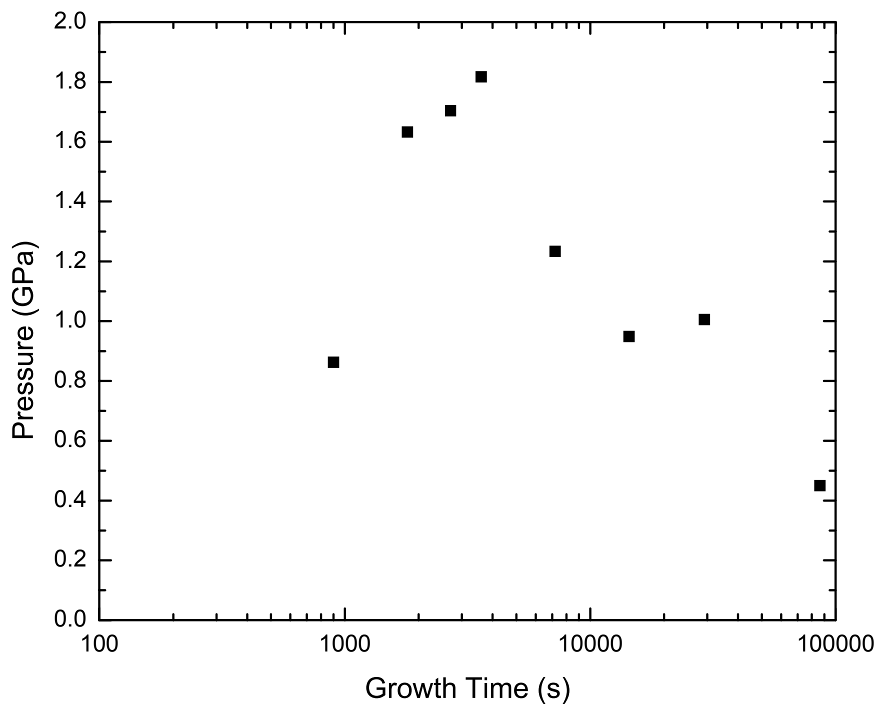

Figure 5.7: Pressure exerted on nanocrystals as a function of the growth time. All samples were annealed at 900 °C. The sample grown at 900 °C for one hour shown in this figure is not the same sample shown in Figure 5.6.

constant strain for all sizes. Furthermore, according to this mechanism the stress is generated during quenching at the conclusion of annealing, so there is minimal transient time for the stress to be annealed away. Figure 5.6 shows the pressure present in as-grown samples annealed for 1 hour as a function of the annealing temperature. The pressure increases smoothly with growth temperature. However, smaller nanocrystals are formed at lower growth temperatures, as shown by TEM in Chapter 3.

Due to the Gibbs-Thomson effect, which will be discussed in detail in Chapter 6 and Appendix D, the smallest nanocrystals should experience greater stresses than larger ones. These observations suggest that solidification is not the source of stress and that the stress generation mechanism is linked to the dynamics of the growth process itself.

Figure 5.7 shows the compressive stress as a function of the annealing time for samples annealed at 900 °C. Initially stress increases with growth time. Beyond one hour, however, stress decreases with annealing time. As will be shown in Chapter 6, the nanocrystal coarsening rate is very slow. Therefore, the nanocrystal size distribution has likely stabilized at the conclusion of one hour of annealing. It appears that stress accumulates during the initial growth of nanocrystals and is relieved through further annealing. Once again, these observation are not consistent with the solidification model for stress generation and strongly suggest that nanocrystals are solid during growth. Specific mechanisms for the generation and relief of compressive stress will be presented in Chapter 6.

5.5 Theory of the Melting Behaviors of Nanocrystals

Numerous experiments have shown that the melting points of free standing nanocrystals, both metal and semiconductor, are significantly reduced from their bulk

values.[115-119] Embedded nanocrystals, on the other hand, may experience either melting point depression or enhancement, depending on the matrix in which they reside.[120-122] Melting point hysteresis extending above and below the bulk melting temperature has also been observed.[131] Because a significant fraction of the atoms comprising a nanocrystal are at the surface, it is not surprising that the local environment of surface atoms plays a crucial role in the melting behavior.

The theory of melting point depression in metal nanocrystals has been well developed and relies on classical thermodynamic arguments. However, the specific mechanism of melting has not been established conclusively to date. One commonly accepted model, which matches a wide range of experimental observations, is called the homogeneous melting and growth (HMG) model.[115] This model describes equilibrium between solid particles, liquid particles, and vapor. Melting occurs when the chemical potential of the liquid is less than that of the solid. For the case of a small particle, the chemical potential, μ_i, is size dependent and is increased by the surface tension of the particle, γ_i, according to:

$$\mu_i(r) = \mu_i^{bulk} + \frac{2\gamma_i}{\rho_i r} \tag{5.11}$$

Where ρ_i is the density and r is the particle radius. Buffat & Borel have shown that the size dependent melting point depression for nanoparticles, ΔT, resulting from this change in the chemical potential is:[115]

$$\Delta T = T_m^{bulk} - T_m(r) = \frac{2T_m^{bulk}}{H_m^{bulk}\rho_s r}\left[\gamma_s - \gamma_l\left(\frac{\rho_s}{\rho_l}\right)^{2/3}\right] \tag{5.12}$$

Where T_m^{bulk} and $T_m(r)$ are the bulk and size-dependent particle melting temperatures,

respectively, and H_m^{bulk} is the bulk latent heat of fusion.

A number of alternate models have also been proposed to describe the size dependent melting of nanocrystals.[133-135] However, for the case of elemental semiconductor nanocrystals, no definitive theory is currently accepted. Therefore, the specifics of these theories will not be presented here. What is common to these models, however, is the importance of the surface atoms to the melting point. The surface atoms of free standing nanocrystals have a lower coordination number than the interior atoms. As a consequence, they are less stable, particularly at elevated temperatures. Therefore, as nanocrystal sizes decrease and the surface atom fraction increases, the melting point decreases.

The situation may be considerably different when nanocrystals are embedded in a matrix. In this case, surface atoms may actually be more stable than the interior atoms due to chemical interface interactions. In essence, the surface atoms are "pinned" and their vibrational amplitudes are significantly reduced. Since melting initiates on the surface, melting point enhancements occur.

In the present case, significant hysteresis of the melting point is observed for embedded Ge nanocrystals. Such an effect has been previously observed, though the mechanism for its occurrence remains a mystery. Here, a mechanism for the specific case of embedded Ge nanocrystals is proposed. It should be emphasized, however, that this proposed mechanism is, at this time, merely a hypothesis that may describe the observed phenomena.

Significant melting point enhancements are observed upon heating from room temperature. This is likely the result of suppressed surface vibrations due to interactions

with the SiO_2 matrix. As shown in Figure 4.5, low energy amorphous-like surface modes are observed from Raman spectra of free-standing Ge nanocrystals. However, these modes do not appear in Raman spectra from embedded nanocrystals. These observations support the present interpretation that the silica suppresses surface atom vibrations, leading to melting point enhancements.

Liquid Ge has a 6% smaller volume than solid Ge.[93] After considerable superheating, the thermal energy is sufficiently large to overcome the energetic barrier for melting, which includes the energy to create additional interfaces arising from the volume contraction of Ge. As a result of the Ge volume reduction, interactions between the nanocrystal and the matrix are no longer as strong because not all of the Ge surface is in contact with silica. In this way, the nanocrystals partially show properties of free-standing nanocrystals and the melting point is reduced below that of the bulk material.

5.6 Summary of Melting Point Observations

In-situ Raman spectroscopy demonstrates conclusively that Ge nanocrystals remain crystalline to at least 850 °C. Construction of a vacuum cell with a stable heating unit will allow for characterization of nanocrystals at even higher temperatures. Raman spectroscopic observation of the growth process will be attempted with such an apparatus.

In-situ electron diffraction patterns provide significant insight into the melting behaviors of Ge nanocrystals. A wide hysteresis of the melting point, consisting of significant superheating of embedded nanocrystals during heating and undercooling of liquid droplets during cooling, is observed. A mechanism is proposed to describe these phenomena, though it has not yet been proven experimentally or theoretically.

Growth experiments show, with reasonable certainty, that nanocrystals are solid during growth. With increasing growth temperature, the pressure exerted on the nanocrystals increases. This observation is contrary to the size-dependent pressure effect arising from surface tension and the size-independent pressure that would be observed for the case of solidification stress. At constant temperature, stress increases for short growth times but decreases for growth times above one hour. These observations support a stress generation mechanism that is coupled to the growth mechanism, and not one that is based on solidification during quenching.

The generation and relief of stress will be discussed in greater detail in Chapter 6. Post-growth thermal annealing experiments are discussed that occur at temperatures below the initial growth temperature of 900 °C. The experiments described in this chapter (Chapter 5) show conclusively that Ge is solid and crystalline during these post-growth annealing experiments. Though all evidence currently suggests nanocrystals are solid during growth, this has not yet been proven directly. Additional Raman spectroscopy and electron diffraction experiments are expected to definitively answer this remaining question.

6. Characterization and Control of Nanocrystal Stresses

6.1 Introduction

Control of stresses in nanocrystals may provide a powerful means of tuning the nanocrystal bandgap, engineering the size distribution, and possibly, achieving ordered structures. Stress generation and relief have been studied extensively for the case of thin film growth processes.[136] In particular, heteroepitaxial thin film growth can lead to large stresses which have been exploited for myriad applications such as strained quantum well structures and ultrafast SiGe devices.[137] Stress arising from heteroepitaxial growth has also been used for self-assembly of ordered quantum dot arrays[69-71] and has provided a means to obtain narrow island size distributions.[26,72-74] However, understanding of stress mechanisms in three-dimensions and at the nanoscale remains relatively limited. Since significant hydrostatic pressures are observed in as-grown nanocrystals, the present system affords an opportunity to further the theory of stress generation and relief during three dimensional nucleation and growth at the nanoscale.

Compressive stress in nanocrystals has occasionally been observed,[83,100,105,132,138] but no systematic study has been performed to date and no physical model has been developed to describe its behavior. Two separate explanations for the observed stress have, however, been proposed. Due to the 6% volume expansion of Ge upon solidification,[93] it has been suggested that Ge nucleates and grows in the liquid phase, creating a void within the oxide equivalent to the Ge droplet size. Upon cooling from the growth temperature, nanocrystals rapidly solidify and the void within the matrix is unable to accommodate the larger nanocrystal volume.[132] As was shown in the previous chapter, significant evidence exists suggesting nanocrystals are solid at the growth temperature.

However, solidification stress can not yet be entirely discounted. Future experiments will be required to conclusively determine whether nanocrystals are solid or liquid at the growth temperature. Nevertheless, an alternate mechanism for stress generation will be proposed that is based on the dynamics of solid phase growth.

Another explanation is that stress arises from the mismatch between nearest neighbor distances in amorphous SiO_2 and Ge, which are 0.16 nm and 0.24 nm, respectively.[100,139,140] The results presented here do not support this explanation. It is shown that stress may be systematically relieved through post-growth annealing and that the degree of stress relief depends strongly on the time and temperature. If mismatch were the cause of the observed stress, it is expected that stress would either be unaffected by post-annealing or it would be reduced rapidly due to surface reconstructions and depend very little on annealing time. It should be noted that the difference between the thermal expansion coefficients of the matrix and Ge has also been considered as the source of compressive stress.[132] However, the thermal expansion coefficient of SiO_2 ($\alpha_{SiO_2} = 5.5 \times 10^{-7}$ K^{-1}) is less than that of Ge ($\alpha_{Ge} = 6.5 \times 10^{-6}$ K^{-1}) and rapid cooling from the annealing temperature would yield negative pressures on nanocrystals as they contract away from the matrix.

A variety of methods exist for determining the stress state of a material. In particular, x-ray and electron diffraction provide direct measurements of the lattice parameter, thereby giving the most fundamental measures of stress. In the present case, however, it has not yet been possible to obtain x-ray diffraction patterns due to the diminutive total volume of crystalline Ge. Electron diffraction patterns have been obtained, but they lack the resolution to discern small changes of the lattice parameter

with compression. Though a less direct measure of stress, Raman spectroscopy provides both the sensitivity and resolution required to determine pressures on embedded nanocrystals. Here, this method for the precise measurement of stress is presented and a mechanism for stress generation during the growth of solid nanocrystals is proposed. Characterization and control of stress is achieved through a series of post-annealing experiments and a theoretical model for its relief as a function of annealing time and temperature is developed following the derivation of D.O. Yi and D.C. Chrzan.[141] This model consists of two parts: first, the elastic problem for a strained nanocrystal in matrix void is solved to provide the driving force for stress relaxation, and second, a steady state diffusion problem, assuming thermodynamic equilibrium at the nanocrystal/matrix interface is solved to describe the dynamics of stress relaxation.

6.2 Experimental Techniques

Compressively stressed nanocrystals were formed using the standard synthesis procedure outlined in Chapter 2. Initial nanocrystal growth was performed at 900 °C for 1 hour and samples were rapidly quenched from the annealing temperature under running cold water. Post-annealing was performed to relieve and characterize the compressive stress. Again, standard sample preparation procedures were followed and post-annealing was conducted at 600 °C, 700 °C, and 800 °C for times ranging between 30 minutes and 48 hours. Post-annealing was terminated by quenching under running water. The stresses exerted on nanocrystals by the SiO_2 matrix were determined via Raman spectroscopy. Spectra were smoothed using a cubic spline with the csaps function in MATLAB and the peak position was determined by taking the zero crossing of the derivative of the smoothing function.

6.3 Pressure Dependent Raman Spectroscopy

The zone center optical phonon mode ($\Gamma_{25'}$) of Ge is triply degenerate as a result of the three-fold symmetry of the diamond cubic structure.[97] Application of tensile stress, however, breaks the cubic symmetry, thereby splitting the degenerate bands. For example, application of uniaxial stress results in phonon energy splitting to doubly degenerate modes in directions perpendicular to the stress and a singlet in the direction parallel to the stress. The energies of all modes are also increased due to the hydrostatic component of the stress. Therefore, uniaxial stress manifests itself as peak broadening (the resolution of the Raman system is insufficient to observe split peaks individually) as well as shifting to higher energies. Hydrostatic pressure is isotropic and the zone center triplet is retained. Therefore, pressure preserves the peak width but increases the phonon energy and results in Raman spectra that are blue shifted with respect to the relaxed case.

As indicated before, Raman lines from as-grown crystals are observed to be significantly blue shifted from their expected positions. No splitting of the Raman peak, or significant broadening beyond that due to phonon confinement, is observed. Thus, the pressure exerted on as-grown crystals is taken to be purely hydrostatic. This comes as no surprise since the nanocrystals are embedded in an isotropic amorphous matrix. For the case of nanocrystals embedded in an anisotropic crystalline matrix, it is conceivable that uniaxial stress may readily develop.

As described in Chapter 4, liberation of nanocrystals relieves the pressure that accumulates during the growth process. This observation confirms that the interactions between the nanocrystal and matrix are responsible for the observed Raman line shifts to higher energies. The following expression, which is derived in detail in Appendix C, is

used to determine the average stress on nanocrystals:[102]

$$P = \frac{\omega_{embedded} - \omega_{liberated}}{3\gamma_{m-G}\omega_{liberated}(S_{11} + S_{12})} \tag{6.1}$$

where γ_{m-G} is the mode-Grüneisen parameter, S_{11} and S_{12} are elastic compliance tensors, and $\omega_{embedded}$ and $\omega_{liberated}$ are the Raman frequencies of the nanocrystals embedded in the oxide matrix and those that have been liberated, respectively. Cerdeira, *et al.*[102] give values of 0.440×10^{-12} cm^2 dyn^{-1} and 0.89 for (S_{11} + S_{12}) and γ_{m-G}, respectively. This method for calculating the hydrostatic pressure of nanocrystals assumes that the surface tension for the air/Ge and SiO_2/Ge interfaces are similar and no appreciable coarsening of the nanocrystals occurs. The former assumption is supported by the observation that no significant difference is observed between the Raman line positions of liberated nanocrystals and fully stress-relieved nanocrystals produced by 48 hours of post annealing at 800 °C, and the latter is supported by AFM and TEM determination of the nanocrystal size distribution subsequent to post-annealing. Both observations will be discussed in the following chapters (Chapter 6.4 & 6.5).

Pressure in as-grown nanocrystals has could alternately be determined by referencing the observed Raman line position to that expected by the phonon confinement model given by Equation 3.8. However, use of the Raman line positions of liberated nanocrystals to define a reference “zero” stress state (in fact, experience pressures due to from the Gibbs-Thomson effect, which will be discussed in Chapter 6.5) is likely more reliable for evaluating the nanocrystal stress state given the sensitivity of the phonon confinement model to the nanocrystal size distribution and to the precise form of the phonon confining function (see Chapter 3.2.2).

6.4 Nanocrystal Coarsening Rate

To ensure the validity of post-annealing data, it is necessary to determine whether the nanocrystal size distribution changes significantly with post-growth thermal annealing. At present, no systematic data is available relating annealing and post-growth annealing conditions to nanocrystal size distributions. Previously, accurately obtaining such data required significant effort using TEM. With the discovery that AFM can be used to obtain size distributions, these data should be available shortly. However, AFM size distribution data are currently available for the longest annealing time at the highest temperature as shown in Figure 6.1. This distribution thus gives the maximum change in size due to post annealing treatments. The average as-grown nanocrystal diameter is 5.1

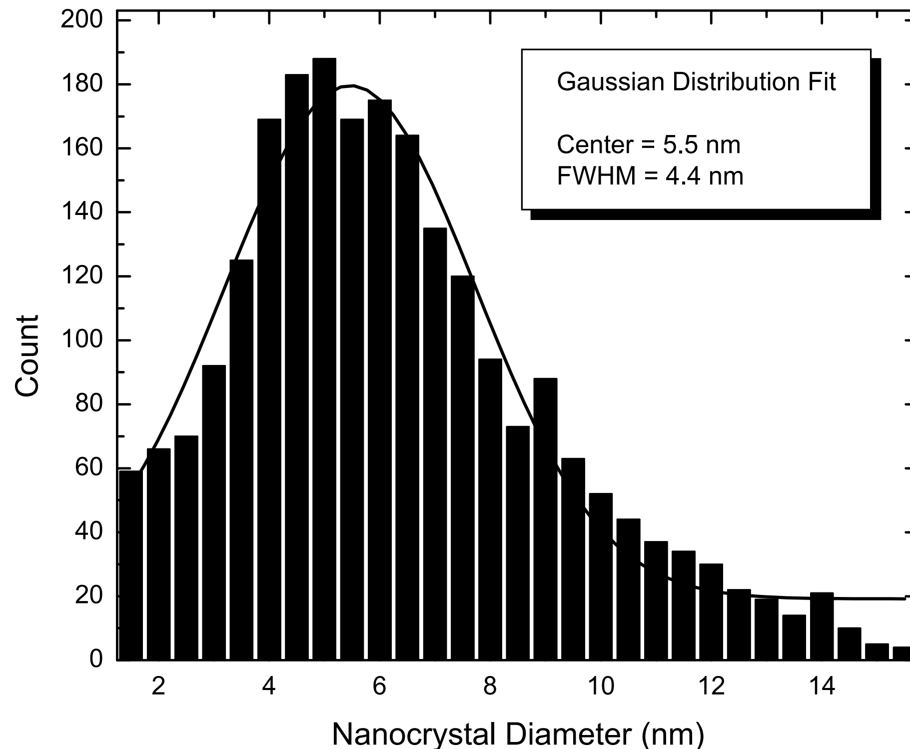

Figure 6.1: Size distribution of liberated Ge nanocrystals after post annealing at 800 °C for 48 hours obtained by AFM. The mean size, determined through a Gaussian fit to the experimental data, is 5.5 nm and the FWHM is 4.4 nm, indicating that only a small amount of coarsening occurs during post annealing.

nm with a 3.4 nm FWHM. After the most aggressive post-annealing treatment (800 °C for 48 hours), which is observed to fully relax the initial stress, the average nanocrystal diameter increases to 5.5 nm with a 4.4 nm FWHM. Such change in size is consistent with slight nanocrystal coarsening. Since all pressure is relieved after only 8 hours of post annealing at 800 °C (see Chapter 6.7), these results suggest that nanocrystal coarsening does not play a significant role in the stress relief process. The mechanistic stress relief model, therefore, will not include changes in nanocrystal size distributions during post-growth annealing.

6.5 Surface Free Energy

To verify the validity of the approximation that the surface free energy of the liberated nanocrystals is similar to that of the embedded crystals, Raman line positions from stress-relieved nanocrystals embedded in the SiO_2 matrix, which were obtained by post-growth thermal annealing, were compared to spectra from fully stress-relieved nanocrystals (after the same thermal treatment) that were liberated. It should be noted that this experiment is capable only of giving the relative difference in the surface free energies of embedded and liberated nanocrystals and is unable to give absolute values.

Small particles necessarily experience a size-dependent pressure as a result of the Gibbs-Thomson effect. The expression for pressure with radius, which is derived in Appendix D, is:[142]

$$P^{G-T} = \frac{2\gamma}{r} \tag{6.2}$$

where γ is the interfacial energy between the nanocrystal and its surroundings and r is its radius. For the case of a Ge nanocrystal, the radius is extremely small, and these pressure effects can be large.

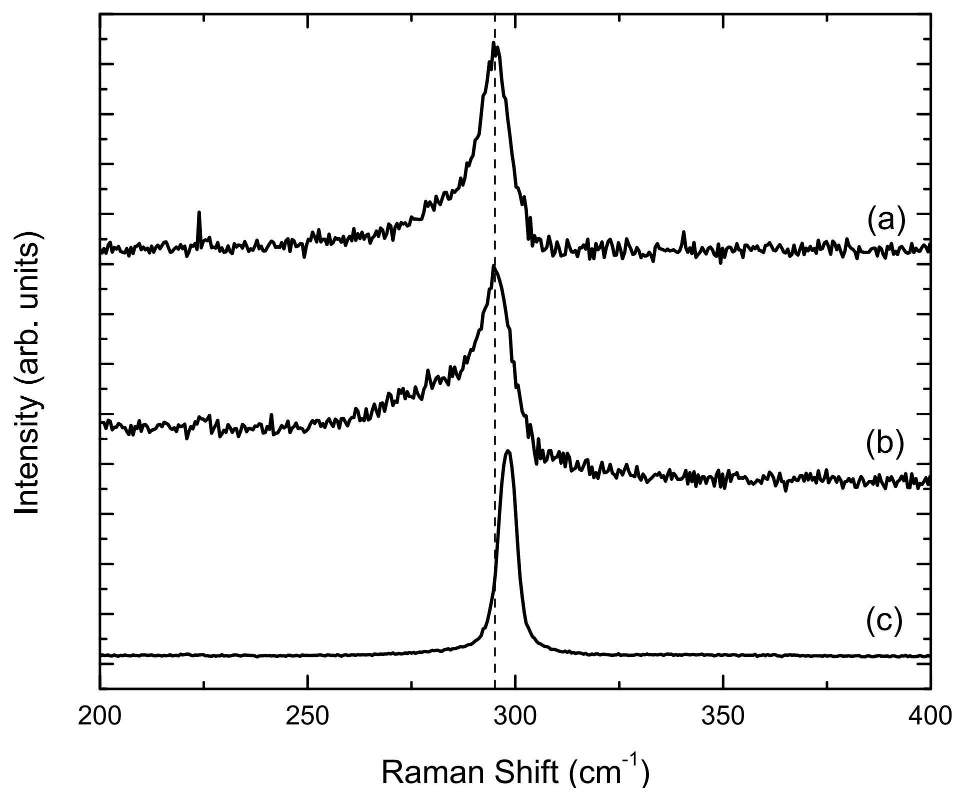

Figure 6.2: Raman spectra from stress-relieved ^{74}Ge nanocrystals embedded in silicon dioxide (a), stress-relieved nanocrystals after liberation (b), and the bulk ^{74}Ge reference sample. No significant difference between the Raman line positions of embedded and liberated nanocrystals is observed. This proves that the difference between the surface free energies of embedded and liberated nanocrystals is within the error of the Raman experiment.

No significant difference is observed between the Raman line positions of stress-relieved nanocrystals embedded in the SiO_2 matrix and liberated stress-relieved nanocrystals after liberation, as shown in Figure 6.2. As shown in previous chapters, the liberation process preserves the nanocrystal size distribution (Chapter 4.6). Therefore, variations of nanocrystal radius may be neglected when comparing the surface free energies. This result does not imply that the interfacial energy of the liberated nanocrystals is identical to that of embedded nanocrystals. Indeed, they almost certainly deviate from one another. However, this experiment does illustrate that the difference between the two interfacial energies is within the error of the Raman measurement. As a

result, it is not necessary to model interfacial energy differences when comparing the stress states of embedded and liberated nanocrystals.

6.6 Aggregation Pressure

An expression for the nanocrystal pressure arising from the growth process aggregation pressure has been derived by Diana Yi and Professor Daryl Chrzan, and the results are repeated here.[141] Details of their derivation are presented in Appendix E for completeness. The total absolute pressure on nanocrystals, P_o^{NC}, originates from two sources and may be expressed as:[141]

$$P_o^{NC} = P_{G-T} + P_{Agg} \tag{6.3}$$

First, the size dependent compressive pressure arising from the Gibbs-Thomson effect, P_{G-T}, is given by Equation 6.2. Second, the matrix exerts an additional pressure, P_{Agg}, on the nanocrystals arising from the growth process itself. Since Raman pressure measurements are referenced to the liberated state and surface energy differences are neglected, the measured pressure to which the theoretical model will be fit is P_{Agg}. Therefore, the relaxed radius of the nanocrystal, R_o^{NC}, is larger than the relaxed radius of the matrix void which forms to accommodate the nanocrystal, R_o^{Matrix}, and both the nanocrystal and the silica matrix near the nanocrystals are strained.

This model assumes nanocrystals are spherical and elastically isotropic and maintain intimate contact with the surrounding matrix at all times such that the radius of the strained nanocrystal is equivalent to the radius of the strained matrix void. TEM micrographs show that nanocrystals are, indeed, spherical. Furthermore, the silica matrix is assumed to be an elastically isotropic infinite medium, which is a good approximation

considering the amorphous state of silica. Taking these assumptions into account, and invoking classical elasticity theory with appropriate boundary conditions of stress continuity at the interface, the radius of the strained matrix void, prior to post annealing, is:

$$R_o^{Matrix} = \left(\frac{1 - \frac{P_o^{NC}}{3B_{NC}}}{1 + \frac{1}{4\mu^{Matrix}} \left[P_o^{NC} - \frac{2\gamma}{R_o^{NC}} \right]} \right) R_o^{NC} \tag{6.4}$$

where μ^{Matrix} is the shear modulus of the matrix, B_{NC} is the bulk modulus of the nanocrystal, and γ is the nanocrystal-matrix interfacial energy. The terms P_o^{NC} and R_o^{NC} are the quantities defined above. Since pressure within nanocrystals accumulates at 900 °C and Raman measurements are performed at room temperature, it is also necessary to account for thermal contraction upon cooling in the expressions for all radii. This effect will be discussed in Chapter 6.7.

Significant evidence exists suggesting that the nanocrystals are solid during growth. Therefore, the following model is proposed to describe the origin of the aggregation pressure during growth of solid nanocrystals. At the growth temperature, Ge atoms have enhanced thermal mobilities which allow them to move rapidly through the silica and form nuclei as large, or larger, than the critical nucleus size. Once stable, nanocrystals rapidly grow, resulting in the size distribution shown in Figure 4.8. Solid phase growth, which occurs by the diffusion of Ge atoms to the surfaces of nanocrystals, proceeds much more rapidly than void growth within the SiO_2 matrix. As a result, significant pressures accumulate and both the nanocrystal and the matrix surrounding the nanocrystal become strained. It is important to point out that the quantitative theory

describing stress relaxation does not depend on the specific mechanism of stress accumulation. Thus this model for stress generation, which was developed in response to the nanocrystal melting point observations presented in the previous chapter, provides an alternative to the solidification-induced stress mechanism.

6.7 Stress Relief Mechanism

Equation 6.4 specifies the initial radius of a stressed void in the matrix as a function of the size of, and total pressure on, the nanocrystal. Thus, this equation gives the void radius immediately after quenching from the growth temperature. During post-annealing, it is assumed that the coarsening rate of nanocrystals is small and the relaxed nanocrystal radius is assumed to be constant and equal to the initial radius, R_o^{NC}. The matrix void grows to relieve the stress and better accommodate the nanocrystal volume through the diffusive flux of matrix atoms away from the nanocrystal. By stipulating that the radius of the matrix void, R_{Matrix}, and the observed total pressure, P^{NC}, vary with annealing time and temperature, Equation 6.4 is rearranged to give the total residual pressure as:

$$P^{NC}(t) = \frac{12 B_{NC} \mu^{Matrix} \left(R_o^{NC} - R_{Matrix}(t) \right) + 3 B_{NC} R_{Matrix}(t) \frac{2\gamma}{R_o^{NC}}}{4 \mu^{Matrix} R_o^{NC} + 3 B_{NC} R_{Matrix}(t)} \qquad (6.5)$$

Therefore, as the radius of the matrix void increases, the total pressure on the nanocrystal decreases.

To determine the time evolution of stress during the annealing process it is necessary to develop a model for the change of the radius of the matrix void with time

and annealing temperature. Again, the complete derivation of this relationship,[141] will not be given here, but may be found in Appendix E.

It is assumed that stress fields within the matrix do not interact so that the problem may be solved by considering the dynamics of the matrix surrounding a single nanocrystal. The exact nature of the diffusing species is not specified here but its volume, Ω, is set equal to that of a SiO_2 molecule (45.3 Å^3). This interstitial species is assumed to diffuse through the silica. In an amorphous material, the spaces between the randomly oriented and tetragonally bonded SiO_2 molecules are considered interstitial sites. For diffusion to occur via this mechanism, SiO_2 dissociates into subgroups consisting of Si, O, SiO, and O_2, though only elemental Si and O are considered here. The total activation energy governing the diffusional process, E_A^i, includes the energy of interstitial formation, E_F^i, and energy of migration, E_M^i. The formation energy includes the energies of dissociation of the silica molecule ($E^{Si}, 2E^O, -E^{SiO_2}$) and a term arising from the entropy of SiO_2, $k_B \ln c^{SiO_2}$, where c^{SiO_2} is the concentration of silicon dioxide molecules. These terms express the total activation energy in the following way:

$$\begin{aligned} E_A &= E_M^i + E_{Si} + 2E_O - E_{SiO_2} - k_B T \ln c_{SiO_2} \\ &= E_M^i + E_{Si} - 2E_O - \mu_{SiO_2} \end{aligned} \tag{6.6}$$

where μ_{SiO_2} is the chemical potential of SiO_2.

In response to the stress in the matrix near the nanocrystal/silica interface, interstitial matrix atoms are created with an equilibrium concentration that minimizes the free energy of the local system at the interface. The radius of the nanocrystal is assumed to increase much more slowly than interstitials diffuse so that the steady state diffusion equation may be applied.[143] Therefore, the matrix void volume is incrementally

increased by a volume Ω by steady state diffusion of interstitials away from the nanocrystal/matrix interface. Using these classical thermodynamic arguments and the steady state diffusion condition, along with appropriate boundary conditions, the time rate of change of the matrix void radius is expressed as:

$$\frac{dR^{Matrix}(t)}{dt} = \frac{D_o}{R_{Matrix}(t)} \exp\left(-\frac{E_A}{k_B T}\right)\left\{\exp\left[\left(P(t) - \frac{2\gamma}{R_{NC}}\right)\frac{\Omega}{k_B T}\right] - 1\right\} \tag{6.7}$$

where D_o is the pre-exponential constant for the diffusion of interstitial matrix atoms through amorphous silica and E_A is the total activation energy given by Equation 6.6. Equation 6.7 shows that the pressure provides the driving force for expansion of the cavity radius. When the stress relaxes to the value given by the surface tension alone, the term in square brackets goes to zero, and the cavity attains its equilibrium volume.

To obtain the absolute pressure as a function of annealing time and temperature, Equation 6.7 is solved, with Equation 6.5 providing the expression for $P(t)$, and using Equation 6.4 as the initial condition. The pressure given by Equation 6.5, however, is the absolute pressure, whereas pressure data obtained experimentally give the initial and residual aggregation pressures. Therefore, the residual aggregation pressure is obtained by subtracting the absolute saturation pressure (given as the solution to Equation 6.5 at long times) from the calculated absolute pressure during post annealing. The parameters used for a least squares fit to the data are P_o^{NC}, D_o, E_A, and γ. However, P_o^{NC} and γ are not independent parameters and they combine to give the initial aggregation pressure, P_{Agg}.

An important consideration, which is factored into the theoretical model but was not mentioned above, is the thermal expansion of the nanocrystals and the matrix at each

Table 6.1: Table of constants used in fit of theoretical stress relief model to experimental data.

Constant	Value	Description
B^{Ge}	77 GPa	Bulk modulus of nanocrystal
μ_{SiO2}	31 GPa	Shear modulus of matrix
α^{Ge}	6.5×10^{-6} K^{-1}	Thermal expansion coefficient of nanocrystal
α^{SiO2}	5.5×10^{-7} K^{-1}	Thermal expansion coefficient of matrix
Ω	45.3 $Å^3$	Volume of matrix molecule
R_o^{NC}	23.3 Å	Radius of nanocrystal
T	(K)	Annealing temperature

annealing temperature. Growth occurs at 900 ^oC, post annealing occurs at 600 ^oC, 700 ^oC, and 800 ^oC, and Raman measurements of the pressure are performed at room temperature. The change in radius with temperature is given by:

$$R_i(T_2) = R_i(T_1)\left[1 + \alpha_i\left(T_2 - T_1\right)\right] \qquad (6.8)$$

Equation 6.8 is used to modify the radii in Equations 6.4, 6.5, & 6.7 accordingly.

The constants used for the calculation are listed in Table 6.1. Figure 6.3 shows the fit of the theoretical model to the experimentally determined pressures as a function of post annealing time and temperature. The resulting fitting parameters are:

$$P_{Agg} = 1.2 \;\; GPa$$
$$D_o = 2.0\times10^{-8} \;\; cm^2\, s^{-1}$$
$$E_A = 2.6 \; eV$$

The error bars shown in Figure 6.3 are the standard deviation from repeated Raman line position measurements on each sample. The theoretical fits provide a good description of the experimental data and indicate that the diffusive flux of matrix material away from the nanocrystal/matrix interface is responsible for the relief of compressive pressure. The diffusivities for our range of temperatures vary from 10^{-20} cm^2/s to 10^{-23} cm^2/s. These results are similar to those one would obtain from extrapolation of previous experimental

results [144,145]. Therefore, this model may be used to predict nanocrystal stress states as a function of thermal treatments subsequent to nanocrystal growth, thereby providing an additional degree of freedom, beyond the size, for tuning the electrical and optical properties of nanocrystals.

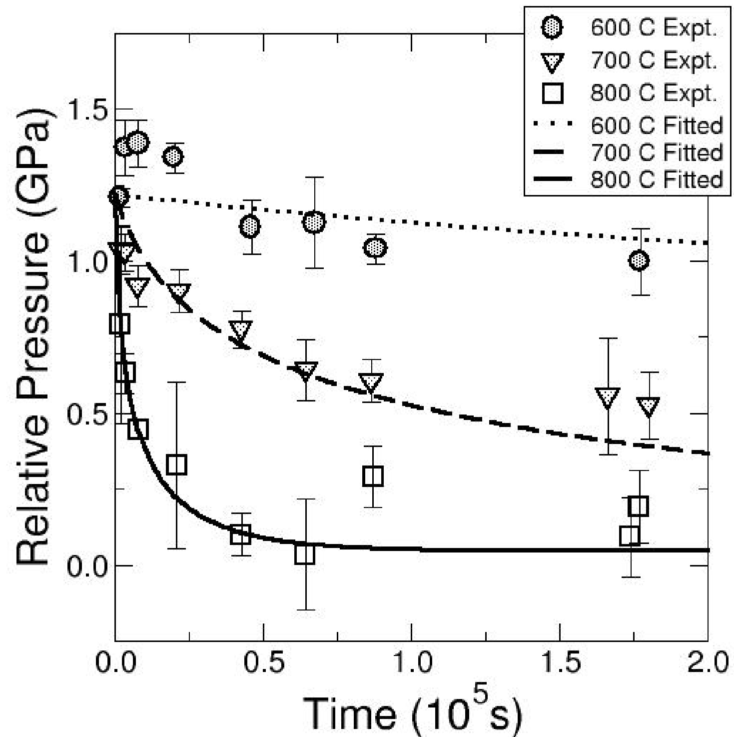

Figure 6.3: Pressure on Ge nanocrystals embedded in silica, measured relative to samples liberated from the matrix, as a function of post annealing times and temperatures. Lines are from the theoretical model described in the text and are fitted to experimental data with three adjustable parameters. The complete aggregation pressure of 1.2 GPa is relieved for samples annealed at 800 °C within a few hours. Lower annealing temperatures relieve the growth pressure at slower rates. Error bars are the standard deviation from repeated Raman line position measurements on each sample.

7. Conclusions and Future Work

^{70}Ge and ^{74}Ge nanocrystals have been synthesized in a silica matrix by ion implantation followed by thermal annealing. Nanocrystals in the as-grown state experience pressures in excess of 1 GPa. These pressures can be tuned by means of post-growth thermal annealing. The stress relaxation process can be accurately described by modeling the diffusive flux of matrix atoms away from the nanocrystal growth region. Use of this model to predict nanocrystal stress states may allow for precise bandgap engineering. Indeed, since semiconductor nanocrystals are expected to strongly interact with light due to quantum confinement effects,[53] it may be possible to precisely engineer radiative absorption and emission spectra using the stress model and experimental techniques presented here.

In-situ Raman spectroscopy and electron diffraction at elevated temperatures have been performed to characterize the melting behavior of nanocrystals and determine the mechanism of stress generation. Both experiments showed that the significant melting point depression which is well-known for free-standing nanocrystals does not occur for embedded Ge nanocrystals. In fact, *in-situ* electron diffraction shows a significant melting point hysteresis around the bulk Ge melting temperature. Further experiments will be performed to compare the melting behavior of embedded Ge nanocrystals to free-standing nanocrystals and determine the size-dependence of this effect. Additional *in-situ* Raman spectroscopy experiments, at both elevated and cryogenic temperatures, will be performed to characteristics of anharmonic phonon decay processes in confined systems.

Systematic growth experiments, combined with *ex-situ* Raman spectroscopy, have

shown that Ge is, most likely, solid during growth. However, Raman spectroscopy will be performed during the growth process itself to conclusively determine the Ge phase during nanocrystal formation. This will yield considerable information regarding the stress generation mechanism. Once the dynamics of stress evolution are more fully understood in this system, it may be possible to exploit compressive stresses to achieve self-organization and additional control over nanocrystal size distributions.

Selective etching of the oxide matrix has been achieved to obtain free standing Ge nanocrystals which are stable under ambient atmospheric conditions. It has been shown that this process does not significantly alter the nanocrystal size distribution, thus allowing for the rapid determination of nanocrystal sizes using atomic force microscopy. Ultrasonic cleaning in methanol baths has been used to decrease the surface nanocrystal density and transfer nanocrystals between surfaces. This process allows for transfer of nanocrystals to conducting substrates and will be used to prepare scanning tunneling microscopy samples for comprehensive surface and electronic characterization of individual nanocrystals. Methods of nanocrystal patterning and manipulation using these procedures will be explored.

Appendix A: Van der Waals Interactions

Van der Waals interactions provide the forces necessary for nanocrystals to accumulate on the surfaces of samples subsequent to etching, as discussed in Chapter 4. Here, the mathematical basis for these interactions will be described in more detail. As discussed previously, the pair potential arising from van der Waals forces between two atoms or molecules is given by (also Equation 4.2):[112]

$$U(d) = -\frac{C}{d^6} \tag{A.1}$$

where C is a constant and d is the interaction length. It is assumed that the van der Waals forces between larger bodies, such as nanocrystals and substrates, may be regarded as the summed forces between their constituent atoms or molecules.[112] Corrections will be applied later in the analysis that account for the errors introduced by this approximation.

To begin, it is necessary to derive an expression for the pair potential between an individual atom and a spherical particle. The derivation presented here follows closely that of Hamaker in 1937.[113] Equation A.1 is integrated over the volume of the particle, using the geometry shown in Figure A.1, to give the total potential arising from the summed interactions between an atom located at point *P* and the atoms making up a spherical particle whose center is located at point *O*. The volume of the shaded differential region shown in Figure A.1 is:

$$dV = \left\{ \int_0^{2\pi} d\varphi \int_0^{\theta_o} r^2 \sin\theta d\theta \right\} dr \tag{A.2}$$

Simple geometry gives a relationship between θ_o and the characteristic distances:

$$R_1^2 = R^2 + r^2 - 2rR\cos\theta_o \tag{A.3}$$

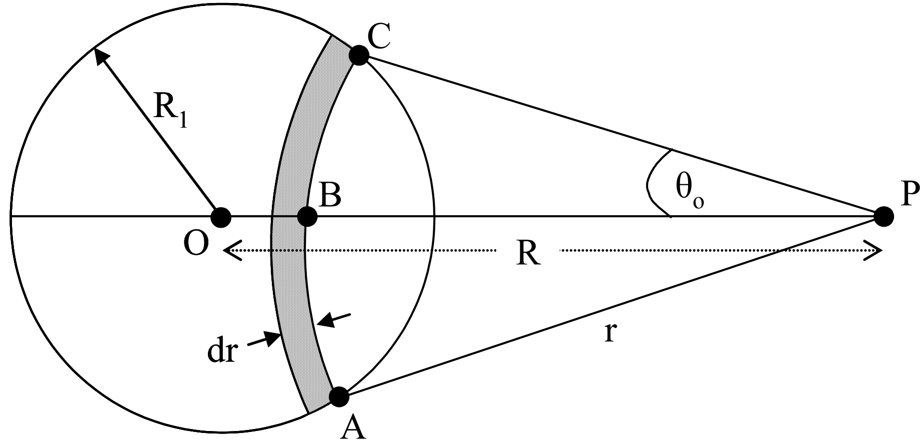

Figure A.1: Schematic diagram illustrating the integration procedure to obtain the pair potential between a single atom or molecule and a particle of radius R_1.

Partial integration of Equation A.2 yields:

$$dV = \frac{\pi r}{R}\left\{R_1^2 - (R-r)^2\right\}dr \tag{A.4}$$

The total number of atoms contained within the differential volume may be obtained by multiplying with the atomic density, ρ. The total potential energy may, therefore, be determined by integration the product of Equation A.4 and Equation A.1 over the entire spherical particle as follows:

$$U_P = -\int_{R-R_1}^{R+R_1} \frac{C\rho\pi r}{Rr^6}\left\{R_1^2 - (R-r)^2\right\}dr \tag{A.4}$$

Following this same procedure, it is possible to determine the potential between two spherical particles. Figure A.2 illustrates the integration procedure. The total potential between two spherical particles of radii R_1 and R_2 as a function of the separation between their surfaces, D, is:

$$\begin{aligned} U_P &= \int_{D-R_2}^{D+R_2} \frac{U_P \rho \pi R}{D}\left\{R_2^2 - (C-R)^2\right\}dR \\ &= \frac{-\pi^2\rho^2 C}{D}\int_{D-R_2}^{D+R_2}\left\{R_2^2 - (C-R)^2\right\}dR \int_{R-R_1}^{R+R_1} \frac{\left\{R_1^2 - (R-r)^2\right\}}{r^5}dr \end{aligned} \tag{A.6}$$

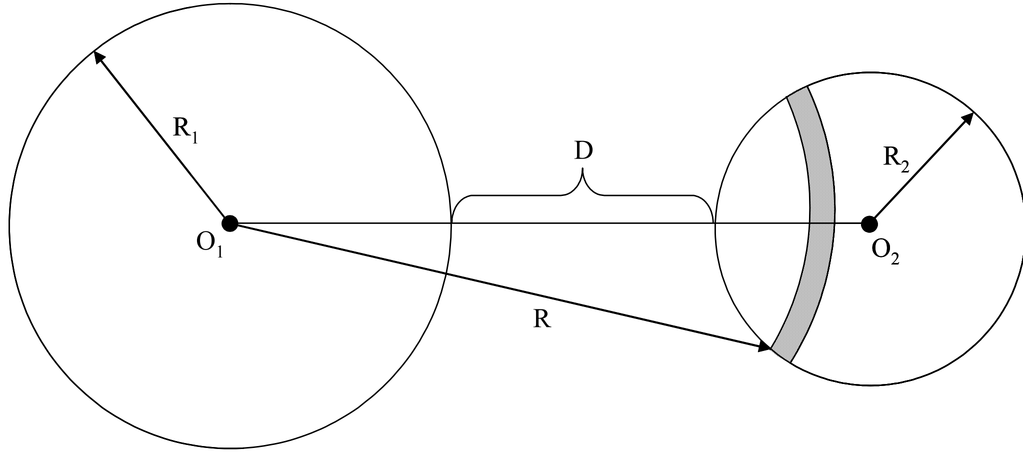

Figure A.2: Schematic diagram illustrating the integration procedure to obtain the pair potential between two particles of radii R_1 and R_2.

Integration and simplification of Equation A.6 gives a final expression for the van der Waals interaction potential between two spheres (Equation 4.3):[113]

$$U(D) = -\frac{A}{12}\left\{\frac{y}{x^2+xy+x} + \frac{y}{x^2+xy+x+y} + 2\ln\left(\frac{x^2+xy+x}{x^2+xy+x+y}\right)\right\} \qquad \text{(A.7)}$$

where $x = \frac{D}{2R_1}$, $y = \frac{R_2}{R_1}$, and $A = \pi^2 \rho^2 C$.

This equation may be easily modified to describe the interactions between a spherical particle and an infinite and flat substrate by setting the substrate radius, R_2, equal to infinity. Therefore, y becomes infinite and Equation A.7 reduces to:[113]

$$U(D) = -\frac{A}{12}\left\{\frac{1}{x} + \frac{1}{x+1} + 2\ln\left(\frac{x}{x+1}\right)\right\} \qquad \text{(A.8)}$$

The constant A is defined as the Hamaker constant. This parameter makes it possible to quantitatively account for the medium through which bodies interact. Furthermore, the Hamaker constant may correct for errors introduced in assuming direct summation of individual atomic interactions.

Derivation of the functional form of the Hamaker constant can be rather complex, and is beyond the scope of this work. For the case of a particle with dielectric constant ε_1, interacting with another particle or a surface with dielectric constant ε_2, through a medium with dielectric constant ε_3, the Hamaker constant is:[112]

$$A = \frac{3}{2} k_B T \sum_{n=0',1,2,\ldots}^{\infty} \left[\frac{\varepsilon_1(i\nu_n) - \varepsilon_3(i\nu_n)}{\varepsilon_1(i\nu_n) + \varepsilon_3(i\nu_n)} \right] \left[\frac{\varepsilon_2(i\nu_n) - \varepsilon_3(i\nu_n)}{\varepsilon_2(i\nu_n) + \varepsilon_3(i\nu_n)} \right] \tag{A.9}$$

The dielectric constants, $\varepsilon_j(i\nu_n)$ are evaluated at the imaginary frequencies $i\nu_n$, and the n = 0 term is multiplied by ½, as denoted by the prime. In order to evaluate this equation, the first term of the infinite sum is taken separately and the remaining terms, multiplied by $k_B T$, are replaced by an integral to yield:[112]

$$A = \frac{3}{4} k_B T \left[\frac{\varepsilon_1 - \varepsilon_3}{\varepsilon_1 + \varepsilon_3} \right] \left[\frac{\varepsilon_2 - \varepsilon_3}{\varepsilon_2 + \varepsilon_3} \right] + \frac{3h}{4\pi} \int_{\nu_1}^{\infty} \left[\frac{\varepsilon_1(i\nu_n) - \varepsilon_3(i\nu_n)}{\varepsilon_1(i\nu_n) + \varepsilon_3(i\nu_n)} \right] \left[\frac{\varepsilon_2(i\nu_n) - \varepsilon_3(i\nu_n)}{\varepsilon_2(i\nu_n) + \varepsilon_3(i\nu_n)} \right] d\nu \tag{A.10}$$

Equation A.10 may be evaluated by making the approximation:[112]

$$\varepsilon_j(i\nu) = 1 + \frac{\left(n_j^2 - 1\right)}{\left(1 + \dfrac{\nu^2}{\nu_{e,j}^2}\right)} \tag{A.11}$$

where n_j and $\nu_{e,j}$ are the refractive index and the main UV absorption frequency of medium j, respectively.

Table 4.3 gives the Hamaker constants, pair potentials, and van der Waals forces for all of the interactions that occur during the etching, ultrasonic cleaning, and characterization processes. For example, the force between two nanocrystals of average radius may be calculated in the following manner. The static dielectric constant and index of refraction of Ge are 16.0 and 4.01, respectively. During etching, the particles interact through a third medium, HF. The static dielectric constant and index of

refraction of HF are 83.6 and 9.14, respectively. Using Equations A.10 & A.11, along with the indices of refraction and dielectric constants of Ge and HF, the Hamaker constant may be calculated. Its value is 8.35×10^{19} J, or $291k_BT$ at room temperature. The potential between the two nanocrystals may be calculated using Equation A.7 by assuming that each nanocrystal has a radius of 2.5 nm and they are separated by a distance of 0.3 nm. The potential, for this case, is $-114.1k_BT$ at room temperature, where the negative sign indicates an attractive interaction. The total force acting between the two particles is calculated by taking the derivative of the potential with respect to the interaction length, *D*. The total force between two nanocrystals (5 nm diameter) that are immersed in HF is 8.9×10^{-10} N.

Appendix B: Temperature Dependence of Raman Line Shapes

In Chapter 5, results of variable temperature Raman spectroscopy are presented. Due to anharmonic effects, Raman spectra are significantly affected by changes in temperature. As temperature is increased, the first order Si phonon mode red shifts and the Raman line broadens. The former effect is exploited to calibrate the measurement temperature and the latter effect is used to compare phonon lifetimes of Ge nanocrystals to bulk crystalline Ge. The theoretical bases for these phenomena are presented here.

The temperature dependent phonon frequency, $\omega(T)$, may be written as:

$$\omega(T) = \omega_o + \Delta(T) \tag{B.1}$$

where ω_o is the harmonic frequency of the zone center optical phonon mode and $\Delta_o(T)$ is the perturbation of the real part of the phonon self-energy with temperature. This term may be divided into two components in the following manner:

$$\Delta(T) = \Delta^{(1)}(T) + \Delta^{(2)}(T) \tag{B.2}$$

where $\Delta^{(1)}(T)$ is the contribution from thermal expansion and $\Delta^{(2)}(T)$ is the contribution from phonon-phonon coupling. Neither of these effects can be described within the framework of the harmonic oscillator approximation.

To determine the contribution of thermal expansion to the frequency shift of the Raman active phonon mode, consider the definition of the mode-Grüneissen parameter, γ:[146]

$$\gamma = -\frac{d\ln\omega}{d\ln V} = -V\frac{d\ln\omega}{dV} \tag{B.3}$$

The volume thermal expansion coefficient, $\alpha_V(T)$, is defined as:

$$\alpha_V(T) = \frac{1}{V}\left(\frac{dV}{dT}\right)_P = 3\alpha_l(T) \tag{B.4}$$

where $\alpha_l(T)$ is the linear coefficient of thermal expansion. Therefore,

$$d\ln\omega(T) = -3\gamma\int_0^T \alpha_L(T)dT \tag{B.5}$$

Thus, the change in the phonon frequency arising from thermal expansion is given by:[123]

$$\Delta^{(1)}(T) = \omega_{oi}\left[\exp\left\{-3\gamma_i\int_0^T \alpha_L(T)dT\right\} - 1\right] \tag{B.6}$$

The second contribution to the change in phonon frequency with temperature is due to phonon-phonon coupling. Kittel concisely describes this coupling process in the following way:[98]

> the presence of one phonon causes a periodic elastic strain which (through the anharmonic interaction) modulates in space and time the elastic constant of the crystal. A second phonon perceives the modulation of the elastic constant and thereupon is scattered to produce a third phonon, just as from a moving three-dimensional grating.

Therefore, phonon coupling is considered a decay process. Three-phonon coupling involves the decay of one phonon to two new phonons through interaction with another phonon. This process may be described by the perturbation Hamiltonian for the decay of one optical phonon into two acoustic phonons:[125]

$$H' = \sum_{\vec{k},\vec{k}',\vec{k}'',\vec{x}} e^{i(\vec{k}-\vec{k}'-\vec{k}'')\bullet\vec{x}} c(\vec{k},\vec{k}',\vec{k}'')a(\vec{k})a^\dagger(\vec{k}')a^\dagger(\vec{k}'') \tag{B.7}$$

where $c(\vec{k},\vec{k}',\vec{k}'')$ is the anharmonic coupling coefficient, $a(\vec{k})$ is the annihilation operator for the Raman active optical phonon ($\vec{k}$) and $a^\dagger(\vec{k}')$ and $a^\dagger(\vec{k}'')$ are the

creation operators for the acoustic phonons ($\vec{k}'$ and $\vec{k}''$) into which the optical phonon decays. The creation and annihilation operators are related to the phonon occupation number, N, by:[125]

$$\begin{aligned} a^{\dagger} &= \left(\frac{\hbar}{M\omega}\right)^{1/2} (N+1)^{1/2} \\ a &= \left(\frac{\hbar}{M\omega}\right)^{1/2} N^{1/2} \end{aligned} \tag{B.8}$$

The phonon occupation number is given by a Bose-Einstein distribution.[97]

The most straightforward way to obtain an expression for the change of the Raman line position as a function of temperature is to determine the temperature dependence of the Raman line width. The temperature dependent line width, $\Gamma(T)$, is given by the perturbation of the imaginary part of the phonon self energy. Therefore it may be related to the change in phonon frequency (which is given by the perturbation of the real part of the phonon self energy) by the Kramers-Kronig relation.[126]

Due to the Heisenberg Uncertainty relationship $\Delta t \Delta E \geq \hbar$, line broadening arising from the finite temperature of the system is proportional to the inverse of the relaxation time, τ. The relaxation time, in turn, is inversely proportional to the time derivative of the occupation number of the Raman active phonon:[127]

$$\Gamma(T) \propto \frac{1}{\tau} \propto \frac{d(\delta N)}{dt} \tag{B.9}$$

Where δN is the deviation of the occupation number of the optical phonon from thermal equilibrium. This quantity may be calculated for each of the phonon interactions using the fact that the time derivative of the occupation number is proportional to the square of the Hamiltonian matrix elements between the initial and final phonon states according to

Fermi's Golden Rule. Including the contribution of the reverse process as well, the time derivative of Equation B.9, for the three phonon process, is:[123]

$$\frac{d(\delta N)}{dt} \propto \left[a^{\dagger}(\vec{k})a(\vec{k}')a(\vec{k}'')\right]^2 - \left[a(\vec{k})a^{\dagger}(\vec{k}')a^{\dagger}(\vec{k}'')\right]^2 \quad \text{(B.10)}$$

Substituting in the relevant annihilation and creation operators, as defined for Equation B.7, we obtain:

$$\frac{d(\delta N)}{dt} \propto (N + \delta N + 1)N'N'' - (N + \delta N)(N'+1)(N''+1) \quad \text{(B.11)}$$

where N is the occupation number of the optical phonon and N' and N'' are the occupation numbers of the two acoustic phonons. At equilibrium, there is no change in the optical phonon occupation number, and

$$(N+1)N'N'' = N(N'+1)(N''+1) \quad \text{(B.12)}$$

which yields:

$$\frac{d(\delta N)}{dt} \propto -(1 + N' + N'')\delta N \quad \text{(B.13)}$$

Combining Equations B.9 & B.13 and inserting a proportionality constant, A, the line broadening arising from three phonon interactions is:

$$\Gamma(T) = A\left(1 + \frac{1}{e^{\hbar\omega'/k_B T}} + \frac{1}{e^{\hbar\omega''/k_B T}}\right) \quad \text{(B.14)}$$

For the case of bulk crystals, $\vec{k} = \vec{k}' + \vec{k}'' = 0$ and it is typically assumed that the optical phonon decays to two LA phonons. So $\omega' = \omega'' = \frac{1}{2}\omega_0$, and Equation B.14, for three phonon coupling, reduces to:

$$\Gamma_3(T) = A\left(1 + \frac{2}{e^{\hbar\omega_0/2k_B T}}\right) \quad \text{(B.15)}$$

Balkanski *et al.*[124] have shown experimentally that the three-phonon interaction is insufficient to explain the observed Si line broadening at high temperatures. As temperature is increased, four phonon processes, corresponding to the quartic anharmonic terms in the bonding potential, become increasingly important. The contribution of the four-phonon process can be quantified by following the method described above for the three phonon process. The characteristic rate equation for the four phonon process is:

$$\frac{d(\delta N)}{dt} \propto (N+\delta N+1)N'N''N''' - (N+\delta N)(N'+1)(N''+1)(N'''+1) \tag{B.16}$$

The corresponding equilibrium condition is:

$$(N+1)N'N''N''' = N(N'+1)(N''+1)(N'''+1) \tag{B.17}$$

Again, only contributions from LA phonons are considered so that $\omega' = \omega'' = \omega''' = \frac{1}{3}\omega_0$ and the expression for the four phonon contribution to Raman line broadening with temperature becomes:

$$\Gamma_4(T) = B\left[1 + \frac{3}{e^{\hbar\omega_0/3k_BT} - 1} + \frac{3}{\left(e^{\hbar\omega_0/3k_BT} - 1\right)^2}\right] \tag{B.18}$$

Thus, the total broadening from anharmonic phonon coupling is:

$$\Gamma(T) = A\left(1 + \frac{2}{e^{\hbar\omega_0/2k_BT}}\right) + B\left[1 + \frac{3}{e^{\hbar\omega_0/3k_BT} - 1} + \frac{3}{\left(e^{\hbar\omega_0/3k_BT} - 1\right)^2}\right] \tag{B.19}$$

As described before, the line broadening in related to the change in the peak position by the Kramers-Kronig relation:[126]

$$\Delta_i^{(2)}(\omega, T) = \frac{1}{\pi}\int_{-\infty}^{\infty} \frac{\Gamma(\omega', T)}{\omega - \omega'} d\omega' \tag{B.20}$$

The resulting change in optical phonon frequency with temperature due to both three and four phonon coupling is:[123]

$$\Delta_i^{(2)}(T) = C\left(1+\frac{2}{e^{\hbar\omega_0/2k_BT}}\right) + D\left[1+\frac{3}{e^{\hbar\omega_0/3k_BT}-1}+\frac{3}{\left(e^{\hbar\omega_0/3k_BT}-1\right)^2}\right] \tag{B.21}$$

Figures 5.2(a) & 5.2(b) in show plots of the calculated position and width of the Si Raman line as a function of temperature and Chapter 5.2.2 gives a description of the selection of the constants *A*, *B*, *C*, and *D*.

Appendix C: Pressure Dependence of Raman Line Positions

Raman spectroscopy experiments show that as-grown nanocrystals are under significant compressive stress. The Raman line position is blue shifted with respect to the expected position, which is characteristic of hydrostatic pressure. Furthermore, no additional line broadening, which would indicate shear stress, is observed. Here, the pressure dependence of the Raman line position with pressure is derived following the treatment of Cerdeira *et al*.[102] The dynamical equation for the zone center optical phonon modes under stress may be written by equating Hooke's Law and Newton's equation of motion:

$$\overline{m}\frac{d^2u_i}{dt^2} = -\left(K_{ii}^{(0)}u_i + \sum_{klm} K_{iklm}^{(1)}\varepsilon_{lm}u_k\right) \tag{C.1}$$

Where u_i represents the component i (x, y, or z direction) of the displacement of two atoms in the unit cell, $\overline{m}$ is the reduced mass, $K_{ii}^{(0)}$ is the effective spring constant for an unstrained system, ε_{lm} is the strain, and $K_{iklm}^{(1)}$ gives the change in the effective spring constant with strain ($K_{iklm}^{(1)} = \partial K_{ik} / \partial \varepsilon_{lm}$) due to anharmonic contributions to the bonding potential. $K_{ii}^{(0)}$ is equivalent to $\overline{m}\omega_o^2$, where ω_o is the unstrained zone center optical phonon frequency.

Equation C.1 may be greatly simplified by considering the symmetry of the cubic system. Only the $K_{iklm}^{(1)}$ tensor components which are invariant under application of the four three-fold symmetry operations along $[111], [\overline{1}11], [1\overline{1}1] \& [\overline{1}\,\overline{1}1]$ are allowed. These three-fold rotation operations result in the following transformations of the cubic axes:[98]

$$
\begin{aligned}
&x \to y \to z \to x \\
&x \to z \to -y \to x \\
&x \to -z \to y \to x \\
&x \to -y \to -z \to x
\end{aligned}
$$

Thus, the 36 available $K^{(1)}_{iklm}$ tensor components may be reduced to the three independent and non-zero tensor components defined below:[102]

$$
\begin{aligned}
K^{(1)}_{1111} &= K^{(1)}_{2222} = K^{(1)}_{3333} = \overline{m}p \\
K^{(1)}_{1122} &= K^{(1)}_{2233} = K^{(1)}_{1133} = \overline{m}q \\
K^{(1)}_{1212} &= K^{(1)}_{2323} = \overline{m}r
\end{aligned}
\tag{C.2}
$$

Equation C.1 may be further simplified by analyzing the stress tensor. Diagonal matrix elements of the third-rank stress tensor imply bond length contraction and expansion, whereas off-diagonal matrix elements require bond angle modification. For hydrostatic pressure of magnitude *P*, the stress tensor is a diagonal matrix of the form:[98]

$$
X = \begin{pmatrix} -P & 0 & 0 \\ 0 & -P & 0 \\ 0 & 0 & -P \end{pmatrix} \tag{C.3}
$$

Therefore, the strain components become $\varepsilon_{xx} = \varepsilon_{yy} = \varepsilon_{zz} = \varepsilon$, and the shear components become zero, which will lead to a diagonal dynamical matrix. Combining the above relations, Equation C.1 may be reduced to:

$$
\frac{d^2 u_i}{dt^2} = -u_i\left[\omega_0^2 + \varepsilon(p + 2q)\right] \tag{C.4}
$$

Thus, it is possible to construct the dynamical matrix and solve the following simple secular equation to obtain a solution for the Raman line position of crystals under hydrostatic pressure, ω_H:

$$\begin{vmatrix} \omega_o^2 + \varepsilon(p+2q) - \omega_H^2 & 0 & 0 \\ 0 & \omega_o^2 + \varepsilon(p+2q) - \omega_H^2 & 0 \\ 0 & 0 & \omega_o^2 + \varepsilon(p+2q) - \omega_H^2 \end{vmatrix} = 0 \qquad \text{(C.5)}$$

$$\omega_H^2 - \omega_o^2 = (p+2q)\varepsilon \qquad \text{(C.6)}$$

To solve for the change in the phonon frequency with hydrostatic pressure, the following assumption is made:

$$\omega_H \approx \omega_o + \frac{\omega_H^2 - \omega_o^2}{2\omega_o} \qquad \text{(C.7)}$$

Therefore, through substitution of Equation C.6 into Equation C.7 and setting $\Delta\omega_H = \omega_H - \omega_0$, following relationship for the change in the Raman line position as a function of the strain is obtained:

$$\Delta\omega_H = \frac{(p+2q)\varepsilon}{2\omega_o} \qquad \text{(C.8)}$$

This may be related to the hydrostatic pressure, *P*, through the standard expression for the Bulk modulus as a function of the elastic compliance tensors:[98]

$$B = -\frac{P}{(\Delta V / V)} = -\frac{P}{3\varepsilon} = \frac{1}{3(S_{11} + 2S_{12})} \qquad \text{(C.9)}$$

$$\varepsilon = -P(S_{11} + 2S_{12}) \qquad \text{(C.10)}$$

Combining Equations C.8 and C.10, gives:

$$\Delta\omega_H = \frac{-P(p+2q)}{2\omega_o}(S_{11} + 2S_{12}) \qquad \text{(C.11)}$$

The mode-Grüneisen parameter, γ, is defined as:[102]

$$\gamma = -\frac{(p+2q)}{6\omega_0^2} \qquad \text{(C.12)}$$

Substitution of Equation C.12 into Equation C.11, yields:

$$P = \frac{\Delta\omega_H}{3\gamma\omega_0(S_{11} + 2S_{12})} \quad \text{(C.13)}$$

Cerdeira, *et al.*[102] give values of 0.440×10^{-12} cm^2 dyn^{-1} and 0.89 for $(S_{11} + S_{12})$ and γ, respectively. In the present case, it is assumed that the elastic compliance tensors and the mode-Grüneisen parameter are equivalent for bulk and nanocrystalline Ge. Here, ω_o is determined from the Raman line position of liberated nanocrystals ($\omega_{liberated}$) and $\Delta\omega_H$ is the difference in Raman line positions between the embedded nanocrystals ($\omega_{embedded}$) and the liberated nanocrystals. Thus, the final version of Equation C.13, which is used for determination of nanocrystal stress states, becomes:

$$P = \frac{\omega_{embedded} - \omega_{liberated}}{3\gamma\omega_{liberated}(S_{11} + S_{12})} \quad \text{(C.14)}$$

Appendix D: The Gibbs-Thomson Effect

It is well known that surface tension results in a size-dependent pressure on materials. Owing to the extremely small radius of Ge nanocrystals, this pressure is significant in the present case. The thermodynamic basis for this pressure will be presented here following the derivation by Porter & Easterling.[142] Figure D.1 shows a theoretical two phase system containing a phase α which has a flat interface with a second phase, β. Since this interface is perfectly flat, its radius of curvature is infinite. A spherical precipitate of phase β, with a radius of curvature equal to r, is located within the α phase. If some quantity of β, dn_β, is transferred from the flat interface to the precipitate, the Gibbs free energy change of the system will be:

$$dG = \left(G_\infty - G_r\right)dn = \Delta G_r dn \quad \text{(D.1)}$$

where G_∞ and G_r are the molar free energies at the flat interface and the spherical interface, respectively. The total change in the Gibbs free energy may be related to the interfacial energy, γ, which is assumed to be independent of r, as follows:

$$dG = \gamma dA_r + \gamma dA_\infty \quad \text{(D.2)}$$

The total area of the flat interface, dA_∞, does not change an appreciable amount.

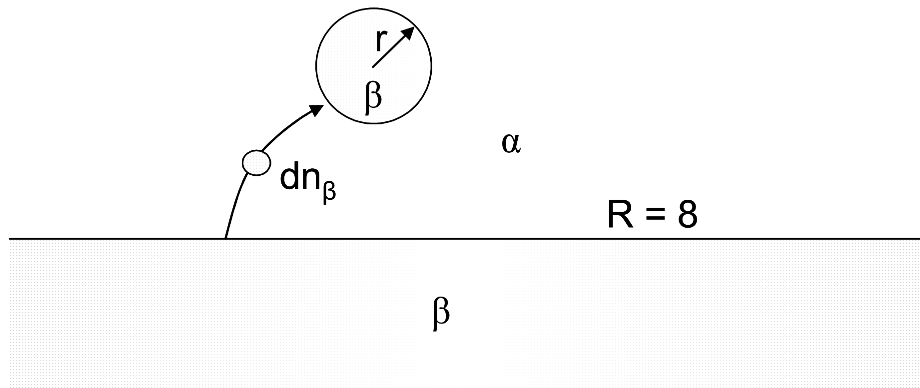

Figure D.1: Theoretical construction of a two-phase system to describe the thermodynamics of the size-dependent pressure within a particle, also known as the Gibbs-Thomson effect.[142]

However, the change in the interfacial area between the spherical precipitate and the α matrix will increase, by an amount dA_r, and the total change in free energy will be:

$$dG = 8\pi r\gamma dr = \Delta G_r dn \tag{D.3}$$

The number of moles in the spherical precipitate is simply the total volume divided by the molar volume, V_m, so that

$$n = \frac{4\pi r^3}{3V_m} \rightarrow dn = \frac{4\pi r^2}{V_m} dr \tag{D.4}$$

Combining equations D.3 and D.4 yields:

$$\Delta G_r = \frac{2\gamma V_m}{r} \tag{D.5}$$

Equation D.5 gives the change in the Gibbs free energy of a particle as a function of radius. This may be related to the pressure of the particle using the well-known equation of state:

$$dG = -SdT + VdP \tag{D.6}$$

Thus, at constant temperature, the change of free energy with pressure is:

$$\Delta G = V_m \Delta P \tag{D.7}$$

Equating equations D.5 and D.7, yield the final expression for the pressure as a function of radius:

$$\Delta P = \frac{2\gamma}{r} \tag{D.8}$$

Appendix E: Diffusive Stress Relaxation Model

The equations describing the diffusive stress relaxation process discussed in Chapter 6 were developed by Diana Yi (GSRA in AS&T, UCB) and Professor Daryl Chrzan.[141] For completeness, the derivation is repeated here. In the first part of the derivation, elasticity theory is used to find expressions for the initial matrix cavity radius, which provides the initial condition for subsequent modeling, and the total nanocrystal pressure as a function of the time-dependent matrix cavity radius. In the second part of the derivation, thermodynamic equilibrium is imposed at the Ge/SiO_2 interface to obtain the concentration of interstitials contributing to the stress relief process and a steady state diffusion condition is applied to determine the change in the matrix cavity radius with time.

The nanocrystals are observed to be very nearly spherical, the amorphous matrix is isotropic, and the compressive stress is purely hydrostatic. Therefore, it is natural to approach this problem in spherical coordinates. The displacement of any point in the nanocrystal due to the applied pressure is

$$\vec{D} = u_r \vec{i}_1 + u_\theta \vec{i}_2 + u_\phi \vec{i}_3 \qquad \text{(E.1)}$$

However, since all forces incident on the nanocrystal are spherically symmetric displacement within the nanocrystal occurs in the radial direction only, and:

$$\vec{D} = u_r \vec{i}_1 = u \vec{i}_1 \qquad \text{(E.2)}$$

The strain tensor, in spherical coordinates, is reduced to the following set of equations:

$$\begin{aligned} \varepsilon_{rr} &= \frac{du}{dr} \\ \varepsilon_{\theta\theta} &= \varepsilon_{\phi\phi} = \frac{u}{r} \\ \varepsilon_{r\phi} &= \varepsilon_{r\theta} = \varepsilon_{\theta\phi} = 0 \end{aligned} \qquad \text{(E.3)}$$

The dilation, δ, gives the ratio of the change of volume due to hydrostatic pressure to the relaxed volume. Therefore, the dilation may be equated to the trace of the strain tensor, which from Equation E.3 yields[147]

$$\delta = \frac{du}{dr} + \frac{2u}{r} \tag{E.4}$$

All forces are incident on the surface of the nanocrystal and no body forces are present. Hence, the dilation does not vary in the radial direction, and:[148]

$$\frac{d}{dr}(\delta) = \frac{d}{dr}\left(\frac{du}{dr} + \frac{2u}{r}\right) = 0 \tag{E.5}$$

Equation E.5 can be integrated to obtain the radially dependent displacement, u:

$$u = a + \frac{b}{r^2} \tag{E.6}$$

Combining the stress-strain relationship for the spherical system and Equations E.3, E.4 & E.6, the radial and angular stress components as a function of radius become:[148]

$$\begin{aligned} \sigma_{rr} &= \frac{aE}{(1-2\nu)} - \frac{2bE}{(1+\nu)r^3} \\ \sigma_{\theta\theta} = \sigma_{\phi\phi} &= \frac{aE}{(1-2\nu)} + \frac{bE}{(1+\nu)r^3} \end{aligned} \tag{E.7}$$

where E and ν are Young's modulus and Poisson's Ratio, respectively. The Bulk modulus, B, is

$$B = \frac{E}{3(1-2\nu)} \tag{E.8}$$

and Equation E.7 may be rewritten as

$$\begin{aligned} \sigma_{rr} &= 3aB - \frac{2bE}{(1+\nu)r^3} \\ \sigma_{\theta\theta} = \sigma_{\phi\phi} &= 3aB + \frac{bE}{(1+\nu)r^3} \end{aligned} \tag{E.9}$$

The stress equations may now be applied to a nanocrystal and the surrounding SiO_2 matrix and the constants a and b may be determined by applying the appropriate boundary conditions. The stresses in the nanocrystals and in the matrix are defined separately by Equation E.9. Therefore, there are six stress terms designated by σ_{ii}^{NC} and σ_{ii}^{Matrix}. As the radius of the nanocrystal approaches zero, the radial strain can not approach infinity, so b_{NC} must equal zero. As the radius of the silica matrix approaches infinity, the stress must go to zero. Therefore, a_{Matrix} must also equal zero and the system of equations defined by E.9 reduces to:

$$\begin{aligned} \sigma_{rr}^{NC} &= \sigma_{\theta\theta}^{NC} = \sigma_{\phi\phi}^{NC} = 3a_{NC}B_{NC} \\ \sigma_{rr}^{Matrix} &= -\frac{2b_{Matrix}E_{Matrix}}{(1+\nu_{Matrix})r^3} \\ \sigma_{\theta\theta}^{Matrix} &= \sigma_{\phi\phi}^{Matrix} = \frac{b_{Matrix}E_{Matrix}}{(1+\nu_{Matrix})r^3} \end{aligned} \qquad \text{(E.10)}$$

where μ_{Matrix} is the silica shear modulus and is defined as:

$$\mu^{Matrix} = \frac{E_{Matrix}}{(1+\nu_{Matrix})} \qquad \text{(E.11)}$$

The radii of the Ge nanocrystal and the matrix void can now be calculated as a function of their relaxed radii, R_o^{NC} and R_o^{Matrix}. It should be noted that the relaxed nanocrystal state defines the radius free of any stress, including that due to the Gibbs-Thomson effect. Since b_{NC} is zero, Equation E.6 gives the displacement within the nanocrystal as: $a_{NC}r$. Therefore, the strained Ge nanocrystal radius is:

$$R_{NC} = R_o^{NC}(1+a_{NC}) \qquad \text{(E.12)}$$

Similarly, the strained SiO_2 void radius is:

$$R_{Matrix} = R_o^{Matrix} + \frac{b_{Matrix}}{(R_o^{Matrix})^2} \tag{E.13}$$

It is assumed that the surface of the Ge nanocrystal is "welded" to the inner surface of the silica void so

$$R_{NC}(R_o^{NC}) = R_{Matrix}(R_o^{Matrix}) \tag{E.14}$$

At the silica-nanocrystal interface under equilibrium conditions, the difference between the stress at the silica void surface and the stress at the nanocrystal surface is equivalent to the stress arising from the Gibbs-Thomson effect. Using Equation 6.2, this boundary condition is written as:

$$\sigma_{rr}^{SiO_2}(R_{SiO_2}^{eq}) - \sigma_{rr}^{Ge}(R_{Ge}^{eq}) = \frac{2\gamma}{R_{Ge}^{eq}} \tag{E.15}$$

Where γ is the SiO_2/Ge interfacial energy. Application of the above boundary conditions (Equations E.14 & E.15) and Equations E.10-E.13 yields an expression for the initial void radius in terms of the initial total pressure, P_o^{NC}:

$$R_o^{Matrix} = \left(\frac{1 - \dfrac{P_o^{NC}}{3B_{NC}}}{1 + \dfrac{1}{4\mu^{Matrix}} \left[P_o^{NC} - \dfrac{2\gamma}{R_o^{NC}} \right]} \right) R_o^{NC} \tag{E.16}$$

The initial total pressure, P_o^{NC}, is comprised of both the pressure arising from the growth process, P_{agg}, and the size-dependent pressure from the Gibbs-Thomson effect:

$$P_o^{NC} = P_{agg} + \frac{2\gamma}{R_{Ge}} \tag{E.17}$$

Since Raman measurements are referenced to free-standing nanocrystals of the same size distribution as embedded crystals, it is the aggregation pressure which is measured experimentally.

Rearranging Equation E.16, and recognizing that the matrix cavity radius increases and relieves pressure during the post annealing process, the equation for the time-dependent total pressure, $P^{NC}(t)$ is:

$$P^{NC}(t) = \frac{12B_{NC}\mu^{Matrix}\left(R_o^{NC} - R_{Matrix}(t)\right) + 3B_{NC}R_{Matrix}(t)\dfrac{2\gamma}{R_o^{NC}}}{4\mu^{Matrix}R_o^{NC} + 3B_{NC}R_{Matrix}(t)} \qquad \text{(E.18)}$$

The experimental data relating the pressure to the post-growth annealing conditions may be modeled using a diffusive stress relaxation mechanism. Stress provides a driving force for the creation of matrix interstitials. These interstitials are assumed to have a volume, *Ω*, equal to the volume of a silica matrix molecule. When an interstitial diffuses away from the nanocrystal, the matrix void volume is necessarily increased by a volume *Ω*. This, in turn, reduces the stresses present on the nanocrystal and within the silica, thereby significantly reducing the total energy of the system.

Interstitials are well-defined in crystalline materials. However, for the case of the amorphous silica matrix, the definition of an interstitial is not so clear. Typically, interstitials within an amorphous material are defined as species that are not a part of the randomly oriented molecules that constitute the matrix. In the present case, interstitials are formed when a SiO_2 molecule dissociates into sub-species, such as Si, O, O_2, and Si-O. The energy required to dissociate a silica molecule is analogous to the formation energy of an interstitial in a crystalline material.

To model the stress relaxation process, the change in the Helmholtz free energy upon diffusion of an interstitial away from the nanocrystal is examined. In general, the change of the Helmholtz free energy may be written as:

$$dF = dU - TdS \tag{E.19}$$

Since the relaxation model involves the transport of matter, it is useful to express Equation E.19 in terms of the chemical potential and the pressure by substituting $dU = TdS - PdV + \mu dN$ to obtain:

$$dF = -PdV + \mu dN \tag{E.20}$$

Expansion of the void results in a decrease in the free energy of the nanocrystal from volume expansion by an amount *Ω*. The quantity of material within the crystal remains constant. The increase in surface area arising from the expansion leads to an additional positive interfacial energy term governed by the Ge/SiO_2 interfacial energy, *γ*. This may be expressed mathematically as:[143]

$$dF_{NC} = -P^{NC}\Omega + \frac{2\gamma}{R_{NC}}\Omega \tag{E.21}$$

The volume of the matrix, which is considered to be infinite, is not altered by the diffusion of the interstitial. However, interstitial formation requires the consumption of a SiO_2 molecule and the formation of a Si atom and two O atoms. It should be noted that other species, for example Si-O, may be created. In the present case, however, only dissociation to elemental components is considered. Therefore, the total free energy change of the silica according to Equation E.20 becomes:

$$dF_{matrix} = \left(\mu_{Si} + 2\mu_O - \mu_{SiO_2}\right)dn \tag{E.22}$$

where μ_i is the chemical potential of species i and dn is the change in the number of silica molecules. Using the thermodynamic relationship used to derive Equation E.20, the chemical potential may be expressed as:

$$\mu_j = \frac{dU_j}{dn} - T\frac{dS_j}{dn} \tag{E.23}$$

The entropy term may be evaluated by considering the change of configurational entropy when the number of interstitials changes from n to n+1. The entropy is written as a function of the number of interstitials, n, and the number of available interstitial sites, N:

$$S = k_B \ln\left(\frac{N!}{(N-n)!\,n!}\right) \tag{E.24}$$

For the case of large n and N and $N >> n$, Stirling's approximation may be applied and Equation E.24 reduces to:

$$S = k_B\{N\ln N - [n\ln n + (n-n)\ln(n-N)]\} \tag{E.25}$$

The concentration of interstitials is defined as: $c_i = n/N$. Taking the change in entropy $S(n+1) - S(n)$, and considering $N >> n$ gives:

$$\frac{dS}{dn} = -k_B \ln\left(\frac{n}{N-n}\right) = -k_B \ln c_i \tag{E.26}$$

The energy to create n elements of specie j is defined as:

$$E_j = \frac{dU_j}{dn} \tag{E.27}$$

Combining Equations E.22, E.23, E.26, & E.27 yields:

$$\begin{aligned} dF_2 &= \{(E_{Si} + k_B T\ln c_{Si}) + 2\mu_O - \mu_{SiO_2}\}dn \\ &= (E_F^i + k_B T \ln c_i)dn \end{aligned} \tag{E.28}$$

where E_F^i is defined as the formation energy for formation of an interstitial and is given by:

$$E_F^i = E_{Si} + 2\mu_O - \mu_{SiO_2} \tag{E.29}$$

The formation and diffusion of an interstitial away from the stressed nanocrystal is thermodynamically governed by a reduction of the free energy within the nanocrystal and an increase of the free energy associated with the formation of interstitial species. The total change in the Helmholtz free energy upon dissociation of a single SiO_2 molecule may be written as:

$$dF = dF_{NC} + dF_{matrix} = -P^{NC}\Omega + \frac{2\gamma}{R_{NC}}\Omega + E_F^i + k_B T \ln c_i \tag{E.30}$$

By applying the condition for local equilibrium, $dF = 0$, and solving Equation E.30, the concentration of interstitial species at the Ge/SiO_2 interface may be written as:

$$\begin{aligned} c_i &= \exp\left(-\frac{E_F^i}{k_B T} + \left[P^{NC} - \frac{2\gamma}{R_{NC}}\right]\frac{\Omega}{k_B T}\right) \\ &= c_i^{eq} \exp\left(\left[P^{NC} - \frac{2\gamma}{R_{NC}}\right]\frac{\Omega}{k_B T}\right) \end{aligned} \tag{E.31}$$

where

$$c_i^{eq} = \exp\left(-\frac{E_F^i}{k_B T}\right) \tag{E.32}$$

is the equilibrium concentration of interstitials and depends only on temperature. Equation E.31 shows that the pressure provides a driving force for the formation of interstitials above the equilibrium concentration. It is this effect which leads to the diffusive flux of interstitials away from the nanocrystal and reduces compressive stresses. It is assumed that the interstitials contributing to stress relaxation are Si atoms. The

diffusivity of O in SiO_2 is significantly larger than that of Si. Therefore, the diffusion of Si is the limiting process for nanocrystals to relax.

To determine the temperature-dependent rate of stress relief, the flux of interstitials away from the nanocrystal must be determined. It is assumed that the rate of nanocrystal growth is much smaller than the rate of interstitial diffusion. Therefore, a steady state diffusion condition is imposed as an approximation.[143] According to Fick's Second Law, steady state diffusion is defined by:

$$\nabla^2 c_i = \frac{1}{r^2}\frac{\partial}{\partial r}\left(r^2 \frac{\partial c_i}{\partial r}\right) = 0 \tag{E.33}$$

The concentration of interstitials at the Ge/SiO_2 interface is specified by Equation E.31 and gives one boundary condition. A second boundary condition is obtained by specifying the far-field equilibrium concentration of interstitial species as c_i^{eq}. Thus, the boundary conditions for solution of Equation E.33 are:

$$\begin{aligned} c_i(R^{Matrix}) &= c_i^{eq} \exp\left(\left[P^{NC} - \frac{2\gamma}{R_{NC}}\right]\frac{\Omega}{k_B T}\right) \\ c_i(\infty) &= c_i^{eq} \end{aligned} \tag{E.34}$$

Integration of Equation E.33 and application of the boundary conditions given by Equations E.34 yields:

$$c_i(r) = c_i^{eq} + \frac{R_{Matrix}}{r} c_i^{eq} \left\{ \exp\left(\left[P^{NC} - \frac{2\gamma}{R_{NC}}\right]\frac{\Omega}{k_B T}\right) - 1 \right\} \tag{E.35}$$

Since the radial interstitial concentration distribution is known, it is now possible to calculate the flux of interstitials at the interface as follows:

$$J_i = -\frac{D_i}{\Omega_i}\left(\frac{dc_i}{dr}\right)_{R_{Matrix}} = -\frac{D_i c_{eq}^i}{R_{Matrix}\Omega_i}\left\{1 - \exp\left(\left[P^{NC} - \frac{2\gamma}{R_{NC}}\right]\frac{\Omega}{k_B T}\right)\right\} \tag{E.36}$$

where Ω_i is the interstitial volume. The flux of interstitials is directly related to the time rate of change of the volume of the matrix cavity by:

$$\frac{dR_{Matrix}(t)}{dt} = \Omega J_i = \frac{\Omega D_i c_{eq}^i}{\Omega_i R_{Matrix}(t)} \left\{ \exp\left(\left[P^{NC}(t, R_{Matrix}) - \frac{2\gamma}{R_{NC}} \right] \frac{\Omega}{k_B T} \right) - 1 \right\} \qquad \text{(E.37)}$$

The product $\frac{\Omega}{\Omega_i} D_i c_{eq}^i$ can be treated as a standard transport coefficient with Arrhenius behavior governed by the activation energies for interstitial formation and migration in the following manner:

$$\frac{\Omega}{\Omega_i} D_i c_{eq}^i = D_o \exp\left(-\frac{E_M^i}{k_B T} \right) \exp\left(-\frac{E_F^i}{k_B T} \right) = D_o \exp\left(-\frac{E_A}{k_B T} \right) \qquad \text{(E.38)}$$

where E_A is the activation energy for interstitial diffusion. This term contains the energy of migration along with the energy for dissociation of a SiO_2 molecule to form interstitials. The final expression for the change of the matrix cavity radius with time as a function of the post-growth annealing temperature is:

$$\frac{dR_{Matrix}(t)}{dt} = \frac{D_o}{R_{Matrix}(t)} \exp\left(-\frac{E_A}{k_B T} \right) \left\{ \exp\left(\left[P^{NC}(t, R_{Matrix}) - \frac{2\gamma}{R_{NC}} \right] \frac{\Omega}{k_B T} \right) - 1 \right\} \qquad \text{(E.39)}$$

This equation is solved numerically, with Equation E.16 providing the initial radius at zero time and Equation E.18 providing an expression for the pressure as a function of the matrix void radius.

References

1. Kayanuma, Y. Quantum size effects of interacting electrons and holes in semiconductor microcrystals with spherical shape. *Phys. Rev. B* **38**, 9797 (1988).

2. Weisbuch, C. & Vinter, B. *Quantum Semiconductor Structures, Fundamentals, and Applications* (Academic, San Diego, CA, 1991).

3. Ciraci, S., Buldum, A. & Batra, I. P. Quantum effects in electrical and thermal transport through nanowires. *J. Phys.: Condens. Matter.* **13**, R537 (2001).

4. Xia, Y. *et al.* One-dimensional nanostructures: synthesis, characterization and applications. *Adv. Mater.* **15**, 353 (2003).

5. Huang, Y., Duan, X., Wei, Q. & Lieber, C. M. Directed assembly of one-dimensional nanostructures into functional networks. *Science* **291**, 630 (2001).

6. Goldberger, J. *et al.* Single-crystal gallium nitride nanotubes. *Nature* **422**, 599 (2003).

7. Javey, A., Guo, J., Wang, Q., Lundstrom, M. & Dai, H. Ballistic carbon nanotube field-effect transistors. *Nature* **424**, 654 (2003).

8. Duan, X. *et al.* High-performance thin-film transistors using semiconductor nanowires and nanoribbons. *Nature* **425**, 274 (2003).

9. Melosh, N. A. *et al.* Ultrahigh-density nanowire lattices and circuits. *Science* **300**, 112 (2003).

10. Ma, D. D. D., Lee, C. S., Au, F. C. K., Tong, S. Y. & Lee, S. T. Small-diameter silicon nanowire surfaces. *Science* **299**, 1874 (2003).

11. Bachilo, S. M. *et al.* Structure-assigned optical spectra of single-walled carbon nanotubes. *Science* **298**, 2361 (2002).

12. Misewich, J. A. *et al.* Electrically induced optical emission from a carbon nanotube FET. *Science* **300**, 783 (2003).

13. Landin, L., Miller, M. S., Pistol, M.-E., Pryor, C. E. & Samuelson, L. Optical studies of individual quantum dots in GaAs: Few-particle effects. *Science* **280**, 262 (1998).

14. Hu, J. *et al.* Linearly polarized emission from colloidal semiconductor quantum rods. *Science* **292**, 2060 (2001).

15. Coe, S., Woo, W.-K., Bawendi, M. & Bulovic, V. Electroluminescence from single monolayers of nanocrystals in molecular organic devices. *Nature* **420**, 800 (2002).

16. Klimov, V. I. *et al.* Optical gain and stimulated emission in nanocrystal quantum dots. *Science* **290**, 314 (2000).

17. Thompson, R. M. *et al.* Single-photon emission from exciton complexes in individual quantum dots. *Phys. Rev. B* **64**, 201302 (2001).

18. Moreau, E. *et al.* Quantum cascade of photons in semiconductor quantum dots. *Phys. Rev. Lett.* **87**, 183601 (2001).

19. Kanemitsu, Y. *et al.* Visible light emission from GaAs nanocrystals in SiO_2 films fabricated by sequential ion implantation. *Phys. Rev. B* **62**, 5100 (2000).

20. Ouyang, M. & Awschalom, D. D. Coherent spin transfer between molecularly bridged quantum dots. *Science* **301**, 1074 (2003).

21. Recher, P., Sukhorukov, E. V. & Loss, D. Quantum dot as spin filter and spin memory. *Phys. Rev. Lett.* **85**, 1962 (2000).

22. Gupta, J. A., D.D. Awschalom, Efros, A. L. & Rodina, A. V. Spin dynamics in semiconductor nanocrystals. *Phys. Rev. B* **66**, 125307 (2002).

23. Tiwari, S. *et al.* A silicon nanocrystals based memory. *Appl. Phys. Lett.* **68**, 1377 (1995).

24. Kouvatsos, D. N., Ionannou-Sougleridis, V. & Nassiopoulou, A. G. Charging effects in silicon nanocrystals within SiO_2 layers, fabricated by chemical vapor deposition, oxidation, and annealing. *Appl. Phys. Lett.* **82**, 397 (2003).

25. Pettersson, H., Bååth, L., Carlsson, N., Seifert, W. & Samuelson, L. Optically induced carge storage and current generation in InAs quantum dots. *Phys. Rev. B* **65**, 073304 (2002).

26. Priester, C. & Lannoo, M. Origin of Self-Assembled Quantum Dots in Highly Mismatched Heteroepitaxy. *Phys. Rev. Lett.* **75**, 93 (1995).

27. Medeiros-Ribeiro, G., Bratkovski, A. M., Kamins, T. I., Ohlberg, D. A. A. & Williams, R. S. Shape transition of germanium nanocrystals on a silicon (001) surface from pyramids to domes. *Science* **279**, 353 (1998).

28. Krzyzewski, T. J., Joyce, P. B., Bell, G. R. & Jones, T. S. Role of two- and three-dimensional surface structures in InAs-GaAs(001) quantum dot nucleation. *Phys. Rev. B* **66**, 121307 (2002).

29. Heun, S. *et al.* Core-level photoelectron spectroscopy from individual heteroepitaxial nanocrystals on GaAs(001). *Phys. Rev. B* **63**, 125335 (2001).

30. Chambers, S. A. *et al.* Epitaxial growth and properties of MBE-grown ferromagnetic Co-doped TiO_2 anatase films on $SrTiO_3$ (001) and $LaAlO_3$ (001). *Thin Solid Films* **418**, 197 (2002).

31. Manna, L., Milliron, D. J., Meisel, A., Scher, E. C. & Alivisatos, A. P. Controlled growth of tetrapod-branched inorganic nanocrystals. *Nature Materials* **2**, 382 (2003).

32. Chan, E. M., Mathies, R. A. & Alivisatos, A. P. Size-controlled growth of CdSe nanocrystals in microfluidic reactors. *Nano Lett.* **3**, 199 (2003).

33. Murray, C. B., Kagan, C. R. & Bawendi, M. G. Synthesis and characterization of monodisperse nanocrystals and close-packed nanocrystal assemblies. *Annu. Rev. Mater. Sci.* **30**, 545 (2000).

34. Wilcoxon, J. P., Provencio, P. P. & Samara, G. A. Synthesis and optical properties of colloidal germanium nanocrystals. *Phys. Rev. B* **64**, 035417 (2001).

35. Stowell, C. A., Wiacek, R. J., Saunders, A. E. & Korgel, B. A. Synthesis and characterization of dilute magnetic semiconductor manganese-doped indium arsenide nanocrystals. *Nano Lett.* **3**, 1441 (2003).

36. Hayashi, S., Tanimoto, S., Fujii, M. & Yamamoto, K. Surface oxide layers of Si and Ge nanocrystals. *Superlattices & Microstructures* **8**, 13 (1990).

37. Thielsch, R. *et al.* Quantum-size effects of PbS nanocrystallites in evaporated composite films. *Nanostructured Materials* **10**, 131 (1998).

38. Kanjilal, A. *et al.* Structural and electrical properties of silicon dioxide layers with embedded germanium nanocrystals grown by molecular beam epitaxy. *Appl. Phys. Lett.* **82**, 1212 (2003).

39. Maeda, Y., Tsukamoto, N., Yazawa, Y., Kanemitsu, Y. & Matsumoto, Y. Visible photoluminescence of Ge microcrystals embedded in SiO_2 glassy matrices. *Appl. Phys. Lett.* **59**, 3168 (1991).

40. Zhu, J. G., White, C. W., Budai, J. D., Withrow, S. P. & Chen, Y. Growth of Ge, Si, and SiGe nanocrystals in SiO_2 matrices. *J. Appl. Phys.* **78**, 4386 (1995).

41. Kolobov, A. V. *et al.* Formation of Ge nanocrystals embedded in a SiO_2 matrix: Transmission electron microscopy, x-ray absorption, and optical studies. *Phys. Rev. B* **67**, 195314 (2003).

42. Budai, J. D. *et al.* Controlling the size, structure, and orientation of semiconductor nanocrystals using metastable phase recrystallization. *Nature* **390**, 384 (1997).

43. Grom, G. F. *et al.* Ordering and self-organization in nanocrystalline silicon. *Nature* **407**, 358 (2000).

44. White, C. W., Budai, J. D., Zhu, J. G., Withrow, S. P. & Aziz, M. J. Ion-beam synthesis and stability of GaAs nanocrystals in silicon. *Appl. Phys. Lett.* **68**, 2389 (1996).

45. Shiryaev, S. Y., Larsen, A. N. & Deicher, M. The chemical interaction between high-concentration, mixed-ion-implanted group-III and -V impurities in silicon. *J. Appl. Phys.* **72**, 410 (1992).

46. Guha, S., Qadri, S. B., Musket, R. G., Wall, M. A. & Shimizu-Iwayama, T. Characterization of Si nanocrystals grown by annealing SiO_2 films with uniform concentrations of implanted Si. *J. Appl. Phys.* **88**, 3954 (2000).

47. Yamamoto, M., Koshikawa, T., Yasue, T., Harima, H. & Kajiyama, K. Formation of size controlled Ge nanocrystals in SiO_2 matrix by ion implantation and annealing. *Thin Solid Films* **369**, 100 (2000).

48. Normand, P. *et al.* Effect of annealing environment on the memory properties of thin oxides with embedded Si nanocrystals obtained by low-energy ion-beam synthesis. *Appl. Phys. Lett.* **83**, 168 (2003).

49. Zhang, H., Gilbert, B., Huang, F. & Banfield, J. F. Water-driven structure transformation in nanoparticles at room temperature. *Nature* **424**, 1025 (2003).

50. Dai, Y., Han, S., Dai, D., Zhang, Y. & Qi, Y. Surface passivant effects on electronic states of the band edge in Si-nanocrystals. *Solid State Commun.* **126**, 103 (2003).

51. Vasiliev, I., Chelikowsky, J. R. & Martin, R. M. Surface oxidation effects on the optical properties of silicon nanocrystals. *Phys. Rev. B* **65**, 121302 (2002).

52. Patel, A. A. *et al.* Synthesis, optical spectroscopy and ultrafast electron dynamics of PbS nanoparticles with different surface capping. *J. Chem. Phys.* (2000).

53. Takagahara, T. & Takeda, K. Theory of quantum confinement effect on excitons in quantum dots of indirect-gap materials. *Phys. Rev. B* **46**, 15578 (1992).

54. Gu, G. *et al.* Growth and electrical transport of germanium nanowires. *J. Appl. Phys.* **90**, 5747 (2001).

55. Böer, K. W. *Survey of SemiconductorPhysics* (Van Nostrand Reinhold, NY, 1990).

56. Maeda, Y. Visible photoluminescence from nanocrystallite Ge embedded in a glassy SiO_2 matrix: Evidence in support of the quantum-confinement mechanism. *Phys. Rev. B* **51**, 1658 (1995).

57. Craciun, V., Boulmer-Leborgne, C., Nicholls, E. J. & Boyd, I. W. Light emission from germanium nanocrystals formed by ultraviolet assisted oxidation of silicon-germanium. *Appl. Phys. Lett.* **69**, 1506 (1996).

58. Kim, B. *et al.* The origin of photoluminescence in Ge-implanted SiO_2 layers. *J. Luminescence* **80**, 281 (1999).

59. Taraschi, G., Saini, S., Fan, W. W., Kimerling, L. C. & Fitzgerald, E. A. Nanostructure and infrared photoluminescence of nanocrystalline Ge formed by reduction of $Si_{0.75}Ge_{0.25}O_2/Si_{0.75}Ge_{0.25}$ using various H_2 pressures. *J. Appl. Phys.* **93**, 9988 (2003).

60. Shcheglov, K. V., Yang, C. M., Vahala, K. J. & Atwater, H. A. Electroluminescence and photoluminescence of Ge-implanted Si/SiO_2/Si structures. *Appl. Phys. Lett.* **66**, 745 (1994).

61. Ye, Y. H., Zhang, J. Y., Bao, X. M., Tan, X. L. & Chen, L. F. Visible photoluminescence from Ge^+-implanted SiO_2 films thermally grown on crystalline Si. *Appl. Phys. Lett.* **67**, 213 (1998).

62. Wu, X. L., Gao, T., Siu, G. G., Tong, S. & Bao, X. M. Defect-related infrared photoluminescence in Ge^+-implanted SiO_2 films. *Appl. Phys. Lett.* **74**, 2420 (1999).

63. Zhang, J.-Y., Ye, Y.-H., Tan, X.-L. & Bao, X.-M. Effect of density of Ge nanocrystals on violet-blue photoluminescence of Ge^+-implanted SiO_2 film. *J. Appl. Phys.* **86**, 6139 (1999).

64. Rebohle, L., Borany, J. v., Fröb, H. & Skorupa, W. Blue photo- and electroluminescence of silicon dioxide layers ion-implanted with group IV elements. *Appl. Phys. B* **71**, 131 (2000).

65. Fukuda, H. *et al.* Physical and electrical properties of Ge-implanted SiO_2 films. *J. Appl. Phys.* **90**, 3524 (2001).

66. Rebohle, L. *et al.* Transient behavior of the strong violet electroluminescence of Ge-implanted SiO_2 layers. *Appl. Phys. B* **74**, 53 (2002).

67. Shklyaev, A. A. & Ichikawa, M. Visible photoluminescence of Ge dots embedded in Si/SiO_2 matrices. *Appl. Phys. Lett.* **80**, 1432 (2002).

68. Tiwari, S., Rana, F., Chan, K., Shi, L. & Hanafi, H. Single chanrge and confinement effects in nano-crystal memories. *Appl. Phys. Lett.* **69**, 1232 (1996).

69. Shchukin, V. A., Ledentsov, N. N., Kop'ev, P. S. & Bimberg, D. Spontaneous Ordering of Arrays of Coherent Strained Islands. *Phys. Rev. Lett.* **75**, 2968 (1995).

70. Tersoff, J., Teichert, C. & Lagally, M. G. Self-Organization in Growth of Quantum Dot Superlattices. *Phys. Rev. Lett.* **76**, 1675 (1996).

71. Shchukin, V. A., Bimberg, D., Munt, T. P. & Jesson, D. E. Metastability of Ultradense Arrays of Quantum Dots. *Phys. Rev. Lett.* **90**, 076102 (2003).

72. Gai, Z. *et al.* Self-Assembly of Nanometer-Scale Magnetic Dots with Narrow Size Distributions on an Insulating Substrate. *Phys. Rev. Lett.* **89**, 235502 (2002).

73. Liu, F., Li, A. H. & Lagally, M. G. Self-Assembly of Two-Dimensional Islands via Strain-Mediated Coarsening. *Phys. Rev. Lett.* **87**, 126103 (2001).

74. Meixner, M., Schöll, E., Shchukin, V. A. & Bimberg, D. Self-Assembled Quantum Dots: Crossover from Kinetically Controlled to Thermodynamically Limited Growth. *Phys. Rev. Lett.* **87**, 236101 (2001).

75. Rajh, T., Micic, O. I. & Nozik, A. J. Synthesis and characterization of surface-modified colloidal CdTe quantum dots. *J. Phys. Chem. B* **97**, 11999 (1993).

76. Counio, G., Gacoin, T. & Boilot, J. P. Synthesis and photoluminescence of $Cd_{1-x}Mn_xS$ nanocrystals. *J. Phys. Chem. B* **102**, 5257 (1998).

77. Heath, J. R., Shiang, J. J. & Alivisatos, A. P. Germanium quantum dots: Optical properties and synthesis. *J. Chem. Phys.* **101**, 1607 (1994).

78. Skorupa, W., Rebohle, L. & Gebel, T. Group-IV nanocluster formation by ion-beam synthesis. *Appl. Phys. A* **76**, 1049 (2003).

79. Milovzorov, D. & Suzuki, T. Size-dependent second-harmonic generation by nanocrystals prepared by plasma-enhanced chemical-vapor deposition. *Appl. Phys. Lett.* **75**, 4103 (1999).

80. Marzen, F., Baron, T., Papon, A. M., Truche, R. & Hartmann, J. M. A two steps CVD process for the growth of silicon nanocrystals. *Appl. Surf. Sci.* **214**, 359 (2003).

81. Choi, W. K. *et al.* Raman characterization of germanium nanocrystals in amorphous silicon oxide films synthesized by rapid thermal annealing. *J. Appl. Phys.* **86**, 1398 (1999).

82. Shen, J. K., Wu, X. L., Tan, C., Yuan, R. K. & Bao, X. M. Correlation of electroluminescence with Ge nanocrystal sizes in Ge-SiO_2 co-sputtered films. *Phys. Lett. A* **300**, 307 (2002).

83. Dubiel, M., Hofmeister, H., Schurig, E., Wendler, E. & Wesch, W. On the stress state of silver nanoparticles in ion-implanted silicate glasses. *Nucl. Instrum. Methods B* **166-167**, 871 (2000).

84. Ignatova, V. A. *et al.* Metal and composite nanocluster precipitate formation in silicon dioxide implanted with Sb^+ ions. *J. Appl. Phys.* **92**, 4336 (2002).

85. Anderson, T. S., III, R. H. M., Wittig, J. E., Kinser, D. L. & Zuhr, R. A. Fabrication of Cu-coated Ag nanocrystals in silica by sequential ion implantation. *Nucl. Instrum. Methods B* **171**, 401 (2000).

86. Liu, Z. *et al.* Favored structure of Ag nanoparticles embedded in SiO_2, by implantation: Single crystal with contracted (111) lattice. *J. Mat. Res.* **15**, 1245 (2000).

87. Ando, M. *et al.* Sharp photoluminescence of CdS nanocrystals in Al_2O_3 matrices formed by sequential ion implantation. *Appl. Phys. Lett.* **79**, 539 (2001).

88. Borany, J. v. *et al.* Ion beam synthesis of narrow Ge nanocluster bands in thin SiO_2 films. *Microelectron. Engin.* **48**, 231 (1999).

89. Karl, H., Hipp, W., Grosshans, I. & Stritzker, B. Ion beam synthesis of buried CdSe nanocrystallites in SiO2 on (100)-silicon. *Mat. Sci. Eng. C* **19**, 55 (2002).

90. Strobel, M., Heinig, K. H. & Moller, W. Can core/shell nanocrystals be fomed by sequential ion implantation? Predictions from kinetic Monte Carlo simulations. *Nucl. Instrum. Methods B* **148**, 104 (1999).

91. Muller, T., Heinig, K. H. & Schmidt, B. Formation of Ge nanowires in oxidized silicon V-grooves by ion beam synthesis. *Nucl. Instrum. Methods B* **175**, 468 (2001).

92. Muller, T., Heinig, K. H. & Schmidt, B. Template-directed self-assembly of buried nanowires and the pearling instability. *Mat. Sci. Eng. C* **19**, 209 (2002).

93. Lide, D. R. (ed.) *CRC Handbook of Chemistry and Physics* (CRC Press, New York, 2002).

94. Ziegler, J. F., Biersack, J. P. & Littmark, W. *The Stopping Range of Ions in Matter* (Pergamon Press, New York, 1985).

95. Leavitt, J. A., L.C. McIntyre, J. & Weller, M. R. in *Handbook of Modern Ion Beam Materials Analysis* (eds. Tesmer, J. R. & Nastasi, M.) (Materials Research Society, Pittsburgh, Pennsylvania, 1995).

96. Nilsson, G. & Nelin, G. Phonon dispersion relations in Ge at 80 K. *Phys. Rev. B* **3**, 364 (1971).

97. Yu, P. Y. & Cardona, M. *Fundamentals of Semiconductors: Physics and Materials Properties* (Springer, Berlin, 2001).

98. Kittel, C. *Introduction to Solid State Physics* (John Wiley & Sons, New York, 1996).

99. Richter, H., Wang, Z. P. & Ley, B. The one phonon Raman spectrum in microcrystalline silicon. *Solid State Commun.* **39**, 625 (1981).

100. Fujii, M., Hayashi, S. & Yamamoto, K. Growth of Ge microcrystals in SiO_2 thin film matrices: A Raman and electron microscopic study. *Jpn. J. Appl. Phys.* **30**, 687 (1991).

101. Campbell, I. H. & Fauchet, P. M. The effects of microcrystal size and shape on the one phonon Raman spectra of crystalline semiconductors. *Solid State Commun.* **58**, 739 (1986).

102. Cerdeira, F., Buchenauer, C. J., Pollak, F. H. & Cardona, M. Stress-Induced Shifts of First-Order Raman Frequencies of Diamond- and Zinc-Blende-Type Semiconductors. *Phys. Rev. B* **5**, 580 (1972).

103. Heinig, K. H. *et al.* Microstructural investigation of ion beam synthesised germanium nanoclusters embedded in SiO_2 layers. *Nucl. Instrum. Methods B* **142**, 969 (1999).

104. Bording, J. K. & Tafto, J. Molecular-dynamics simulation of growth of nanocrystals in an amorphous matrix. *Phys. Rev. B* **62**, 8098 (2000).

105. Sharp, I. D. *et al.* Liberation of ion implanted Ge nanocrystals from a silicon dioxide matrix via hydrofluoric acid vapor etching. *Mat. Res. Soc. Symp. Proc.* **777**, T7.6.1 (2003).

106. Rolo, A. G., Vasilevskiy, M. I., Conde, O. & Gomes, M. J. M. Structural properties of Ge nano-crystals embedded in SiO_2 films from X-ray diffraction and Raman spectroscopy. *Thin Solid Films* **336**, 58 (1998).

107. Lanninn, J. S., Maley, N. & Kshirsager, S. T. Raman scattering and short range order in amorphous germanium. *Solid State Commun.* **53**, 939 (1985).

108. Cheng, W., Ren, S.-F. & Yu, P. Y. Theoretical investigation of the surface vibrational modes in germanium nanocrystals. *Phys. Rev. B* **68**, 193309 (2003).

109. Deegan, T. & Hughes, G. An X-ray photoelectron spectroscopy study of the HF etching of native oxides on Ge(111) and Ge(100) surfaces. *Appl. Surf. Sci.* **123-124**, 66 (1998).

110. Liu, H. I., Biegelsen, D. K., Ponce, F. A., Johnson, N. M. & Pease, R. F. W. Self-limiting oxidation for fabricating sub-5 nm silicon nanowires. *Appl. Phys. Lett.* **64**, 1383 (1994).

111. Borodin, V. A., Heinig, K. H., Schmidt, B. & Oswald, S. Oxidation of Ge implanted into SiO_2 layers: Modeling and XPS. *Nucl. Instrum. Methods B* **178**, 115 (2001).

112. Israelachvili, J. N. *Intermolecular and Surface Forces* (Academic Press, London, 1985).

113. Hamaker, H. C. The London-van der Waals attraction between spherical particles. *Physica* **4**, 1058 (1937).

114. Decossas, S., Mazen, F., Baron, T., Bremond, G. & Souifi, A. Atomic force microscopy nanomanipulation of silicon nanocrystals for nanodevice fabrication. *Nanotechnology* **14**, 1272 (2003).

115. Buffat, P. & Borel, J.-P. Size effect on the melting temperature of gold particles. *Phys. Rev. A* **13**, 2287 (1976).

116. Goldstein, A. N., Echer, C. M. & Alivisatos, A. P. Melting in semiconductor nanocrystals. *Science* **256**, 1425 (1992).

117. Peters, K. F., Cohen, J. B. & Chung, Y.-W. Melting of Pb nanocrystals. *Phys. Rev. B* **57**, 13430 (1998).

118. Zhang, M. *et al.* Size-dependent melting point depression of nanostructures: Nanocalorimic measurements. *Phys. Rev. B* **62**, 10548 (2000).

119. Wu, Y. & Yang, P. Melting and welding semiconductor nanowires in nanotubes. *Adv. Mater.* **13**, 520 (2001).

120. Radloff, C. & Halas, N. J. Enhanced thermal stability of silica-encapsulated metal nanoshells. *Appl. Phys. Lett.* **79**, 674 (2001).

121. Zhong, J., Zhang, L. H., Jin, Z. H., Sui, M. L. & Lu, K. Superheating of Ag nanoparticles embedded in Ni matrix. *Acta. mater.* **49**, 2897 (2001).

122. Liang, L. H., Li, J. C. & Jiang, Q. Superheating thermodynamics of nanocrystals based on the interface effect. *Physica B* **322**, 188 (2002).

123. Menendez, J. & Cardona, M. Temperature dependence of the first-order Raman scattering by phonons in Si, Ge, and alpha-Sn: Anharmonic effects. *Phys. Rev. B* **29**, 2051 (1984).

124. Balkanski, M., Wallis, R. F. & Haro, E. Anharmonic effects in light scattering due to optical phonons in silicon. *Phys. Rev. B* **28**, 1928 (1983).

125. Hart, T. R., Aggarwal, R. L. & Lax, B. Temperature dependence of Raman scattering in silicon. *Phys. Rev. B* **1**, 638 (1970).

126. Haro, E., Balkanski, M., Wallis, R. F. & Wanser, K. H. Theory of damping and shift of the Raman mode in silicon. *Phys. Rev. B* **34**, 5358 (1986).

127. Klemens, P. G. Anharmonic decay of optical phonons. *Phys. Rev.* **148**, 845 (1966).

128. Tang, H. & Herman, I. P. Raman microprobe scattering of solid silicon and germanium at the melting temperature. *Phys. Rev. B* **43**, 2299 (1991).

129. Burke, H. H. & Herman, I. P. Temperature dependence of Raman scattering in $Ge_{1-x}Si_x$ alloys. *Phys. Rev. B* **48**, 15016 (1993).

130. Mishra, P. & Jain, K. P. Temperature-dependent Raman scattering studies in nanocrystalline silicon and finite-size effects. *Phys. Rev. B* **62**, 14790 (2000).

131. Anderson, H. H. & Johnson, E. tructure, morphology and melting hysteresis of ion-implanted nanocrystals. *Nucl. Instrum. Methods B* **106**, 480 (1995).

132. Wellner, A., Paillard, V., Bonafos, C., Coffin, H. & Claverie, A. Stress measurements of germanium nanocrystals embedded in silicon dioxide. *J. Appl. Phys.* **94**, 5639 (2003).

133. Wautelet, M. Estimation of the variation of the melting temperature with the size of small particles, on the basis of a surface-phonon instability model. *J. Phys. D: Appl. Phys.* **24**, 343 (1991).

134. Zhang, Z., Zhao, M. & Jiang, Q. Melting temperatures of semiconductor nanocrystals in the mesoscopic size range. *Semicond. Sci. Technol.* **16**, L33 (2001).

135. Shrivastava, K. N. Melting temperature, Brillouin shift, and density of states of nanocrystals. *Nano Lett.* **2**, 519 (2002).

136. Tu, K., Mayer, J. W. & Feldman, L. C. *Electronic Thin Film Science* (Macmillan Publishing Co., New York, 1992).

137. Meyerson, B. S. High speed silicon-germanium electronics. *Sci. Am.* **270**, 42 (1994).

138. Cheung, A. *et al.* Structural perturbations within Ge nanocrystals in silica. *Appl. Phys. Lett.* **84**, 278 (2004).

139. Serincan, U. *et al.* Characterization of Ge nanocrystals embedded in SiO_2 by Raman spectroscopy. *Semicond. Sci. Technol.* **19**, 247 (2004).

140. Wu, X. L. *et al.* Annealing temperature dependence of Raman scattering in Ge^+-implanted SiO_2 films. *J. Appl. Phys.* **82**, 2704 (1997).

141. Yi, D. O. & Chrzan, D. C. personal communication.

142. Porter, D. A. & Easterling, K. E. *Phase Transformations in Metals and Alloys* (Stanley Thornes Publishers Ltd, Bath, UK, 1992).

143. Greenwood, G. W., Foreman, A. J. E. & Rimmer, D. E. The role of vacancies and dislocations in the nucleation and growth of gas bubbles in irradiated fissible material. *J. Nucl. Mater.* **4**, 305 (1959).

144. Tsoukalas, D., Tsamis, C. & Normand, P. Diffusivity measurements of silicon in silicon dioxide layers using isotopically pure material. *J. Appl. Phys.* **89**, 7809 (2001).

145. Takahashi, T. *et al.* Self-diffusion of Si in thermally grown SiO_2 under equilibrium conditions. *J. Appl. Phys.* **93**, 3674 (2003).

146. Postmus, C., Ferraro, J. R. & Mitra, S. S. Pressure dependence of infrared eigenfrequencies of KCl and KBr. *Phys. Rev.* **174**, 983 (1968).

147. Godfrey, D. E. N. *Theoretical Elasticity and Plasticity for Engineers* (Thames and Hudson, London, 1959).

148. Landau, L. D. & Lifshitz, E. M. *Theory of Elasticity* (Pergamon Press, Oxford, 1975).